Design and Analysis of Whispering Gallery Mode Semiconductor Lasers

Ali T. Hajjiah

Dissertation submitted to the faculty of the Virginia Polytechnic Institute and State University in partial fulfillment of the requirements for the degree of

Doctor of Philosophy

In

Electrical Engineering

Professor Louis J. Guido Chair

Professor Robert Hendricks

Professor Guo Quan Lu

Professor Ahmad Safaai-Jazi

Professor Levon V. Asryan

January 19th, 2009

Blacksburg, Virginia

Keywords: Semiconductor laser, Whispering Gallery-Mode

Copyright 2009, Ali Hajjiah

Design and Analysis of Whispering Gallery Mode Semiconductor Lasers

Ali T. Hajjiah

Abstract

Significant technical barriers currently prevent the wide spread adoption of WGM lasers as building blocks in large-scale photonic integrated circuits. The first challenge is to reduce the electrical power consumption at desirable levels of light output power. The second target is to obtain directional light emission without sacrificing other laser performance metrics. The best opportunity for success lies in the pursuit of small *μ-Pillar lasers* with spiral-geometry cavities. Process technology has been demonstrated for making high-performance WGM lasers including a refined ICP etching process for fabricating *μ-Pillar* cavities with sidewall roughness less than 10 nm and a new hydrogenation based approach to achieving current blocking that is compatible with all other processing steps and robust in comparison with earlier reports. A comprehensive photo-mask has been designed that enables investigation of the interplay between device geometry and WGM laser performance. Emphasis has been placed on enabling experiments to determining the impact of diffraction and scattering losses, current and carrier confinement, and surface recombination on electrical/optical device characteristics. In addition, a methodology has been developed for separating out process optimization work from the task of identifying the best means for directional light out-coupling. Our device fabrication methods can be proven on WGM lasers with pure cylindrical symmetry, hence results from these experiments should be independent of any specific light output coupling scheme. Particular attention has been paid to the fact that device geometries that give the best performance for purely symmetrical cavities may not yield the highest level of light emission from the spiral output notch. Such considerations seem to be missing from much of the earlier work reported in the literature. Finally, our processing techniques and device designs have resulted in individual WGM lasers that outperform those made by competitors. These devices have been incorporated into multi-element, coupled-cavity optical circuits thereby laying the groundwork for construction of digital photonic gates that execute AND, OR, and NOT logic functions.

Acknowledgments

I would like to express my gratitude to the following people:

- My thesis advisor, Prof. L. Guido, whose mentorship and support made my graduate career a truly remarkable experience. Despite his busy schedule, he has always made time for discussion. In addition to the scientific side, he has also provided me with invaluable help in carefully planning and managing the different steps of my research. I have truly learned a lot during my thesis, which goes beyond science itself.

- The members of my thesis committee: Prof. G.Q.Lu, Prof. Ahmad Safaai-Jazi, Prof. Robert Hendricks, and Prof. Levon Asryan for their guidance and support throughout my Ph.D. study.

- The other members of Prof. Guido's group, Kevin and Tim for all the support they have given me during my stay here in Virginia Tech.

- All my friends in Blacksburg for their friendship over the past 7 years. They have helped me many times through good and bad times.

- I would like to thank Kuwait University for all the financial support and help they provided me. Without them, it would not have been possible to finish this very difficult journey.

- I would like to give a special thanks to my lovely wife, Alya, who has always supported me during my difficult journey. Her love, understanding and support have made my journey easy.

- Last but not least, I wish to thank my parents, my mother Sara and my father Talib, for their support, love and patience during my entire time at Virginia Tech. In particular my father Talib, who I deeply admire, has provided me with advice and helped me overcome many challenging situations. He has always been an inspiration and motivation source to me. It is to my wife and parents; I wish to dedicate this thesis.

Table of Contents

Abstract ii

Acknowledgments iii

Table of Contents iv

List of Figures vii

List of Tables xiii

1. Introduction 1

1.1. Historical Perspective 1

1.2. Problem Statement 5

1.3. Technical Objectives 6

1.4. Chapter Overview 7

References 9

2. Technical Background 13

2.1. Design Considerations for Diode Lasers 15

2.1.1. Compound Semiconductor Alloys 15

2.1.2. Carrier Injection via P-N Heterojunctions 16

2.1.3. Separate Confinement Heterostructures 18

2.1.4. Low Dimensional Gain Media 20

2.2. Optical Modes in Dielectric Structures 22

2.2.1. Transverse Modes in Slab Waveguides 22

2.2.2. Lateral Modes in Ridge Waveguides 25

2.2.3. WGMs in Cylindrical Cavities 26

Reference..31
3. Material Structure and Device Processing..36
3.1. Description of Material Structures..36
3.2. Overview of Device Processing..38
3.3. Design of μ-Pillar Optical Cavities..40
3.4. Layout of μ-Pillar Photomask..43
References..45
4. Measurement Techniques and Device Analysis..46
4.1. Instrument Design and Calibration..46
4.1.1. Apparatus for I-V Measurements..46
4.1.2. Apparatus for L-I Measurements..49
4.1.3. Apparatus for Spectral Measurements..55
4.2. Performance Metrics for Diode Lasers..57
4.3. Parameter Extraction for Diode Lasers..60
4.3.1. Analysis of I-V Characteristics..60
4.3.2. Analysis of L-I Characteristics..64
4.3.3. Analysis of Emission Spectra..65
References..68
5. Process Development for WGM Lasers..69
5.1. Formation of μ-Pillar Optical Cavities..69
5.1.1. Evaluation of Fabrication Methods..69
5.1.2. Optimization of Dry Etching Process..73

5.2. Preparation of Metal/Semiconductor Contacts 81

5.3. Current Blocking via Hydrogen Passivation 86

References 94

6. Design Considerations for WGM Lasers 98

6.1. Optical Losses via Diffraction 102

6.2. Optical Losses via Scattering 103

6.3. Electrical Losses via Current Leakage...105

6.4. Electrical Losses via Carrier Recombination.....................................107

6.5. Output Coupling from WGM Lasers 110

6.5.1. Output Coupling via Y-Junctions 110

6.5.2. Output Coupling via Evanescent Waves..111

6.5.3. Output Coupling via Spiral Cavities 112

References 114

7. Summary and Conclusions 122

Appendix A: Analysis of Optical Modes in Slab Waveguides.............................124

Appendix B: Analysis of Optical Modes in Cylindrical Cavities 134

Appendix C: Procedures for WGM Laser Fabrication 142

Appendix D: Definition of Optical Confinement Factor 164

Appendix E: Design Parameters for WGM Lasers..171

List of Figures

Figure 1.1: Schematics for the three basic radiative transitions envisioned by Einstein in 1929. 2

Figure 1.2: Plan view image of St. Paul's Cathedral in London. The solid white line traces out the circular propagation path of an acoustic wave confined at the periphery of the dome (http://www.explore-stpauls.net/oct03/textMM/DomeConstructionN.htm). 4

Figure 2.1: Schematic of a broad-area, edge-emitting Fabry-Perot laser. 14

Figure 2.2: Bandgap energy vs. lattice constant for some III-V semiconductors. The plotted data correspond to room temperature values of these physical quantities (Materials catalogue, EPI Materials Ltd., Lancaster Way, Ely, Cambridge-shire, (CB6 3NW UK)). 15

Figure 2.3: Energy vs. distance diagram for a separate-confinement p-n junction heterostructure laser under high forward bias. This state of operation is referred to as "flat-band" since the built-in diode potential is offset by the applied voltage giving rise to a spatially independent energy band structure..................................17

Figure 2.4: Energy vs. position diagram (upper panel) and corresponding refractive index profile (lower panel) for a separate-confinement heterostructure laser. The optical intensity pattern is also shown for the fundamental transverse mode (lower panel)...19

Figure 2.5: Density of states vs. energy relationships for laser active regions with different dimensionality. Carriers are free to move without quantum confinement in three (bulk), two (well), one (wire), or zero (dot) dimensions. These spatial configurations are referred to as 3-D, 2-D, 1-D, and 0-D material structures (from left to right). 21

Figure 2.6: Schematic of a three-layer slab waveguide. 23

Figure 2.7: Graphical solution of the characteristic equations for even TE modes. The normalized wave vector parameters are equal to the points of intersection between the two equations at specific values of OCL thickness. 25

Figure 2.8: Narrow-stripe ridge waveguide laser. 26

Figure 2.9: Ray optics picture of a WGM as it travels around a dielectric cavity ($n_2 > n_1$) and in so doing experiences multiple TIR events. 27

Figure 2.10: Geometry and parameters for a *μ-Disk* laser cavity...........................28

Figure 2.11: Radial intensity profiles for two different TM polarized modes confined within a Gallium Nitride *μ-Disk* cavity with R_0 = 2.5 μm and n = 2.65. ..29

Figure 3.1: Schematic cross-section of AlGaAs/GaAs QW laser structure (right hand side) and corresponding SEM image (left hand side). The SEM image was taken (after cleaving and staining the sample) using the LEO 1550 instrument at Virginia Tech. 37

Figure 3.2: SIMS depth profiles of the alloy constituents (Al, Ga, As) and the doping species (Mg, Se) in the AlGaAs/GaAs QW laser structure. These measurements were made using the Cameca IMS 7f GEO instrument at Virginia Tech...38

Figure 3.3: Cross-section of the WGM laser structure with oxide as the current blocking region. 39

Figure 3.4: Plan-view drawing of full-circle *(FC)* optical cavity. 41

Figure 3.5: Plan-view drawing of partial-circle *(PC)* optical cavities: (a) ¾-circle, (b) ½-circle, and (c) ¼-circle dielectric structure. 42

Figure 3.6: Plan-view drawing of spiral *(Sp)* optical cavity. 43

Figure 3.7: Optical image of WGM laser mask designed at Virginia Tech using L-edit software from Tanner Research. The photo-mask was manufactured by Image Technology using advanced optical lithography techniques. 44

Figure 4.1: Apparatus for measuring I-V curves under CW excitation.................47

Figure 4.2: Apparatus for measuring I-V curves under PW excitation.................48

Figure 4.3: Comparison of I-V data acquired under both CW and PW conditions at 300 K. The DUT was a commercial laser diode (NVG D650-5). The resistance values shown in the legend correspond to *R* in the current divider circuit.............49

Figure 4.4: Apparatus for measuring L-I curves under CW excitation.................50

Figure 4.5: Apparatus for measuring L-I curves under PW excitation. 52

Figure 4.6: Input (current) and output (detector) waveforms from a typical pulsed-wave L-I measurement run. The current source pulses were 2 μs in duration with a repetition frequency of 200 Hz. The pulses delivered to the resistor network were swept from 0.8 to 3.2 A which corresponds to bias currents ranging from 8 to 32 mA. The DUT was a NVG D650-5 laser diode..53

Figure 4.7: L-I data recorded under both CW and PW conditions at 300 K. The DUT was a NVG D650-5 laser diode. The reference CW data were plotted using the *Y-axis* labeled “light power” on the left hand side. The original PW data were plotted against “detector voltage” (right hand side). The solid line represents the corrected PW curve with its *Y-axis* values in mW. 54

Figure 4.8: Apparatus for measuring optical spectra under CW excitation. 55

Figure 4.9: Spectral radiant flux measurements under PW excitation at 300 K. The DUT is an oxide-confined AlGaAs/GaAs QW spiral laser fabricated at Virginia Tech. The nominal radius of the spiral cavity is 250 μm and the width of the p-metal contact ring is 25 μm. The laser material used to fabricate this device is identical to that described in Chapter 3 of this manuscript................................56

Figure 4.10: I-V data recorded using CW drive conditions at 300 K. The DUT is an oxide-confined AlGaAs/GaAs QW spiral laser fabricated at Virginia Tech. The nominal radius of the spiral cavity is 250 μm and the width of the p-metal contact ring is 25 μm. The laser material used to fabricate this device is identical to that described in Chapter 3 of this manuscript. 61

Figure 4.11: I-V data recorded using CW drive conditions at 300 K. The DUT is an oxide-confined AlGaAs/GaAs QW spiral laser fabricated at Virginia Tech. The

nominal radius of the spiral cavity is 250 μm and the width of the p-metal contact ring is 25 μm. The laser material used to fabricate this device is identical to that described in Chapter 3 of this manuscript. 63

Figure 4.12: L-I data recorded under PW (symbols) and CW (solid line) excitation at 300 K. The DUT is an edge-emitting AlGaAs/GaAs QW laser diode with a p-contact stripe width of 100 μm and a cavity length of 1000 μm. 65

Figure 4.13: Optical spectra recorded under CW excitation at 300 K. This laser diode was fabricated in 1995 by an industrial collaborator using material nearly identical to that described in Chapter 3 of this manuscript. 66

Figure 5.1: 3-D view of *test structure* used during wet and/or dry etching runs. The materials of construction are GaAs and photoresist. The relevant low-index FCC crystal planes are labeled using standard notation. 70

Figure 5.2: SEM images of sidewall profiles for test structures patterned using wet etching. The photoresist stripe orientation was parallel (a) or perpendicular (b) to the [011] crystal direction. 71

Figure 5.3: AZ 9260 profiles after soft-baking, UV exposure and development, followed by hard-baking. In (a) SB was performed at 100 °C for 1 min and in (b) SB = 115 °C for 3.5 min. In both cases, the HB step was done at 120 °C for 5 min. 74

Figure 5.4: AZ 9260 profiles after completing both *PR* mask definition and dry etching processes. In (a) SB was performed at 100 °C for 1 min and in (b) SB = 115 °C for 3.5 min. In both cases, the HB step was done at 120 °C for 5 min. 75

Figure 5.5: SEM images of sidewall profiles from the ICP etching study performed on GaAs test structures. Only four of the seven process runs listed in Table 5.1 are shown here for brevity: (a) Run # I-1, (b) I-5, (c) I-3, and (d) I-4...........................77

Figure 5.6: SEM images of sidewall roughness from ICP etching study on (100) GaAs substrates: (a) maximum and (b) minimum roughness. 78

Figure 5.7: SEM images of side-wall profiles from the ICP etching study performed on AlGaAs/GaAs QW laser structures. Only four of the five process

runs listed in Table 5.3 are shown here for brevity: (a) Run # II-1, (b) II-3, (c) II-4, and (d) II-5. 80

Figure 5.8: Electrical characteristics from preliminary study of p-side (Ti/Au) contact metallization. Annealing times range from 1 ≤ τ_{anneal} ≤ 10 minutes with the temperature held at T_{anneal} = 400 °C (for all cases). 82

Figure 5.9: Electrical characteristics from preliminary study of n-side (Sn/Au) contact metallization. Annealing times range from 1 < τ_{anneal} < 10 minutes with the temperature held at T_{anneal} = 400 °C (for all cases). The insert is a higher resolution plot near the origin of the I-V curve. 83

Figure 5.10: Cross-sectional view of *p-n junction test device* fabricated from AlGaAs/GaAs QW structure during the final phase of metal contact evaluation...84

Figure 5.11: Electrical characteristics for *p-n junction test device* with p-side and n-side metal contacts formed under optimum conditions. Annealing times range from 1 < τ_{anneal} < 10 minutes with the temperature held at T_{anneal} = 400 °C (for all cases). 85

Figure 5.12: Cross-sectional view of two different device embodiments for achieving lateral confinement: (a) oxide-stripe laser and (b) ridge-waveguide laser. 87

Figure 5.13: Cross-sectional view of WGM p-n junction laser with current blocking via hydrogenation within the central region of the structure (not to scale). 88

Figure 5.14: Flow diagram for implementation of hydrogenation process in the Trion Technologies PECVD system at Virginia Tech. 89

Figure 5.15: Electrical characteristics for *hydrogenated p-n junction test device* (HYD) with p-side and n-side metal contacts annealed at 400 °C. Annealing times range from 1 < τ_{anneal} < 10 minutes. 91

Figure 5.16: Electrical characteristics for three *p-n junction test devices* showing the effectiveness of PECVD oxide as a mask against hydrogenation. The metal contacts were annealed in forming gas at 400 °C for 5 min. 92

Figure 5.17: SIMS depth profiles of the hydrogen content in the reference sample (after annealing of metal contacts) and hydrogenated sample (before annealing of metal contacts). 93

Figure 6.1: Side-view drawing of WGM laser structure after completing the fabrication process. 100

Figure 6.2: SEM images (upper panels) and CCD photographs (lower panels) of two GaN *μ-Pillar* cavities fabricated by dry etching. 103

Figure 6.3: SEM image of GaAs sidewall (left) and planar surface (middle) prepared by ICP etching. The AFM image (right) provides an estimate of the actual surface roughness with $R_a = 6.02$ nm. 104

Figure 6.4: Schematic of a gain guided laser. 106

Figure 6.5: Schematic of an index guided laser. 106

Figure 6.6: SEM image of a semiconductor ring laser with an integrated Y-junction out-coupler (Reprinted with permission from M. C. Shih *et. al.*, Appl. Phys. Lett., vol. 66, pp. 2608-2610 (1995). Copyright [1995], American Institute of Physics). 111

Figure 6.7: Plan-view drawing of a laterally coupled ring resonator in (a) and a vertically coupled structure in (b). 112

Figure 6.8: Plan view drawing of a spiral-shaped WGM laser 113

List of Tables

Table 3.1: Material design parameters for the AlGaAs/GaAs QW laser structure. 36

Table 5.1: Parameters for ICP etching study on (100) GaAs substrates (etching time = 4 min). 76

Table 5.2: Average values and standard deviations for key physical observables associated with the optimized ICP etching process. 78

Table 5.3: Parameters for ICP etching study on an AlGaAs/GaAs QW laser structure (ICP power = 320 W / chamber pressure = 10 mTorr). 79

1. INTRODUCTION

1.1. Historical Perspective

Over the last five decades, the world has witnessed continuous improvements in size, speed, and complexity of electronic devices and circuits, spurred on by an endless stream of new applications. Compact, lightweight, and robust electronic systems have been made possible by integrating on the same chip large numbers of tiny *active* devices, such as MOSFETs and BJTs, with other *passive* components (resistors, capacitors, inductors). Over the past few years, however, it has become increasingly difficult to further advance the speed and size of electronic devices because we are approaching their fundamental limits of performance. One potential solution to this dilemma is to *replace electronics with photonics* whenever circumstances make this practicable.

The term "photonics" refers to devices capable of manipulating, transferring, and/or storing photons as a means of executing higher level tasks. There are some clear advantages to working with photons to perform data and/or signal processing functions. It is now possible to generate optical pulses that are only several tens of attoseconds in duration (50 to 90 x 10^{-18} seconds!), much shorter than anything comparable in electronics [1]. Light waves with frequencies in the range of 200 to 600 THz can be used as carriers for ultra-high-speed signals, well beyond what is possible using electronics. An optical waveguide can transport multiple data streams (each at a different signal wavelength) within a common transmission channel, something not possible with electronic interconnects. Just as with its electronics predecessor, the evolution of photonics is now being enabled by critical semiconductor device technologies – lasers, waveguides, modulators, switches, and detectors – which are combined using integrated-circuit-style processing to build sophisticated circuits and systems. *The focal point of this Ph.D. research is one such form of integrated photonic device; namely, a whispering gallery mode (WGM) semiconductor laser.*

The word *LASER* is really an acronym for the phrase "*L*ight *A*mplification by *S*timulated *E*mission of *R*adiation." In general terms, a laser consists of a *gain medium* – which may take

the form of an atomic gas, liquid solution, or solid-state slab of material – located within some type of *resonant cavity*. The gain medium must be driven or "pumped" into an excited state using one of several forms of energy (chemical, electrical, optical) after which it decays back to its ground state by releasing optical energy (i.e., emitting photons). The resonant cavity "stores" some of this optical energy (i.e., the photon population increases in the resonant modes of the cavity). Under steady-state pumping conditions, the electrons of the gain medium and the photons inside the cavity interact via three related but distinct mechanisms. These electron/photon interactions – *referred to as radiative transitions* – are illustrated in Fig.1.1.

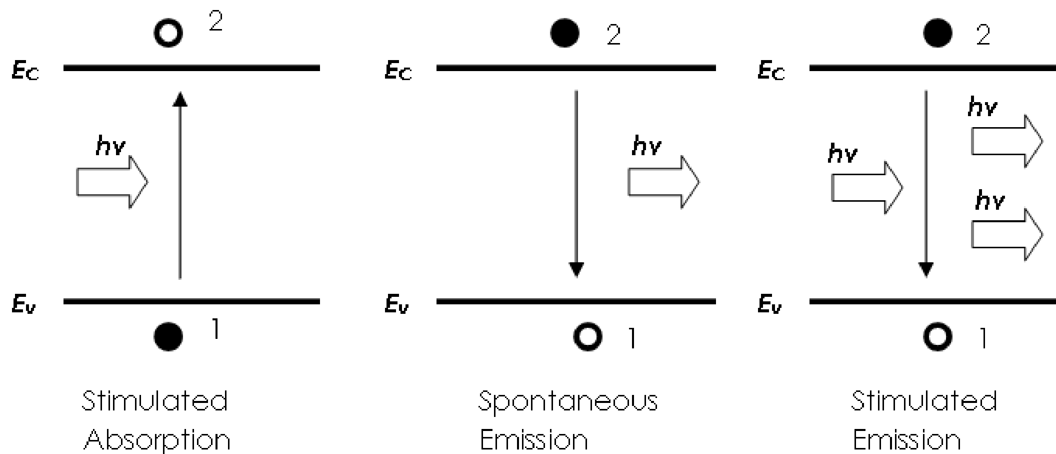

Figure 1.1: Schematics for the three basic radiative transitions envisioned by Einstein in 1929.

During a *stimulated emission* event an incident photon induces an "excited-state" electron to return to its lower energy or "ground" state after which a new photon is created with the same polarization and phase as the original photon. In the *stimulated absorption* process an incident photon induces a "ground-state" electron to occupy a higher energy or "excited" state thereby annihilating the photon. During a *spontaneous emission* event an excited-state electron returns to its ground state accompanied by the creation of a photon with random polarization and phase. Since the two *stimulated* mechanisms require the presence of electrons *and* photons, their corresponding transition rates depend on the populations of both particles. The expression "net stimulated emission" refers to the algebraic difference between the rates of stimulated emission and absorption.

In the case of a semiconductor laser, two conditions must be satisfied before net stimulated emission prevails over spontaneous emission. First, the electron concentration near the bottom of the conduction band must be larger than at the top of the valence band. This state of *population inversion* is achieved in a p-n junction by injecting electrons from the n-side and holes from the p-side into the active region. Next, the photon density in select electromagnetic modes must be built up by high-level pumping and/or optical wave guiding. If optical feedback is provided in the form of highly reflecting mirrors located at either end of a linear cavity, i.e., a *Fabry-Perot* resonator, then photons bounce back and forth between the mirrors and eventually contribute to net stimulated emission. Coherent light is coupled out of the cavity through one or both of the mirrors. *Self-sustained oscillations or lasing* occurs when the optical gain inside the cavity equals the sum of the internal optical losses plus the "useful" light output through the mirrors.

The earliest and still most ubiquitous type of semiconductor lasers have been configured as edge-emitting (*EE*) devices – that is, current flows in the direction parallel to the surface normal and light is emitted in a perpendicular direction from the edge of the structure. In its simplest embodiment the *Fabry-Perot* cavity of an *EE* laser is formed by cleaving the semiconductor material through two parallel crystallographic planes (facets) separated from one another by a distance known as the cavity length. It is not possible to integrate this kind of laser with other light wave elements on a single substrate, because the structure is discontinuous at the facets. Therefore, in order to fabricate photonic integrated circuits, it is necessary to provide optical feedback by some other means. One solution to this problem is the design of "traveling-wave" lasers with circular resonant cavities that can be formed without cleaving the semiconductor wafer.

The first discussion of wave guiding along a curved boundary dates back to 1912, when Lord Rayleigh observed acoustic waves clinging to the dome of St. Paul's Cathedral in London. He found that a whisper close to the edge of the inner side of the dome could be heard easily by a person standing at the opposite side of the vault, hence the name "whispering gallery." Lord Rayleigh also noticed that a person standing in the center of the dome was not able to hear the

very same whisper! The explanation for this phenomenon is that the dome functions as a excellent conduit for acoustic waves traveling along its periphery [2]. Figure 1.2 [3] shows a plan view image of St. Paul's Cathedral in London where Lord Rayleigh observed acoustic waves clinging to the dome. These observations *define* the nature of wave propagation in whispering gallery modes (WGMs) – that is, the primary maxima of wave intensity is localized near the outermost boundary of a structural cavity with circular or spherical symmetry. In the present context, we concern ourselves with optical waves traveling within a semiconductor cavity of pure circular symmetry and/or small perturbations thereof.

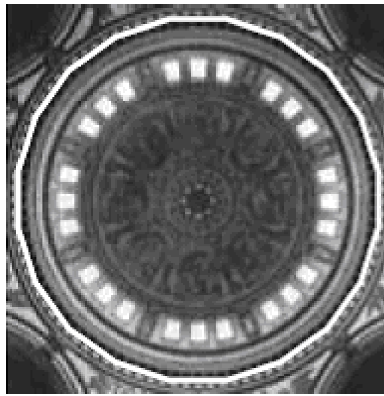

Figure 1.2: Plan view image of St. Paul's Cathedral in London. The solid white line traces out the circular propagation path of an acoustic wave confined at the periphery of the dome (http://www.explore-stpauls.net/oct03/textMM/DomeConstructionN.htm).

The first applications of curved waveguides were in microwave technology in the 1930's and 1940's. Towards the end of the 1960's, curved waveguides were considered for optical applications, essentially scaled down versions of their microwave counterparts [4]. A half-ring semiconductor laser was first realized in 1970, in the form of a zinc-diffused GaAs homojunction laser [5]. An electrically pumped, full-ring semiconductor laser was demonstrated in 1977 [6]. In this case, lasing was evidenced by collecting light scattered off the etched semiconductor sidewalls as no provisions were made for directional output coupling. The first full-ring laser involving a Y-junction output coupler was reported in 1980 [7]. Thereafter these same workers pursued more vigorously half-ring and quarter-ring resonators to avoid complications arising from the "impendence mismatch" introduced by the Y-junction. A few years later, a detailed

investigation of laser geometries and fabrication issues was published [8]. Notwithstanding such advances, ring lasers were still impractical owing to their high threshold current (I_{th} > 100 mA) which eliminated the possibility of continuous-wave (CW) operation at 300 K. Further improvements in materials synthesis and device processing eventually led in 1990 to a full-ring laser operating CW at room-temperature [9].

A common attribute of these early semiconductor ring lasers was their curved "rib waveguide" structure and relatively large cavity size (many tens of microns). This trajectory was *disrupted* in the early 1990's by the pioneering work of Slusher and colleagues at Bell Laboratories on micrometer-sized dielectric disks and rings [10]. The promise of *μ-disk* lasers hinges on the nexus of small gain volumes with high-quality optical cavities. These two factors should result in low threshold current and thus low power consumption. Their planar nature makes it particularly easy to cascade many devices on a single chip [11-13]. The wide range of functionality reported to date, including optical channel add-drop filters, multiplexers and demultiplexers [14-16], high-order filters [17-21], wavelength-selective reflectors [22-24], lasers [10,25-26], and modulators [27,28], is a testament to their versatility. Given these attributes, it should be no surprise that *μ-disk* lasers are now considered to be ideal candidate light sources for high-density photonic integrated circuits [29].

1.2. Problem Statement

There are two technical barriers that must be overcome before it becomes practical to accomplish various signal and data processing tasks using photonic integrated circuits based upon micron scale WGM lasers and resonators. The first issue is high power consumption. This can be addressed by lowering the amount of drive current necessary to achieve lasing while simultaneously increasing the optical power coupled into the next circuit element. The second challenge is to achieve directional light emission without sacrificing other key performance metrics.

As mentioned above, there was a good amount of early work done on large semiconductor ring lasers and related devices (100's of microns). Moreover, it is clear that much of the research

community is presently focused on very small micro-cavity structures (less than 2 μm in diameter). There is now ample evidence of the viability of semiconductor optoelectronic devices that are much smaller than the original ring lasers. It is also well known that threshold currents for very small lasers are often dominated by surface recombination and as such these micro-devices have not proven to be very useful to date.

It is our considered opinion that the best opportunity for success lies in the middle ground – say lasers and other devices based on *μ-Disk* and *μ-Pillar* cavities with $R_{cavity} \leq 10$ μm. These devices are small enough such that I_{th} should be very low when performance is limited only by theoretical considerations. However, this size range is large enough that careful consideration must be given to issues such as current/carrier confinement and methods for reducing light scattering and out-coupling losses. Furthermore, while many different approaches have been reported for realizing directional light emission, there is definitely room for improvement. The overarching goals of this research are as follows:

1. *Demonstrate in a quantitative fashion that device design and processing parameters have an enormous impact on key performance metrics for WGM lasers with μ-Pillar cavities.*

2. *Demonstrate in a quantitative fashion that WGM lasers with novel spiral cavities present the best alternative to existing approaches for light output coupling.*

1.3. Technical Objectives

The specific technical objectives for this work are given below. A detailed discussion of our progress on each of these research directions is presented in Chapters 2 through 6 and a summary of our accomplishments is given in Chapter 7.

1. *Develop and optimize the requisite process technology for making WGM lasers. Key focal points included optimizing techniques for cavity formation via dry etching and introducing a new approach for current confinement via hydrogenation of acceptors and/or donors.*

2. *Design and calibrate the measurement apparatus necessary for testing WGM lasers. The main challenge was to bring these experimental capabilities on-line for the first time in Prof. Guido's lab at Virginia Tech.*

3. *Improve understanding of the connection between device configuration and performance with regard to key design parameters such as cavity radius, laser stripe width, and proximity of stripe to the cavity sidewall.*

4. *Build and test WGM lasers having cavities with pure cylindrical symmetry and spiral geometry and compare their performance.*

5. *Demonstrate an improvement in light extraction efficiency for spiral cavity lasers by minimizing the electromagnetic mode impendence mismatch at the output coupler.*

1.4. Chapter Overview

CHAPTER 2 is divided into two sections. Overall it provides the technical background for the rest of the thesis and serves as an introduction to the terminology used in other chapters. The first part shows the kinds of semiconductor alloys required in lasers and gives a brief explanation of the role different structural layers play in enhancing their performance. The second part gives an optical mode analysis of edge-emitting lasers in the transverse direction and then moves on to discuss whispering gallery modes in cylindrical waveguides.

CHAPTER 3 is divided into four sections. The first part describes the material structures from which our WGM lasers have been built. The second part gives a brief overview of the device fabrication process used to make oxide-confined device structures. The third part introduces the optical cavity designs used to assess the performance of WGM lasers. Finally, in the fourth part, our photomask design and layout procedures are described to clarify the process flow and to establish the types of WGM lasers under consideration.

CHAPTER 4 is divided into three sections. The first part describes the experimental setups and calibration procedures used throughout this thesis. The second part defines the key metrics used to evaluate laser performance. Finally, in the third part, a methodology is introduced for extracting useful device parameters from measured I-V, L-I, and spectral data.

CHAPTER 5 is divided into three sections. The first part shows that our fabrication methods can be used to form high-quality optical cavities in the *μ-Pillar* geometry. The second part describes the preparation and characterization of low-resistance ohmic contacts. The third part demonstrates the current blocking capability of our new hydrogenation process.

CHAPTER 6 is divided into three sections. In the first part, we describe the impacts of optical diffraction and scattering, current and carrier confinement, and surface recombination on the electrical and optical characteristics of WGM lasers. In the second part, we show different methods for extracting light from WGM-like and discuss their impact on laser performance. The third part demonstrates the ability to use WGM lasers in photonic integrated circuits.

CHAPTER 7 summarizes the key elements of this overall body of work and presents our most important conclusions regarding the success of the research as well as the opportunities for further advances in scientific knowledge and practical device technology.

References

[1] P. M. Paul, E. S. Toma, P. Breger, G. Mullot, F. Auge, P. Balcou, H. G. Muller, and P. Agostini, " Observation of a train of attosecond pulses from high harmonic generation," *Science*, vol. 292, pp. 1689-1692 (2001).

[2] Lord Rayleigh, "The problem of the whispering gallery," Scientific Paers, Cambridge University, vol. 5: pp. 617 (1912).

[3] http://www.explore-stpauls.net/oct03/textMM/DomeConstructionN.htm

[4] E.A.J. Marcatili, "Bends in optical dielectric guides," *Bell Systems Technical Journal,* vol. 48, pp. 2103 (1969).

[5] J.A. Carra, L.A.D'Asaro, J.C. Dyment, and G.J. Herskowitz, "GaAs lasers utilizing light propagation along curved junctions," *IEEE Journal of Quantum Electronics,* vol. 6, pp. 367 (1970).

[6] N. Matsumoto, and K. Kumabe," AlGaAs-GaAs Semiconductor Ring Laser ,"*Jpn. J. Appl. Phys.*, vol. 16, pp. 1395-1398 (1977).

[7] A.S.H. Liao, and S. Wang, "Semiconductor injection lasers with a circular resonators," *Applied physics Letters,* vol. 36, pp. 801 (1980).

[8] A. F. Jezierski, and P. J. R. Laybourn, "integrated semiconductor ring lasers,"*IEE Proceedings*, vol. 135, pp. 17 (1988).

[9] T. Krauss, P. J. R. Laybourn, and J. Roberts, "CW operation of semiconductor ring lasers," *Electronic Letters*, vol. 36, pp. 2095 (1990).

[10] S. L. McCall, A. F. J. Levi, R. E. Slusher, S. J. Pearton, and R. A. Logan, "Whispering-gallery mode mirodisk lasers," *Applied Physics Letters*, vol. 60, pp. 289-291 (1992).

[11] S. T. Chu, B. E. Little, W. Pan, and Y. Kokubun, “A cross-grid array of microresonators for vcery large scale integrated photonic circuits,” *presented at Conference on Lasers and Electro-Optics*, San Francisco, CA (1999).

[12] B. E. Little and S. T. Chu, “Microring resonators for very large scale integrated photonics,” *presented at IEEE Lasers and Electro-Optics Society, 12th Annual Metting*, Baltimore, MD (1999).

[13] B. E. Little and S. T. Chu, “The application of microresonators in large scale optical signal processing circuits,” *Laser Resonators III* (2000).

[14] B. E. Little, S. T. Chu, and H. A. Haus, “Micro-ring resonator channel dropping filters,” *presented at IEEE Lasers and Electro-Optics Society, 8th Annual Meeting* (1995).

[15] S. T. Chu, B. E. Little, W. Pan, T. Kaneko, S. Sato, and Y. Kokubun,” An eight-channel add-drop filter using vertically coupled microring resonators over a cross grid,” *IEEE Photonics Technology Letters,* vol. 11, pp. 691-693 (1999).

[16] S. J. Choi, P. Zhen, Y. Qi, C. Sang Jun, and P. D. Dapkus, “8-channel tunable MUX/DEMUX using vertically coupled active microdisk resonators,” *2003 IEEE LEOS Annual Meeting Conference Proceedings (IEEE Cat. No. 03CH37460)* (2003).

[17] R. Orta, P. Savi, R. Tascone, and D. Trinchero, “ Synthesis of multiple-ring-resonator filter for optical systems,” *IEEE Photonics Technology Letters*, vol. 7, pp. 1447-1449 (1995).

[18] S. T. Chu, B.E. Little, W. Pan, T. Kaneko, and Y. Kokubun, “Second order filter response from parallel coupled glass microring resonators,” *IEEE Photonics Technology Letter*s, vol. 11, pp. 14261428 (1999).

[19] B. E. Little, S. T. Chu, J. V. Hryniewicz, and P. P. Absil, “Filter synthesis for periodically coupled microring resonators,” *Optics Letters*, vol. 25, pp. 344-346 (2000).

[20] R. Grover, V. Van, T. A. Ibrahim, P. P. Absil, L. C. Calhoun, F. G. Johnson, J. V. Hryniewicz, and P. –T. Ho, "Parallel-cascaded semiconductor microring resonators for high-order and wide-FSR filters*,"* *Journal of Lightwave Technology*, vol. 20, pp. 900-905 (2002).

[21] B. E. Little, S. T. Chu, P. P. Absil, J. V. Hryniewicz, F. G. Johnson, F. Seiferth, D. Gill, V. Van, O. King, and M. Trakalo, " Very high-order microring resonator filters for WDM application," *IEEE Photonics Technology Letters*, vol. 16, pp. 2263-2265 (2004).

[22] P. P. Absil, J. V. Hryniewicz, B. E. Little, F. G. Johnson, and P. T. Ho," Wavelength selective mirror using notched mirroring resonators," *LEOS 2001. 14th Annual Meeting of the IEEE Lasers and Electro-Optics Society (Cat. No. 01CH37242)* (2001).

[23] J. K. S. Poon, J. Scheuer, and A. Yariv," Wavelength-selective reflector based on a circular array of coupled mirroring resonators," *IEEE Photonics Technology Letters*, vol. 16, pp. 1331-1333 (2004).

[24] G. T. Paloczi, J. Scheuer, and A. Yariv, " Compact mirroring-based wavelength-selective inline optical reflector," *IEEE Photonics Technology Letters*, vol. 17, pp. 390-392 (2005).

[25] S. M. K. Thiyagarajan, D. A. Cohen, A. F. J. Levi, S. Ryu, R. Li, and P. D. Dapkus, " Continuous room-temperature operation of mirodisk laser diodes," *Electronics Letters*, vol. 35, pp. 1252-1254 (1999).

[26] C. Seung June, P. Zhen, Y. Qi, C. Sang Jun, and P. D. Dapkus," Eight-channel microdisk CW laser arrays vertically coupled to common output bus waveguides," IEEE Photonics Technology Letters, vol. 16, pp. 356-358 (2004).

[27] K. Djordjev, C. Seung-June, C. Sang-Jun, and P. d. Dapkus, "Vertically coupled InP microdisk switching devices with electroabsorptive active regions," *IEEE Photonics Technology Letters*, vol. 14, pp. 1115-1117 (2002).

[28] S. Pradhan, B. Schmidt, L. Martinez, Q. Xu, V. R. Almeida, C. Barrios, and M. Lipson," Electro-optic modulator on silicon-on-insulator substrates using ring resonators," *2005 Conference on Lasers and Electro-Optics (CLEO)* (IEEE Cat. No. 05TH8796) (2005).

[29] T. Baba, “Photonic Crystals and Microdisk Cavities Based on GaInAsP-InP System,” *IEEE. J. Sel. Top. Quantum Electron,* vol. 3, pp. 808-830 (1997)

2. TECHNICAL BACKGROUND

Semiconductor lasers have continued to evolve since their invention by four competing research groups in 1962 [1-4]. The first lasers to operate via current injection took the form of GaAs p-n junction diodes with infra-red light emission at λ = 840 nm (in one case the material was a GaAsP alloy emitting visible light at λ = 710 nm [3]. This type of device structure is called a *homojunction laser* because it is made from one homogenous semiconductor material. Lasing was observed from its cleaved facets when the diode was placed under high-level forward bias. In this embodiment, the injected carrier densities decay exponentially with distance from the junction and thus the effective thickness of the gain region depends upon their diffusion lengths. Wave-guiding in the transverse direction is attributable only to the small index change that accompanies the creation of a population inversion (i.e., "gain guiding"), thus the optical field spreads into "non-inverted" regions of the device giving rise to large internal optical losses. As a result of these shortcomings, GaAs homojunction diodes do not exhibit CW lasing above 77 K and their pulsed-wave threshold current densities, J_{th}, are extremely high at 300 K (J_{th}^{300K} > 50 kA/cm^2).

Not long thereafter, the performance of semiconductor lasers was greatly improved by sandwiching the GaAs active region between two AlGaAs layers; i.e., forming an AlGaAs/GaAs double heterostructure (DH). This layer configuration is beneficial for two reasons. First, AlGaAs has a wider band gap than GaAs, and thus it confines electrons and holes to the active region. Second, AlGaAs has a lower refractive index than GaAs, and therefore it establishes a three-layer waveguide with the active region being the optical core. This *double-heterostructure laser* concept was successfully implemented in 1970, as evidenced by several reports of CW operation at 300 K [5-7].

The typical layer construction and device configuration for a "broad-area" DH laser diode is illustrated in Fig. 2.1. It consists of a p$^+$-doped GaAs ohmic contact layer, p-doped AlGaAs upper cladding layer, p- or n-type active region, n-doped AlGaAs lower cladding layer, and finally, an n$^+$-GaAs substrate. The width of the pumped region is defined by the p-contact metal

which extends over the entire surface of the chip. The active region can be made of many different materials as long as it produces enough optical gain to overcome losses within the cavity and from the mirrors. The wavelength at the peak of the stimulated emission spectrum is inversely proportional to the "band gap" of the semiconductor. The semiconductor band gap is the energy difference between the top of the valence band and the bottom of the conduction band. The resonant cavity needed to obtain feedback for self-sustained oscillation is formed by cleaving a pair of [011] crystal facets separated by the distance L_c from the (100) surface-oriented wafer. These semiconductor-air interfaces act as mirrors with approximately 30% reflectivity. To suppress optical feedback, and therefore, lasing in the lateral direction, rough edges are formed by sawing though the device. Coherent light escapes the semiconductor parallelepiped from its cleaved facets.

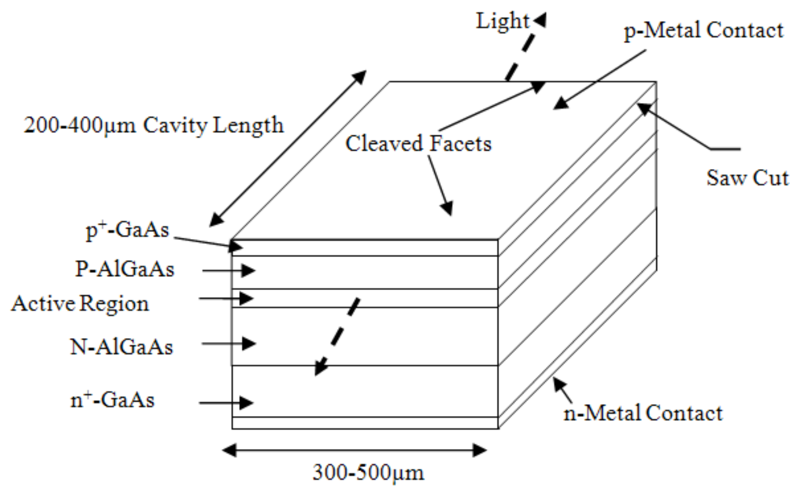

Figure 2.1: Schematic of a broad-area, edge-emitting Fabry-Perot laser.

In Section 2.1, we review the evolution of semiconductor laser structures and discuss the corresponding impact on their electrical and optical performance. Our goal is to present a clear picture of the benefits and weaknesses of the AlGaAs/GaAs QW structure employed throughout this work. In Section 2.2, we describe the types of electromagnetic modes that exist in *EE* semiconductor lasers with *Fabry-Perot* resonators and in cylindrical WGM laser cavities.

2.1. Design Considerations for Diode Lasers

2.1.1. Compound Semiconductor Alloys

All laser diodes in existence today were fabricated from compound semiconductors with *direct* band gaps. Elemental semiconductors such as Si and Ge have *indirect* band gaps and thus exhibit comparatively weak radiative transitions (e.g., the spontaneous emission coefficient for bulk GaAs is about 10^5 times larger than that found in bulk Si or Ge). Compounds made from group-III elements, such as gallium and indium, and group-V elements, such as phosphorus and arsenic, have been of particular interest because their emission wavelengths cover the visible-to-near-infrared range of the electromagnetic spectrum (0.5-1.6 µm). An overview of commonly used III-V semiconductors is given in Fig. 2.2 with their band gap energies plotted as a function of lattice constant [8].

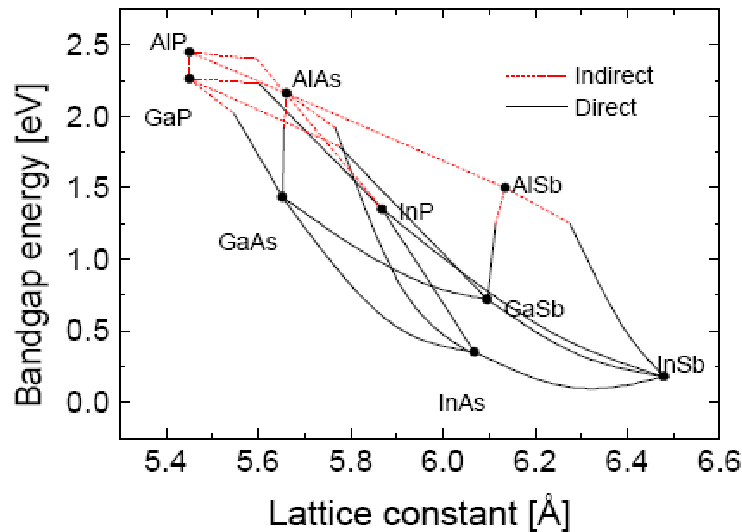

Figure 2.2: Bandgap energy vs. lattice constant for some III-V semiconductors. The plotted data correspond to room temperature values of these physical quantities (Materials catalogue, EPI Materials Ltd., Lancaster Way, Ely, Cambridge-shire, (CB6 3NW UK)).

The solid points correspond to binary compounds, such as GaAs and InAs, while the connecting or "tie" lines represent ternary alloys, such as $In_xGa_{1-x}As$ ($0 \leq x \leq 1$), formed by mixing the two

binary endpoints. The solid and dashed lines denote semiconductor alloys with direct and indirect band gaps, respectively.

Another important consideration is the lattice constants of the materials used to build a typical multi-layer, thin-film laser structure. The various semiconductor layers, most of which are less than 1 μm in thickness, must be grown on a 300 to 450 μm thick substrate for mechanical stability. This material synthesis task is accomplished using any one of several well developed crystal growth techniques [9, 10]; namely, liquid phase epitaxy (LPE), vapor phase epitaxy (VPE), molecular beam epitaxy (MBE), or metal-organic chemical vapor deposition (MOCVD). In order to achieve the highest structural quality all constituent materials must be "lattice-matched" to the substrate – *ideally their lattice constants should be equal at the crystal growth temperature*.

Suitable materials can be found by overlaying a vertical line on Fig. 2.2 with the lattice constant set equal to one of the binary endpoints (substrate wafers are almost always made from binary compounds). One such example is the $Al_xGa_{1-x}As$ alloy system having a lattice constant of about 5.65 Å with energy band gaps ranging from 1.43 to 2.2 eV. Many other choices are in evidence on this laser material "phase diagram" and the realm of possibilities can be broadened still further by considering quaternary alloys. The materials of choice in fiber-optic communication networks are $In_xGa_{1-x}As_yP_{1-y}$ alloys and quantum well structures, grown lattice-matched to InP substrates, because these semiconductors make it easy to design and synthesize lasers with emission wavelengths of 1.3 μm (lowest fiber dispersion) and 1.55 μm (lowest optical loss).

2.1.2. Carrier Injection via P-N Heterojunctions

The action in a semiconductor laser takes place at the junction between two regions with dissimilar impurity doping, namely p- and n-type regions. If there is no voltage drop across the junction, charge carriers are distributed through the crystal in roughly the same way as the impurities. Electrons are the majority carriers throughout the n region, while holes are in the majority in the p region. In equilibrium, without an applied voltage or other external stimulus imposed on the device, the electron and hole diffusion and drift currents sum to exactly zero.

A semiconductor diode is said to be under forward bias, if a positive voltage is applied to the p-side and a negative voltage to the n-side. This attracts the electrons and holes to the opposite sides of the device; that is, these two types of charged particles are injected across the p-n junction and thus become minority carriers (electrons on the p-side and holes on the n-side). Under this biasing condition, there is a non-zero net current flow through the device and electrons and holes may undergo radiative recombination near the junction, thereby releasing photons equal in energy to the semiconductor band gap.

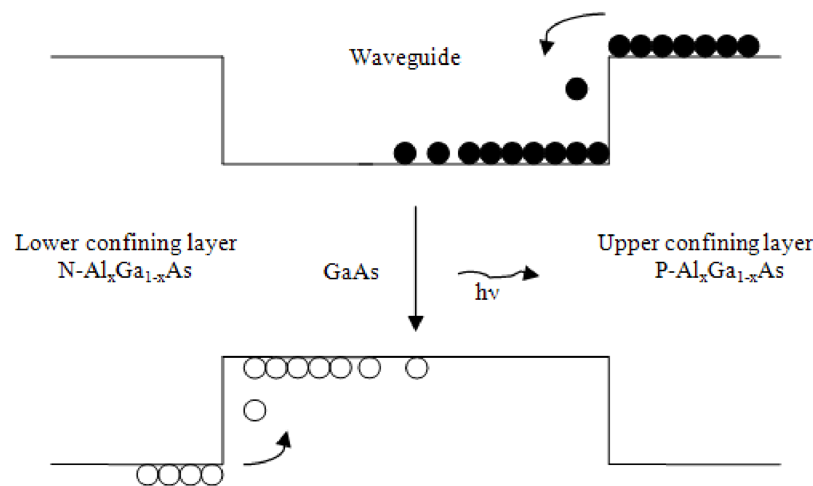

Figure 2.3: Energy vs. distance diagram for a separate-confinement p-n junction heterostructure laser under high forward bias. This state of operation is referred to as “flat-band” since the built-in diode potential is offset by the applied voltage giving rise to a spatially independent energy band structure.

The effect of the two heterojunctions that constitute a DH laser on the spatial distribution of carriers is shown in Fig. 2.3. Injected electrons and holes are confined to the GaAs active region by means of the AlGaAs potential energy barriers, and, as a consequence, recombine within a volume defined by the active region thickness rather than the minority carrier diffusion length. The consequences of this design change can be quite significant. For example, the minority carrier diffusion lengths in lightly doped GaAs range from 2 to 10 μm while the active layer thickness in a DH laser is typically between 0.2 and 0.5 μm. Therefore, at the same value of injection current, the carrier density in a DH active region is much higher than for its

homojunction laser counterpart. The inverse relationship also holds true; that is, the drive current necessary to reach a particular carrier density should be lower for a DH laser than for the homojunction case. If we now assume that the gain vs. carrier density relationships and optical losses are the same, then the threshold current should be considerably lower for the DH laser. Typical values of I_{th}^{300K} for AlGaAs/GaAs DH lasers are in the 1 to 3 kA/cm^2 range, more than 10x lower than the best results for GaAs homojunction lasers.

2.1.3. Separate Confinement Heterostructures

In a conventional DH laser structures, the gain medium or active region could be made thinner to reduce the volume of material that must be "inverted" by the injection current. Doing so, however, would also cause the optical intensity profile for the fundamental transverse mode to redistribute itself with a larger fraction overlapping with the p- and n-doped cladding layers. In other words, the magnitude of the transverse optical confinement factor, Γ_y, would decrease and thereby exert a counteracting influence on the threshold current. It can be shown using the analysis presented in Appendix D that Γ_y would begin to decrease precipitously as the active region thickness approaches the range where quantum effects become important.

This problem can be mitigated by using the *separate confinement heterostructure* design [11]; that is, an optical confinement layer or OCL can be added to the structure so as to introduce an alternative optical core for transverse wave guiding. A schematic energy band vs. position diagram for a five-layer separate confinement heterostructure (SCH) laser is presented in the upper panel of Fig. 2.4, with the corresponding refractive index profile shown in the lower panel. It is clear that the OCL, represented by b, is considerably thicker than the active region, denoted by a. If the a-to-b ratio was small enough then the effective index of the active region plus OCL composite would be very close to that of the OCL material alone. Thus, changes in the active region thickness would not have a significant impact on the shape of the optical mode itself and Γ_y would be directly proportional to a instead of having the super-linear relationship expected for DH lasers.

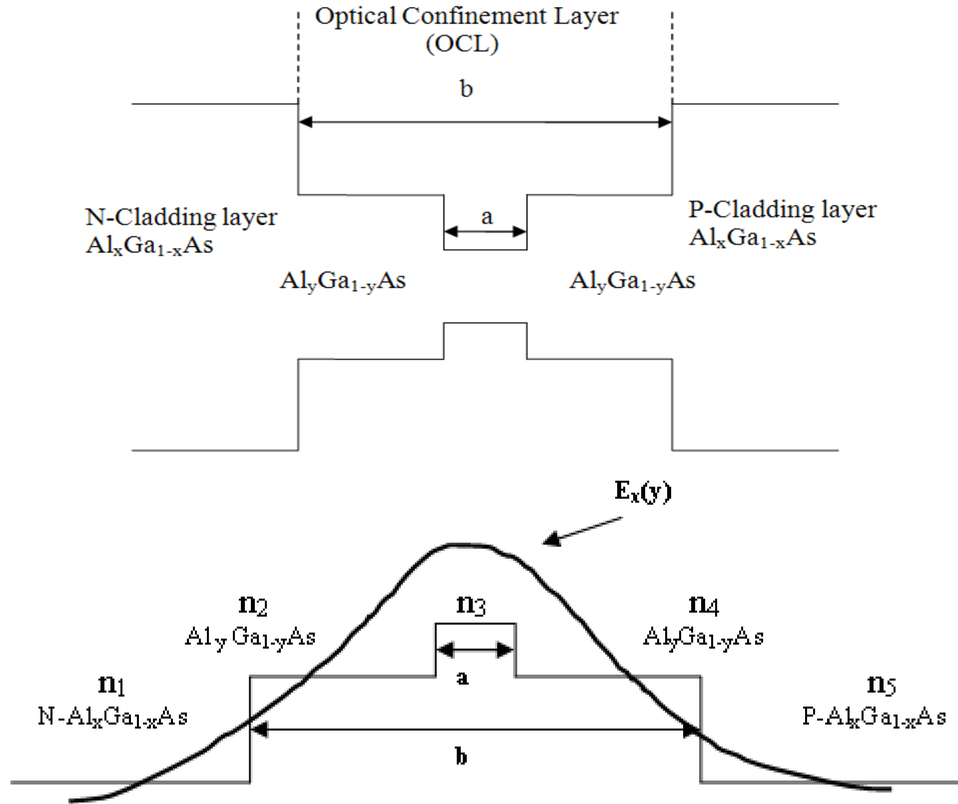

Figure 2.4: Energy vs. position diagram (upper panel) and corresponding refractive index profile (lower panel) for a separate-confinement heterostructure laser. The optical intensity pattern is also shown for the fundamental transverse mode (lower panel).

The SCH laser design also provides additional flexibility with regard to minimizing propagation losses. In order to reduce free carrier absorption, both the OCL and active layer can be made from non-doped semiconductor materials for which every effort has been put forth to eliminate contamination by residual impurities. We note that initial demonstrations of high transparency GaAs waveguides were mostly attributable to significant reductions in residual carrier density [12, 13]. The heavily doped n- and p-type cladding layers contribute significantly to the overall free carrier loss. An optical loss of 22 dB/cm was found for n-type GaAs with an electron density of 1 x 10^{18} cm^{-3} [14]. The greater valence band complexity causes even higher absorption in p-type III-V materials [15-19]. An optical loss of 56 dB/cm at λ = 1.3 μm was reported for GaAs-based alloys with p-type doping of 1 x 10^{18} cm^{-3} [19].

High quality epitaxial material is also required to minimize optical scattering losses at interfaces and/or inclusions. Liquid phase epitaxy, historically one of the first useful III-V semiconductor growth techniques, has proven to be less satisfactory in this context. Owing to unavoidable interface roughness, propagation losses are typically≥ 5 dB/cm [20,21], with the lowest reported value of 2 dB/cm [22]. The advent of alternative growth method has greatly reduced this problem. There have been several reports of single-mode or quasi-single mode GaAs-AlGaAs waveguides grown by MOCVD or MBE with propagation losses < 0.3 dB/cm [12, 13, 23, 24].

Finally, we mention that the upper and lower cladding layers must be of sufficient thickness to minimize coupling losses to parasitic waveguides running parallel to the plane of the active region. If these bounding layers become too thin, the transverse mode profile may penetrate into the adjacent p^+ or n^+ regions and thus couple into waveguides with such heavily doped layers as their core. Optical energy would then be transferred from the vicinity of the active region into these neighboring waveguides where it would be dissipated via free carrier absorption [25].

2.1.4. Low Dimensional Gain Media

Quantum confinement of electrons and holes within a one-dimensional potential energy well was first demonstrated in 1976 by Raymond Dingle and his colleagues at Bell Laboratories [26]. Since then, quantum well (QW) lasers have become the backbone of fiber-optic communication systems. Semiconductor QW heterostructures consist of a narrow band gap "well" layer surrounded on both sides by a wider band gap "barrier" material. The QW itself is typically less than 100 Å in thickness while the barrier layers are often considerably thicker. The wide band gap material establishes a potential energy barrier on each side of the QW and thereby restricts the "free" motion of carriers within the 2-D plane of the well. Carrier motion perpendicular to the QW plane is *confined* to unique values of the crystal momentum (in this particular direction) and thus the kinetic energy is *quantized* into discrete levels for this one degree of freedom. Consequently, the density of states (DOS) functions for these *quantum-confined* electrons and holes [27] morphs into the "2-D like" formulation depicted in Fig. 2.5. These same basic arguments would apply, with only qualitative changes, for situations in which carrier motion was

confined in two or three dimensions. Figure 2.5 compares the DOS functions for different carrier confinement geometries (four possibilities exist in three-dimensional space).

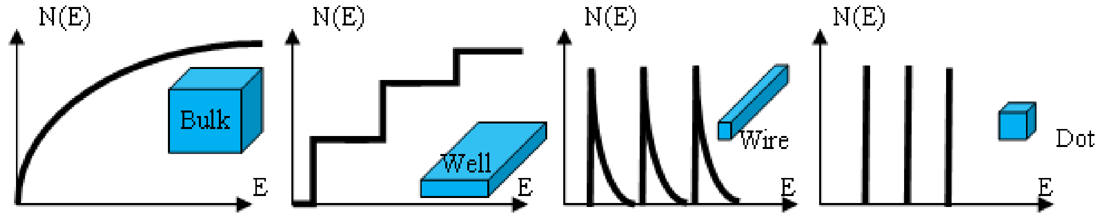

Figure 2.5: Density of states vs. energy relationships for laser active regions with different dimensionality. Carriers are free to move without quantum confinement in three (bulk), two (well), one (wire), or zero (dot) dimensions. These spatial configurations are referred to as 3-D, 2-D, 1-D, and 0-D material structures (from left to right).

It is reasonable to expect that such modifications to the DOS function would have an impact on laser performance. As an example, we note that typical values of J_{th} for bulk and QW lasers held at room-temperature are 1500 and 300 A/cm^2, respectively. Numerous improvements in QW laser characteristics – such as lower threshold current, higher efficiency, higher modulation band-width and lower dynamic spectral line width – were predicted theoretically in the mid 1980's [28-32]. All of these claims have been confirmed experimentally over the past 25 years [33].

Since the electronic states in a quantum dot (QD) are discrete in nature, fewer charge carriers are necessary to create a population inversion. Thus, the carrier density at which lasing occurs should be considerably lower in QD structures compared to either quantum wire or quantum well lasers. Arakawa and Sakaki [34] first predicted that reducing the dimensionality of the laser active region from 3-D to 0-D would give rise to a significant decrease in the magnitude of J_{th} and make it independent of temperature. In the present work, we have focused our attention on conventional QW laser structures; nonetheless, all of the device fabrication technology and cavity design concepts introduced in Chapters 3 through 6 should be applicable with little modification to more advanced and potentially better performing QD lasers.

2.2. Optical Modes in Dielectric Structures

The analytical techniques described in Section 2.2.1 can be applied without modification to determine the properties of transverse modes in our *μ-Pillar* laser structures. In addition, the concept of lateral electrical/optical confinement introduced in Section 2.2.2 plays an important role in WGM lasers. However, given the circular symmetry of the *μ-Pillar* structure, a purely 1-D analytical technique cannot be used to derive its "lateral" mode structure. The topic of electromagnetic modes in cylindrical dielectric cavities is discussed briefly in Section 2.2.3.

2.2.1. Transverse Modes in Slab Waveguides

After taking a quick look ahead at Fig. 3.1 of Section 3.1, it should be obvious that our AlGaAs/GaAs QW material structure is just a modified form of the SCH laser introduced in 1976 by G. H. B. Thompson [11]. The quantum well heterostructure (QWH) version of a SCH device is referred to herein as a *SC-QWH laser*. Schematics of the energy band structure and refractive index profile for the original five-layer SCH laser were presented in Fig. 2.4; however, no information was given about sizes beyond the statement that the OCL thickness, b, is usually much larger than the active region thickness, a. It is important to remember that quantum confinement in semiconductors was demonstrated only months before the publication of Thompson's paper [26]. Five to ten more years would pass before QW lasers began to occupy the curiosity of many researchers.

In its original form, the active region of a SCH laser was relatively thick, with typical values being $a_{bulk} \geq 300$ nm, and the OCL was even thicker [11]. In the present case, however, the active region consists of a GaAs QW with $a_{QW} = 10$ nm and an OCL thickness of 250 nm. Given the large difference between a_{QW} and b_{OCL}, it is reasonable to assume that the QW has little impact on the effective index of refraction seen by an optical wave traveling inside the OCL. In other words, we can ignore the QW with regard to computing the transverse electromagnetic mode profiles without any loss of generality. Note, also, that refractive index is only a weak function of doping so it is justifiable to ignore the small index difference between the p-type (upper) and n-type (lower) $Al_{0.85}Ga_{0.15}As$ cladding layers. At this level of approximation, we have transformed a complex laser structure – with its 7+ layers and changes in alloy composition

and doping type and level – into a much simpler three-layer slab waveguide. By so doing, we have rendered the problem tractable to solution via conventional analytical methods.

The configuration of a three-layer $Al_yGa_{1-y}As/Al_xGa_{1-x}As$ slab waveguide is illustrated in Fig. 2.6, along with the coordinate system referenced throughout the following discussion. Wave propagation occurs along the z-axis, which we refer to as the *longitudinal* direction. The y-axis is parallel to the direction of crystal growth, which we refer to as the *transverse* direction. The x-axis is in the plane of the substrate, and we call it the *lateral* direction.

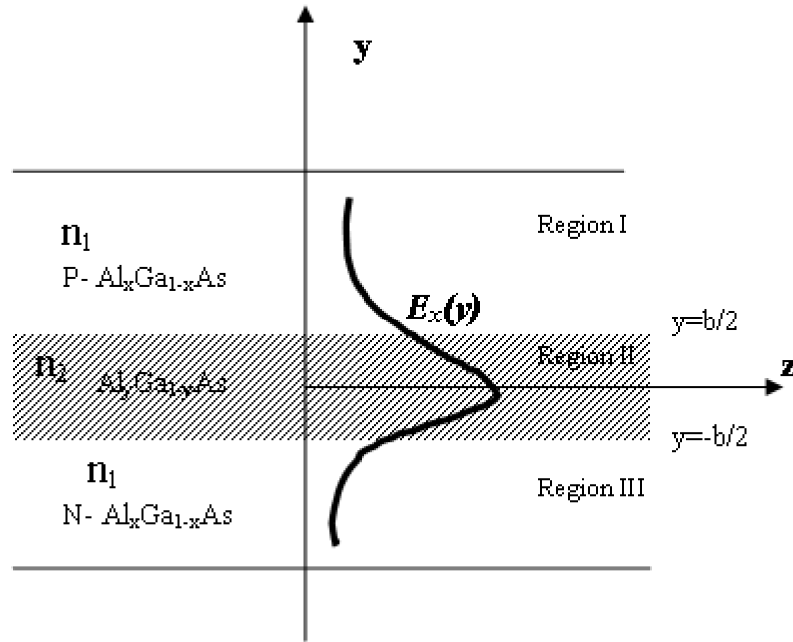

Figure 2.6: Schematic of a three-layer slab waveguide.

For convenience, we restate below the characteristic equations introduced in Appendix A (Eq. A.34 and A.35). In Region II (I) of Fig. 2.6, the symbol χ (γ) represents the y-component of the wave propagation vector and the quantity n_2 (n_1) is the index of refraction.

$$\left(\frac{\chi \cdot b}{2}\right)\tan\left(\frac{\chi \cdot b}{2}\right) = \left(\frac{\gamma \cdot b}{2}\right) \tag{2.1}$$

$$\left(\frac{\gamma \cdot b}{2}\right)^2 + \left(\frac{\chi \cdot b}{2}\right)^2 = \left(\frac{k_o b}{2}\right)^2 \left(n_2^{\,2} - n_1^{\,2}\right) \qquad (2.2)$$

The emission wavelength of our laser device is $\lambda_0 = 795$ *nm* and therefore k_0 can be calculated as shown in Eq. 2.3.

$$k_0 = \frac{2\pi}{\lambda_o} = 7.9 \times 10^4 cm^{-1} \qquad (2.3)$$

In order to find χ and γ, we solve Eq. 2.1 and 2.2 using the graphical method introduced by Collin [35]. Once this has been done, the optical mode profiles can be obtained by substituting these values of χ and γ into the electric field solutions given in Appendix A (Eq. A.27 and A.28).

We now apply this technique, as illustrated in Fig. 2.7, in order to find the even TE waveguide modes for our laser structure. The material parameters were taken from the data base assembled by the *Ioffe Institute* in Russia [36]. We used $n_2 = 3.45$ in the case of $Al_{0.25}Ga_{0.75}As$ and $n_1 = 3.16$ for $Al_{0.85}Ga_{0.15}As$. The relevant values of χ and γ are found at the intersections of Eq. 2.1 and 2.2. Only positive values of ($\gamma \cdot b/2$) are given consideration because negative values imply unguided waves [37]. For b = 0.26, 0.52, and 0.78 μm, circles of radii given by the right side of Eq. 2.2 are shown by the dotted lines in Fig. 2.7. At b = 0.26 μm, an intersection near ($\chi \cdot b/2$)≈ 0.98 is obtained only with the m = 0 curve, which is the solution for the lowest-order or *fundamental* transverse mode. No matter how small b becomes, this mode is never "cut-off" in a symmetric wave-guiding structures [37]. Increasing b to 0.52 μm leads to an intersection close to ($\chi \cdot b/2$) ≈ 1.2 for the m = 0 mode and ($\chi \cdot b/2$) ≈ 3.4 for the m = 2 mode.

It is clear from this analysis that higher order TE even modes can be cut-off simply by making the OCL thin enough such that ($\chi \cdot b/2$) $\leq$ 3.1. Moreover, owing the large *built-in* difference in refractive index between the OCL and cladding layers, the higher order modes should remain cut-off independent of the operating conditions (i.e., drive current and/or junction temperature). All high-performance SC-QWH lasers are now designed in this manner.

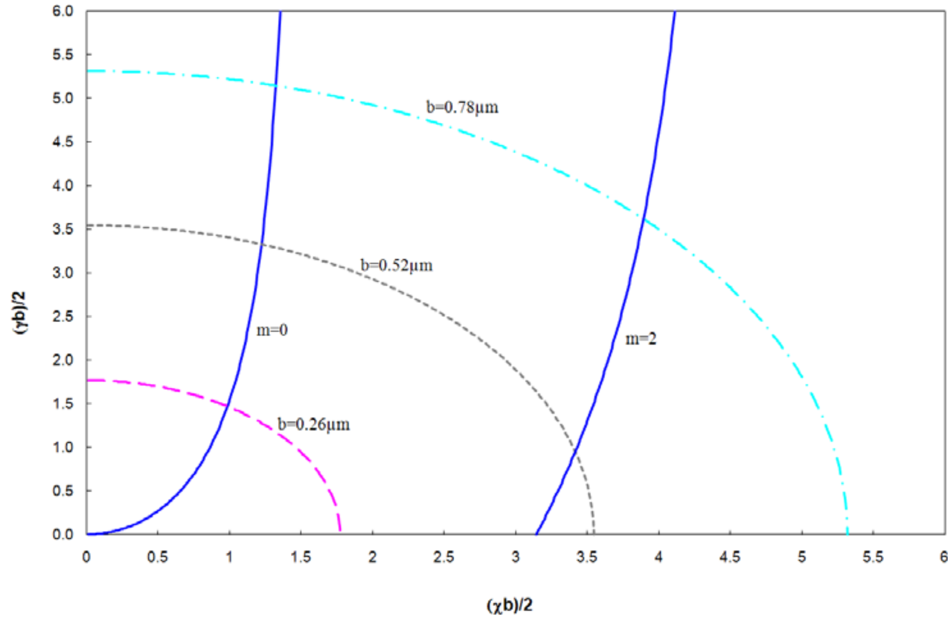

Figure 2.7: Graphical solution of the characteristic equations for even TE modes. The normalized wave vector parameters are equal to the points of intersection between the two equations at specific values of OCL thickness.

2.2.2. Lateral Modes in Ridge Waveguides

In most applications of semiconductor lasers it is desirable to maintain single-mode operation over the widest possible range of drive current and junction temperature. The transverse mode component of the problem is handled as described above via proper layer design and material synthesis. The *lateral mode* issue can be addressed by patterning the laser material (before and/or after crystal growth) into a narrow "active" stripe. An example of one such form of narrow-stripe laser is shown in Fig. 2.8. In this *ridge-waveguide* structure, the effective active volume is reduced in the lateral direction by removing the p-type AlGaAs upper cladding layer outside the lithographically defined stripe width, W_s, and replacing it with a dielectric material known as polyimide. Therefore, *by design*, current flow is confined to W_s and the lateral optical modes "see" a material (outside the stripe) with a much lower index of refraction.

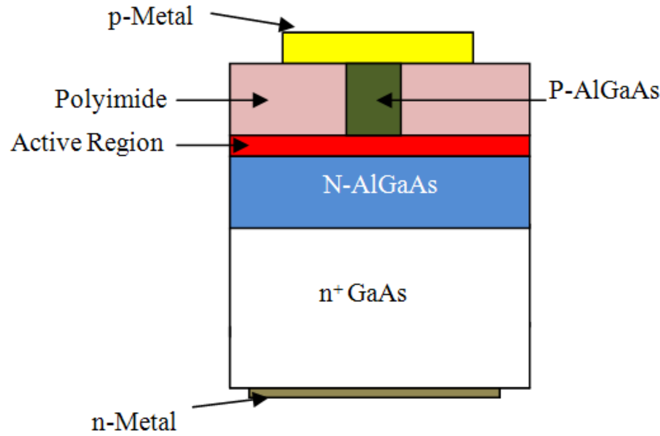

Figure 2.8: Narrow-stripe ridge waveguide laser.

Such complex 2-D waveguide structures must be examined using numerical techniques to obtain truly accurate results. Nonetheless, it is possible to gain considerable physical insight by using a piece-wise 1-D analytical approach known as the effective index method [38-40]. The graphical method of Section 2.2.1 is first applied to each of the three regions that constitute the lateral structure (stripe region made via crystal growth surrounded on both sides by *lateral confining regions* with polyimide capping layers). This effort yields values of the effective modal index, n_{eff}, in all three regions. However, since the structure is symmetric about the center of the stripe, there are really only two different values of n_{eff}. Next, the calculated values of n_{eff} are assigned as material parameters for a heuristic *lateral* three-layer slab waveguide. The solution is finally brought to a close by reapplying the graphical method to estimate the properties of the lateral optical modes.

2.2.3. WGMs in Cylindrical Cavities

The phenomenon of total internal reflection (TIR) of light waves from the sidewalls of a closed dielectric structure is a well known means of optical ray confinement. Consider a microsphere of radius R with refractive index, n_2, surrounded by another material with a smaller refractive index, n_1. According to Snell's law, a light ray undergoes TIR at the boundary between the two media if its angle of incidence, θ_{inc}, satisfies the condition given below

$$\theta_{inc} > \theta_c = \sin^{-1}\left(\frac{n_1}{n_2}\right) \qquad (2.4)$$

The symbol θ_c denotes the critical angle for total internal reflection. At larger angles of incidence the ray remains trapped inside the closed dielectric cavity. The spherical (3-D) or cylindrical (2-D) symmetry of such dielectric structures gives rise to a second observation – namely, that θ_{inc} does not change upon multiple reflections of the ray as it propagates around the periphery, as illustrated in Fig. 2.9.

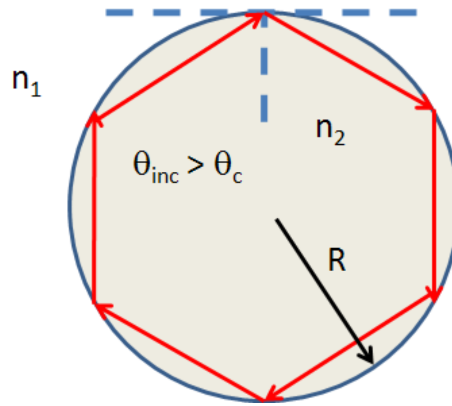

Figure 2.9: Ray optics picture of a WGM as it travels around a dielectric cavity ($n_2 > n_1$) and in so doing experiences multiple TIR events.

In the case of WGMs, the equivalent optical rays circulate near the outer wall of the cavity and thus traverse a distance $\approx 2\pi R$ in one round trip. If one round trip equals an integer number of ray wavelengths, then a standing wave is established with the resonance condition given by Eq. 2.5, where λ/n_2 is the wavelength in the medium [41].

$$2\pi R = n\left(\frac{\lambda}{n_2}\right) \qquad (2.5)$$

A schematic is presented in Fig. 2.10 of a semiconductor *μ-Disk* laser cavity. It consists of a disk-shaped gain medium with thickness d, radius R_o, and refractive index n_1, sandwiched

between two layers of lower refractive index n_3. The dielectric discontinuity along the z-axis strongly confines the fundamental (transverse) mode to the active region. Total internal reflection at the boundary $r = R_0$ establishes WGMs inside the cylindrical cavity [42-44].

The semiconductor *μ-Pillar* structure of interest herein is very similar to this idealized *μ-Disk* cavity except that our SC-QWH material has a pair of p- and n-type AlGaAs cladding layers above and below the optical core (OCL plus QW) which are surrounded on top and bottom by more heavily doped p+ and n+ GaAs contact layers, respectively. As a consequence, the optical confinement factor should be larger in the *μ-Disk* case and free-carrier absorption losses should be higher in the *μ-Pillar* structure.

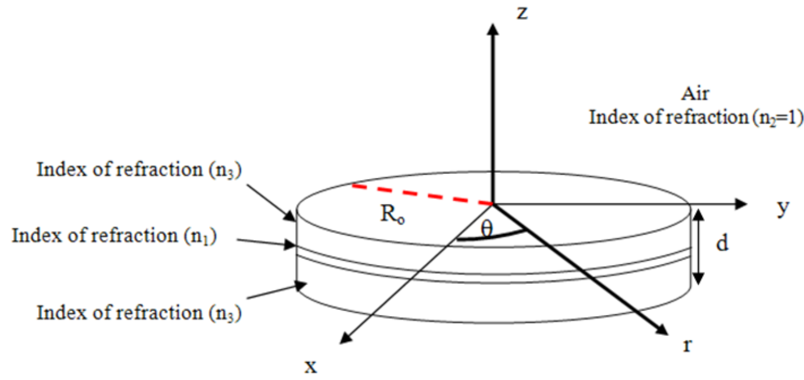

Figure 2.10: Geometry and parameters for a *μ-Disk* laser cavity.

It is necessary to use 2-D numerical techniques to calculate exact optical mode profiles for these *μ-Disk* cavities; however, we can still gain useful physical insight by using much simpler analytical methods. Appendix B provides a detailed accounting of one such solution technique and we summarize the key findings below to enable additional discussion. The z-dependence should follow the slab-waveguide model for TE and TM modes. The fundamental *transverse* mode can be described as *cos(χz)* with $\chi = k_o\sqrt{n_1^2 - n_{eff}^2}$, inside the gain medium (| z | < d/2), and as $e^{-\gamma|z|}$ with $\gamma = k_o\sqrt{n_{eff}^2 - n_3^2}$, within the surrounding material (| z | > d/2). Two mode numbers may be introduced to distinguish various WGM solutions: (1) azimuthal mode number

M reveals the number of wavelengths necessary to make one 360 degree trip around the cavity and (2) radial mode order N corresponds to the number of nodes (N-1) in the radial component of the electromagnetic field. *The value of N is equal to unity for WGMs.* Following the approach given by Rex [45], and limiting the analysis to *in-plane* optical waves with TM polarization only, we have

$$\Phi(r) = \begin{cases} A_M J_M(nkr) & r < R_o \\ H_M^{(2)}(kr) + S_M H_M^{(1)}(kr) & r > R_o \end{cases} \qquad (2.6)$$

where J_M is a Bessel function of the first kind and $H^{(1)}$ and $H^{(2)}$ are Hankel functions of the first and second kind, respectively. Figure 2.11 shows two radial intensity profiles for a GaN *μ-Disk* cavity with R_0 = 2.5 μm and n = 2.65.

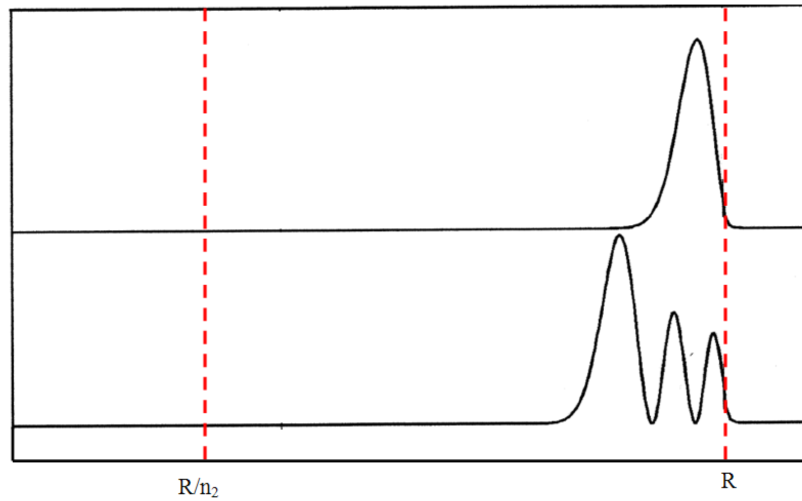

Figure 2.11: Radial intensity profiles for two different TM polarized modes confined within a Gallium Nitride *μ-Disk* cavity with R_0 = 2.5 μm and n = 2.65.

These approximate solutions were found by applying Eq. 2.6 and assuming an emission wavelength of λ = 375 nm (which is typical of bulk GaN at 300 K). The azimuthal and radial mode indices are M = 103 / N = 1 and M = 91 / N = 3 for the upper and lower wave forms, respectively. The whispering-gallery mode (N = 1) intensity maximum is very close to the cavity sidewall and the wave solution approaches zero asymptotically for ≤ 2.2 μm. In contrast, the

higher order radial mode ($N = 3$) extends further into the GaN disk than the WGM and its optical intensity is considerably lower near the cavity sidewall.

Reference

[1] R. N. Hall, G. E. Fenner, J. D. Kingsley, T. J. Soltys, and R. O. Carlson ," Coherent Light Emission From GaAs Junction," *Phys. Rev. Lett.*, vol. 9, pp. 366-368 (1962).

[2] M. I. Nathan, W. P. Dumke, G. Burns, F. H. Dill, Jr., and G. Lasher, "Stimulated Emission of Radiation from GaAs p-n Junctions," *Appl. Phys. Lett.,* vol. 1, pp 62 (1962).

[3] N. Holonyak, Jr., and S. F. Bevacqua, "Coherent (Visible) light emission from $Ga(As_{1-x}P_x)$ Junctions," *Appl. Phys. Lett.,* vol. 1, pp. 82 (1962).

[4] T. M. Quist, R. H. Rediker, R. J. Keys, W. E. Krag, B. Lax, A. L. McWhorter, H. J. Zeigler, "Semiconductor Maser of GaAs," *Appl. Phys. Lett.,* vol. 1, pp. 91 (1962).

[5] I. Hayshi and M. B. Panish, Device Research Conf., Seattle, Washington (1970).

[6] I. Hayashi, M. B. Panish, P.W. Foy, and S. Sumski, " Junciton Lasers which operate continuously at room temperature,"*Appl. Phys. Lett*., vol.17, pp. 109-111 (1970).

[7] Zh. I. Alferov, V. M. Andreev, D. Z. Garbuzov, Yu. V. Zhilyaev, E. P. Morozov, E. L. Portnoi, and V. G. Trofim, *Sov. Phys. Semicond*. vol. 4, p1573. 1970. [Translated from *Fiz. Tekh. Poluprovodn*. vol4. p1826. 1970].

[8] Materials catalogue, EPI Materials Ltd., Lancaster Way, Ely, Cambridge-shire, (CB6 3NW UK)

[9] P.P. Chow, *"Molecular beam epitaxy",* in "*Thin film processes II*", J. L. Vossen and W. Kern, Eds., Academic Press (1991).

[10] T. F. Kuech and K.F.Jensen, "*OMVPE of compound semiconductors*", in "*Thin film processes II*", J. L. Vossen and W. Kern, Eds., Academic Press (1991).

[11] G. H. B. Thompson, G. D. Henshall, J. E. A. Whiteway, and P. A. Kirby, "Narrow-beam five-layer GaAlAs/GaAs heterostructure lasers with low threshold and high peak power," *J. Appl. Phys.*, vol. 47, pp. 1501-1515 (1976).

[12] H. Inoue, K. Hiruma, K. Ishida, T. Asai, and H. Matsumura, "Low loss GaAs optical waveguides,' *J. Lightwave technol.*, vol. LT-3, pp. 1270-1275 (1985).

[13] E. Kapon and R. Bhat," Low-loss single mode GaAs/AlGaAs optical waveguides grown by organometallic vapor phase epitaxy," *Appl. Phys, Lett.* , vol. 50, pp. 1628-1630 (1987).

[14] W. G. Spitzer and J. M. Whelan, "Infrared absorption and electron effective mass in n-type Gallium Arsenide," *Phys. Rev.,* vol. 114, p. 59-63 (1959).

[15] A. A. Ballman, A. M. Glass, R. E. Nahory, and H. Brown, "Double doped low etch pit density InP with reduced optical absorption," *J. Cryst. Growth*, vol. 62, pp. 198-202 (1983).

[16] R. Braunstein and E. O. Kane, " The valence band structure of the III-V compounds," *J. Phys. Chem. Solids*, vol. 23, pp. 1423-1431 (1962).

[17] H. C. Casey, Jr., D. D. Sell, and K. W. Wecht, " Concentration dependence of the absorption coefficient for n- and p-type GaAs between 1.3 and 1.6 eV," *J. Appl. Phys.,* vol. 46, pp. 250-257 (1975).

[18] H. Sano, H. Inoue, Y. Sasaki, H. Nakamura, K. Ishida, and J. M. Glinski, " Low-loss single InGaAs/InAlAs multi-quantum well electroabsorption modulator," In *Tech. Dig. Opt. Fiber Commun. Conf.*, San Fransisco, CA, Jan. 1990, paper WM 15, p. 112.

[19] C. H. Henry, R. A. Logan, F. R. Merritt, and J. P. Luongo," The effect of intervalance band absorption on the behavior of InGaAsP lasers," *IEEE J. Quantum Electron.* , vol. QE-19, pp. 947-952 (1983).

[20] E. Garmire, "Semiconductor components for monolithic applications, "in *Integrated Optics*, T. Tamir, Ed. New York: Springer-Verlag, pp 243-304 (1985).

[21] H. Van Brug, F. H. Groen, Y. S. Oei, J. W. Pedersen, E. C. M. Pennings, D. K. Doeksen, and J. J. G. M. Van der Tol, " Low-loss straight and curved ridge waveguide in LPE-grown GaInAsP," *Electron. Lett.*, vol. 25, pp. 1330-1332 (1989).

[22] P. Buchmann, H. Kaufmann, H. Melchior, and G. Guekos, "Reactive ion etched GaAs optical waveguide modulators with low loss and high speed," *Electron. Lett*., vol. 20, pp. 295-296 (1984).

[23] R. J. Deri, E. Kapon, and L. M. Schiavone, "Scattering in low loss GaAs/AlGaAs rib waveguides," *Appl. Phys. Lett*., vol. 51, pp. 789-791 (1987).

[24] M. K. Hibbs-Brenner and C. T. Sullivan, "Low-loss AlGaAs optical rectangular waveguides at 830nm," *Appl. Phys. Lett.*, vol. 56, pp. 1529-1531 (1990).

[25] These narrow band gap "passive" layers do not undergo population inversion and thus should also exhibit very high band-to-band absorption losses at the lasing wavelength.

[26] R. Dingle and C. H. Henry, Quantum Effects in Heterostructure Lasers, US Patent No. 3982207, 21, September 1976.

[27] The DOS function describes how many quantum mechanical states (per unit volume and within a small differential energy range) are available for occupancy by electrons and holes.

[28] Y. Arakawa and A. Yariv,"Theory of gain, modulation response, and spectral linewidth in AlGaAs quantum well lasers," *IEEE J. Quantum Electron.*, vol. QE-21, pp. 1666-1674 (1985).

[29] Y. Arakawa and A. Yariv," Quantum well lasers-gain, spectra, dynamics," *IEEE J. Quantum Electron*., vol. QE-22, pp. 1887-1899 (1986).

[30] A. Sugimura, "Phonon assisted gain coefficient in AlGaAs quantum well lasers," *Appl. Phys. Lett*., vol.43, pp. 728-730 (1983).

[31] N. K. Dutta and R. J. Nelson,"The case for Auger recombination in $In_{1-x}Ga_xAs_yP_{1-y}$," *J. Appl. Phys.*, vol. 53, pp.74-92 (1982).

[32] N. K. Dutta, " Calculations of Auger rates in a quantum wells and its application to InGaAsP quantum well lasers," *J. Appl. Phys.*, vol. 54, pp. 1236-1245 (1983).

[33] See *Quantum Well Lasers,* P. S. Zory, Jr., Ed., Academic Press (1993), for an excellent review of these developments.

[34] Y. Arakawa and H. Sakaki, " Multidimentinal quantum well laser and temperature dependence of its threshold current, " *Appl. Phys. Lett.*, vol. 40, p 939 (1982).

[35] R. E. Collin, "Theory of Guided Waves," p. 470. McGraw-Hill, New York (1960).

[36] http://www.ioffe.rssi.ru/SVA/NSM/Semicond/index.html.

[37] H. C. Casey and M. B. Panish in *Hetrostructure Laser. Part A: Fundamental Principles.* (1978).

[38] R. M. Knox and P. P. Toulios, "Integrated circuits for the millimeter through optical frequency range," in *Proc. MRI Symp. on Sub-millimeter Waves*, J. Fox, Ed., Brooklyn, NY, Polytechnic Press (1970).

[39] W. Streifer, R. D. Burnham, and D. R. Scifres,"Analysis of diode lasers with lateral spatial variations in thickness," *Appl. Phys. Lett.*, vol. 37, pp. 121-123 (1980).

[40] J. Buus, "The Effective Index Method and Its Application to Semiconductor Lasers," *IEEE J. Quantum. Electron.*, vol. 18, pp. 1083-1089 (1982).

[41] Rachel Symes, Robert M. Sayer and Jonathan P. Reid, "Cavity enhanced droplet spectroscopy: Principles and prospects," *Phys. Chem.,* vol.6, pp. 474-487 (2004).

[42] G. P. Agrawal and N. K. Dutta, *Semiconductor Lasers*, 2nd Edition, Chapter 6, Van Nostrand Reinhold, New York (1993).

[43] N. C. Frateschi and A. F. J. Levi," Resonant modes and laser spectrum of microdisk lasers," *Appl. Phys. Lett.*,vol. 66, pp. 2932-2934 (1995).

[44] N. C. Frateschi and A. F. J. Levi, "The spectrum of microdisk lasers," *J. Appl. Phys.,*vol. 80, pp. 644-653 (1996).

[45] N. B. Rex, “Regular and Chaotic Orbit Gallium Nitride Micro-Cavity Lasers,” Ph.D. thesis, Yale University (2001).

3. MATERIAL STRUCTURE AND DEVICE PROCESSING

3.1. Description of Material Structures

In this section, we describe the AlGaAs/GaAs QW material structures used to perform any and all experiments associated with this research project. The samples were prepared by Dr. Steve Smith at Amoco Laser Company via metal organic chemical vapor deposition (MOCVD). The layer structure was grown on an n-type (100) oriented epi-ready GaAs substrate beginning with a 500 nm n-type GaAs buffer layer followed by 1.25 µm n-type $Al_{0.85}Ga_{0.15}As$ lower confining layer, a 1.25 µm p-type $Al_{0.85}Ga_{0.15}As$ upper confining layer, and finally, a 150 nm p-type GaAs ohmic contact layer. The active region consists of a single GaAs undoped quantum well placed in the centre of a waveguide. The upper and lower half of the waveguide consists of undoped $Al_{0.25}Ga_{0.75}As$ semiconductor material. The thickness of the quantum well is 10 nm and the thickness of the upper and lower waveguide regions is 125 nm respectively. A summary of all relevant design parameters is presented in Table 3.1.

Table 3.1: Material design parameters for the AlGaAs/GaAs QW laser structure.

Layer Description	Nominal Thickness	Semiconductor Material	Alloy Mole Fraction	Doping Concentration (cm^{-3})	Doping Species
Ohmic Contact Layer	150 nm	GaAs	x = 0	$p^{+} = 2x10^{19}$	Mg
Upper Confining Layer	1.25 µm	$Al_xGa_{1-x}As$	x = 0.85	$p = 5x10^{17}$	Mg
Upper Half of Waveguide	125 nm	$Al_xGa_{1-x}As$	x = 0.25	undoped	N/A
Quantum Well	10 nm	GaAs	x = 0	undoped	N/A
Lower Half of Waveguide	125 nm	$Al_xGa_{1-x}As$	x = 0.25	undoped	N/A
Lower Confining Layer	1.25 µm	$Al_xGa_{1-x}As$	x = 0.85	$n = 5x10^{17}$	Se
Buffer Layer	500 nm	$Al_xGa_{1-x}As$	x = 0.25	$n^{+} = 2x10^{18}$	Se
Substrate	325 µm	GaAs	x = 0	$n^{+}= 2x10^{18}$	Si

The layer thicknesses listed in Table 3.1 were confirmed via scanning electron microscopy (SEM). A schematic cross-section of the layer structure, along with the corresponding SEM image, is shown in Fig. 3.1. There is good overall agreement between the MOCVD design parameters and the measured layer thicknesses.

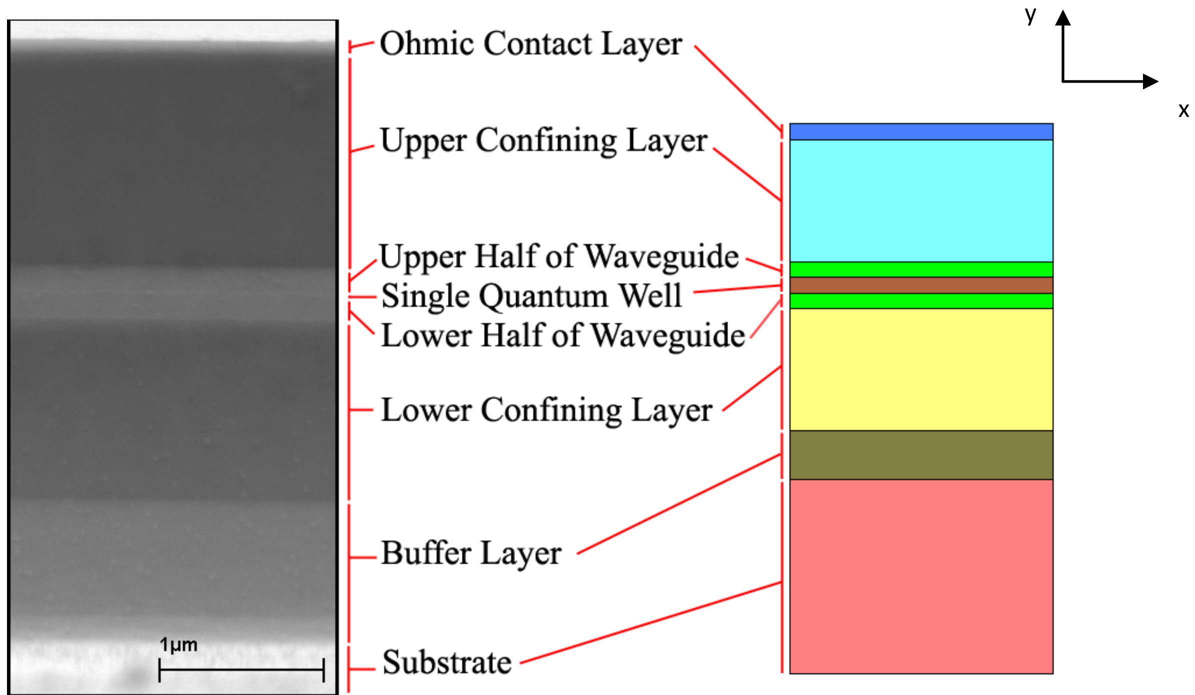

Figure 3.1: Schematic cross-section of AlGaAs/GaAs QW laser structure (right hand side) and corresponding SEM image (left hand side). The SEM image was taken (after cleaving and staining the sample) using the LEO 1550 instrument at Virginia Tech.

The alloy mole fractions and doping concentrations listed in Table 3.1 were verified using Secondary Ion Mass spectrometry (SIMS). This technique is based on sputtering the surface of the specimen with a focused primary ion beam and collecting and analyzing ejected secondary ions. These secondary ions are measured with a mass spectrometer to determine the elemental or molecular composition of the surface. SIMS is a powerful analytical tool for studying concentration vs. depth profiles of doping atoms, owing to its extremely high sensitivity and depth resolution. Figure 3.2 shows SIMS depth profiles for the relevant alloy constituents and

doping species. There is good agreement between the MOCVD design parameters and the measured alloy mole fractions and doping concentrations.

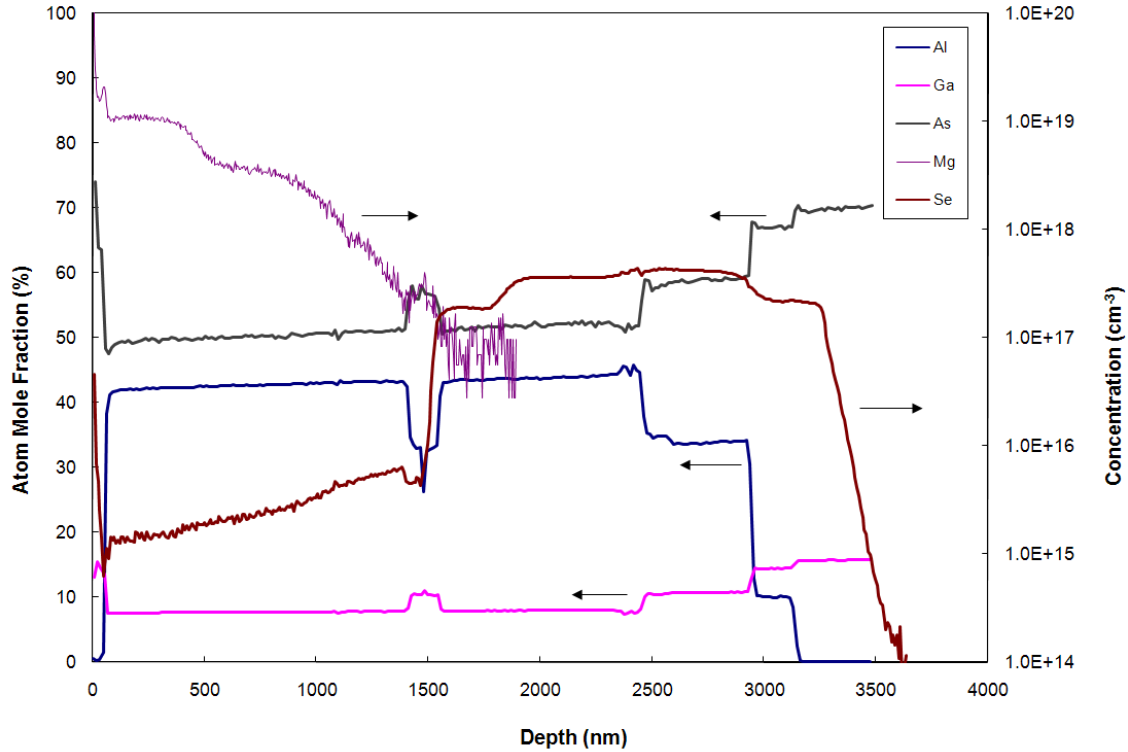

Figure 3.2: SIMS depth profiles of the alloy constituents (Al, Ga, As) and the doping species (Mg, Se) in the AlGaAs/GaAs QW laser structure. These measurements were made using the Cameca IMS 7f GEO instrument at Virginia Tech.

Several different AlGaAs/GaAs QW structures were employed throughout this body of work; however, all of these samples were synthesized in the same MOCVD reactor using nearly identical growth recipes. As a consequence, we expect that the layer structure and materials parameters described above are representative of the entire collection of samples.

3.2. Overview of Device Processing

In this section, we present a brief overview of the process flow used to make oxide-confined (*OXC*) whispering gallery mode lasers. This device embodiment serves as a useful reference since it has been employed by many other research groups in previous work on WGM lasers. In

addition, we will gauge the utility of the new hydrogenation-based fabrication process (described in Chapter 5) by direct comparison against our own *OXC* lasers.

Several unit processes, such as photolithography, etching, metal deposition, and thermal annealing, are executed in series to realize the final device structure. These unit processes are carried out using a number of sophisticated tools, such as a Karl Suss MA-6 mask aligner, Trion Technologies inductively-coupled plasma etcher (ICPE), Kurt Lesker electron-beam vapor deposition (E-beam) system, and Trion plasma-enhanced chemical vapor deposition (PECVD) system. These tools are part of the newly renovated cleanroom micro-fabrication facility at Virginia Tech.

A schematic cross-section of the oxide-confined WGM laser structure is shown in Fig. 3.3. Note the PECVD (SiO_x) *oxide* layer inserted between the p-pad metal contact and the p-type AlGaAs upper confining layer. This electrical insulator prevents current from flowing directly from the metal pad into the central region of the device and thereby increases the current density at the periphery of the laser cavity (in close proximity to the peak intensity of the WGMs).

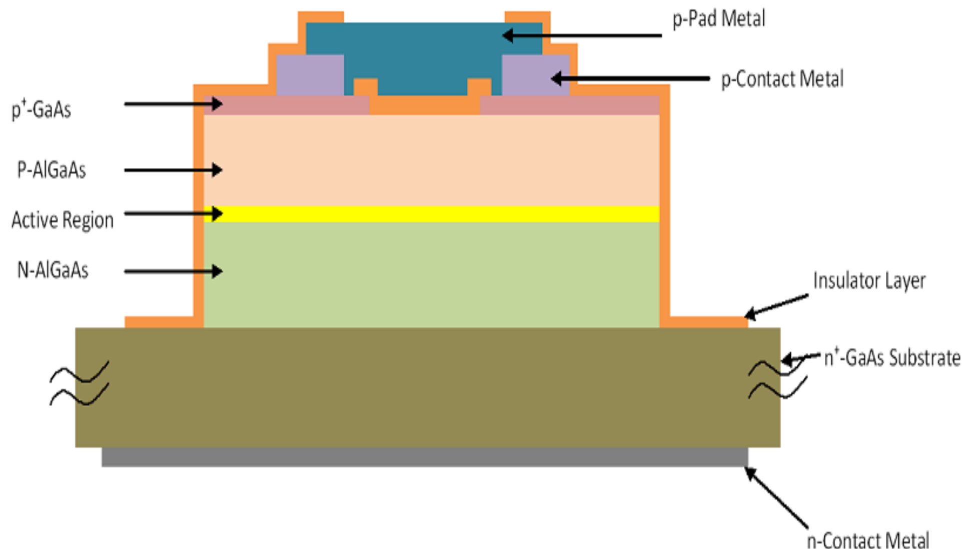

Figure 3.3: Cross-section of the WGM laser structure with oxide as the current blocking region.

The O-C laser fabrication procedure involves the following steps:

(i) Selective removal of the p^+-GaAs cap layer by wet etching, followed by oxide deposition and patterning to form the current blocking layer.

(ii) Formation of p-side ohmic contact (Ti 300 Å / Au 2000 Å) with ring geometry, followed by thermal annealing at 400 °C for 5 min in forming gas (3.99% H_2 mixed with Ar). Forming gas is used to prevent the metal contacts from oxidizing during the annealing process.

(iii) Formation of p-side metal pad (Ti 300 Å / Au 2000 Å) on top of the ohmic p-metal ring. This metal pad acts as a relatively large, smooth noble metal surface for probe testing and wire bonding.

(iv) Creation of WGM cavity by dry etching down through the entire epitaxial layer structure. The ICPE etching step uses Cl_2 and BCl_3 process gases.

(v) Deposition of nitride encapsulation layer to passivate electronic surface states and reduce "optical roughness" of WGM cavity.

(vi) Formation of broad-area ohmic contact to back-side of n-type substrate (Sn 200 Å/Au 1100 Å), followed by thermal annealing at 390 °C or 3 min.

Further details on sample handling and device fabrication (including specific recipes for all critical steps) are presented in Appendix B and C, respectively.

3.3. Design of μ-Pillar Optical Cavities

In this section, we describe three different optical cavity structures that were designed to assess the performance of our WGM lasers. The first structure, which has pure circular symmetry, is referred to herein as a full-circle *(FC)* cavity. Figure 3.4 shows a plan-view drawing of such an optical cavity, with labels assigned to key design parameters. In reality, our AlGaAs-GaAs *FC* cavities are only 3.5 μm in height (along the z-axis of the cylindrical coordinate system) and bounded on the bottom-side by a GaAs substrate. Therefore, when considering all three

dimensions, our *FC* cavities are identical to the micro-pillar devices investigated by several other groups [1-4]. We refer to these devices herein as *μ-Pillar* structures.

This dielectric structure closely resembles an infinite cylindrical cavity, which is the mathematical construct most often used to determine the EM mode spectrum in WGM lasers [5-7]. Such an approximate EM analysis is sufficient to formulate a qualitative understanding of WGMs, which can then be used to investigate the impact of design parameters (cavity radius, width of gain region, offset of gain region from cavity perimeter), and process limitations (non-vertical profile and surface roughness of cavity sidewall), on the operating characteristics of WGM lasers.

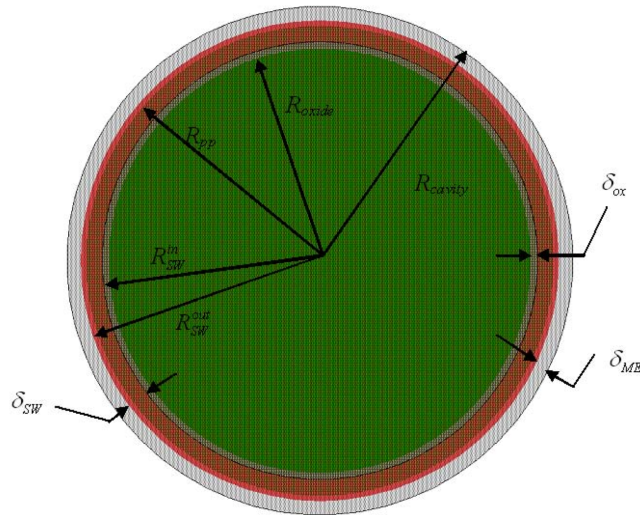

Figure 3.4: Plan-view drawing of full-circle *(FC)* optical cavity.

R_{cavity}: radius of etched cavity.

R_{pp}: radius of p-pad metal.

R^{out}_{sw}: outer radius of p-contact metal ring.

R^{in}_{sw}: inner radius of p-contact metal ring.

R_{ox}: radius of the oxide current blocking region.

δ_{ME}: separation between p-metal ring and cavity sidewall.

δ_{ox}: separation between p-metal ring and oxide layer.

δ_{SW}: width of the p-contact metal ring.

It may prove useful, for diagnostic purposes, to vary the optical path length in such circular dielectric structures without changing the cavity radius. We achieve this objective by means of the partial-circle *(PC)* optical cavities shown in Fig. 3.5. Considering that electronic gain is restricted to the cavity periphery (see p-contact ring highlighted in red), we do not expect lasing to occur in multiple bounce optical modes with small angles of incidence. Instead, we anticipate lasing in whispering-gallery-like modes with feedback from the flat facets. The stimulated emission from these *PC* cavities could then be sampled at one (or both) of the output facets akin to the situation in Fabry-Perot lasers.

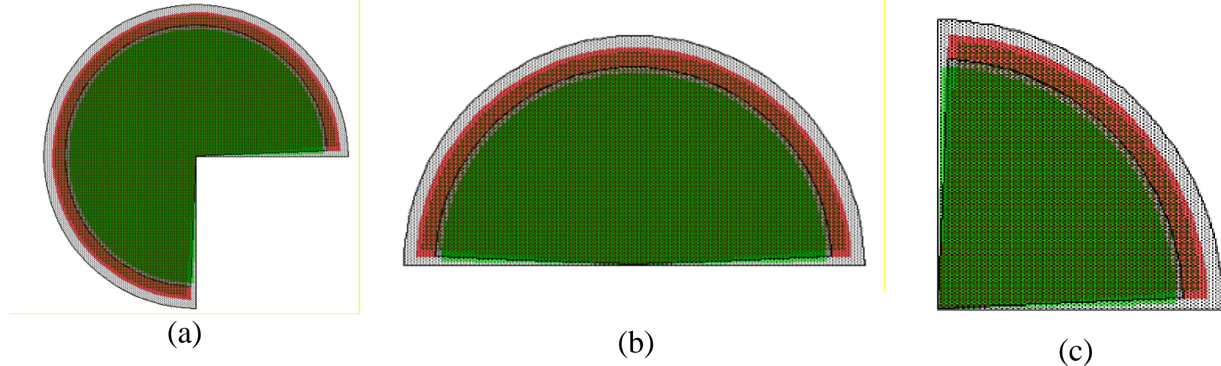

Figure 3.5: Plan-view drawing of partial-circle *(PC)* optical cavities: (a) ¾-circle, (b) ½-circle, and (c) ¼-circle dielectric structure.

In principle, photons that occupy WGMs should circulate around the curved inner boundary of the cavity, reflecting from the walls with an angle of incidence greater than the critical angle for total internal reflection. These photons remain trapped inside the cavity with only minute losses of light caused by evanescent leakage and scattering from surface roughness. Moreover, the small fraction of photons that do escape would be emitted into the vacuum with equal probability at all angles (i.e., the laser output would be non-directional). So, in order to make practical use of WGM lasers, it is necessary to destroy the pure circular symmetry of the *FC* cavity. We accomplish this goal by distorting the cavity shape from a circle to a spiral and thereby providing an output "notch" at a specific location along the cavity perimeter.

This final dielectric structure, which is referred to herein as a spiral *(Sp)* cavity, is shown in plan-view in Fig. 3.6. Along the z-axis (out of the page) this structure is identical to the *FC* and *PC* cavities, and the color scheme follows that used above. The perimeter of the *Sp* cavity is defined by $r(\phi) = r_o(1 + \frac{\varepsilon \cdot \phi}{2\pi})$, where ε is the deformation parameter and r_o is the radius at $\phi = 0$. As a consequence, a discontinuity (or notch) appears at $\phi = 2\pi$ which provides a means for out-coupling of photons.

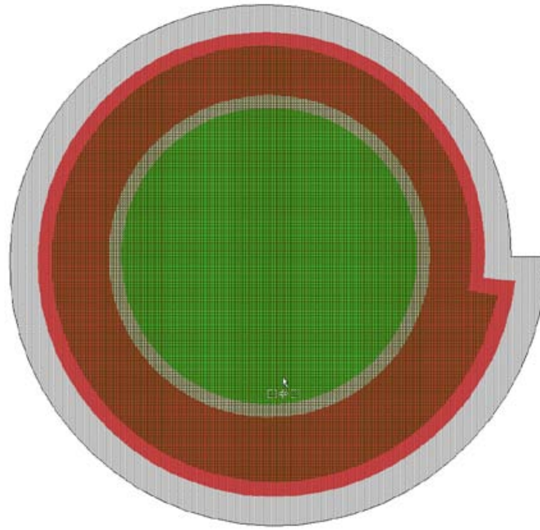

Figure 3.6: Plan-view drawing of spiral *(Sp)* optical cavity.

Additional information regarding the design parameters used to make WGM lasers from all three types of dielectric structures is presented in Chapter 6.

3.4. Layout of μ-Pillar Photomask

In order to execute the process flow described in Section 3.2, a photo-mask was designed with six different regions on a 4 inch glass plate. A low magnification optical image of this photo-mask is shown in Fig. 3.7. The dark field (DF) regions, highlighted in blue, are used to create openings in photoresist for the following purposes: (1) p-metal ring deposition via lift-off, (2) p-

metal pad deposition via lift-off, and (3) oxide removal for exposure to hydrogen passivation. The light field (LF) regions, highlighted in white, are used to leave photoresist features that serve as masks for the following procedures: (1) dry etching of the optical cavity, (2) patterning of the oxide for blocking current, and (3) deposition of n-metal top contact via lift-off. The later process step can be used, as an alternative to the broad-area back-side n-metal contact, for processing laser structures grown on semi-insulating substrates.

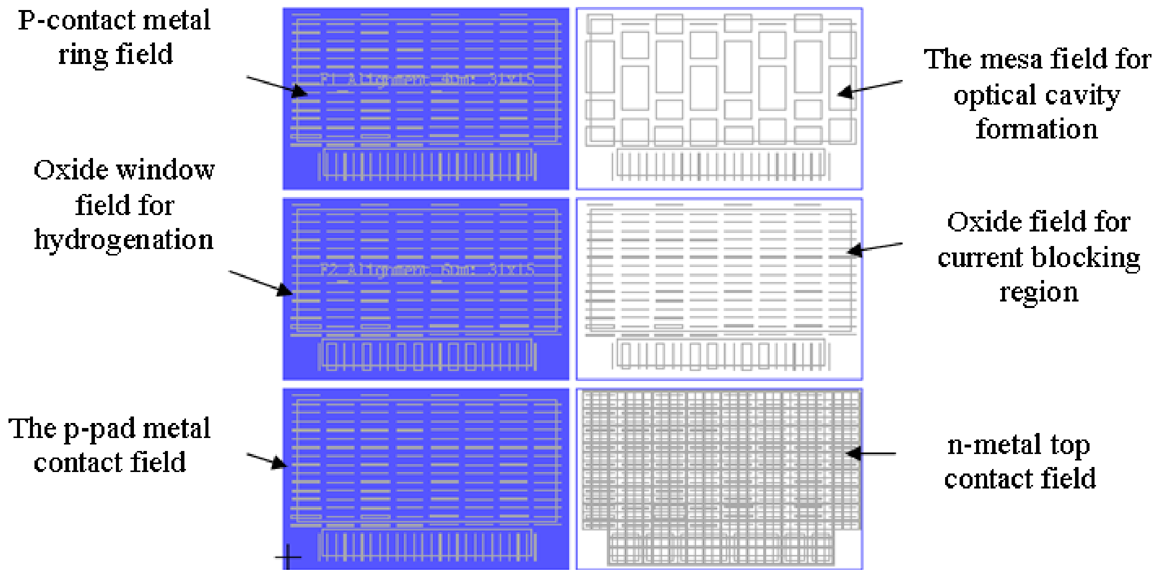

Figure 3.7: Optical image of WGM laser mask designed at Virginia Tech using L-edit software from Tanner Research. The photo-mask was manufactured by Image Technology using advanced optical lithography techniques.

In each region of the photo-mask there are 31 distinct *FC* cavity structures, each with different design parameters. Every design is repeated 4x giving a total of 124 *FC* laser diodes. The same design philosophy was followed for the *PC* structures – 31 sets of parameters were repeated 4x yielding 124 devices for each fractional cavity (total of 372 *PC* laser diodes). With regard to *Sp* laser diodes, there are 4 devices with radius=9 μm, 6 devices with radius=11 μm, and 3 devices with radius=18 μm. Each of these 13 devices is repeated 4x with two different deformation parameters (ε=0.15, and ε=0.05) to give a total of 104 devices. All spiral lasers have an out-coupling angle of 90 degrees. The center-to-center distance between devices is 500 μm over the entire photo-mask.

References

[1] S. L. McCall, A. F. J. Levi, R. E. Slusher, S. J. Pearton, and R. A. Logan, "Whispering-gallery mode mirodisk lasers," *Appl. Phys. Lett.*, vol. 60, pp. 289-291 (1992).

[2] S. M. K. Thiyagarajan, D. A. Cohen, A. F. J. Levi, S. Ryu, R. Li, and P. D. Dapkus, "Continuous room-temperature operation of micro-disk laser diodes," *Electron. Lett.*, vol. 35, pp. 1252-1254 (1999).

[3] A. F. J. Levi, R. E. Slusher, S. L. McCall, T. Tanbun-Ek, D. L. Coblentz, and S. J. Pearton, "Room Temperature Operation of microdisc lasers with submilliamp threshold current," *Electron. Lett.,* vol. 28, pp. 1010-1011 (1992).

[4] R. E. Slusher, A. F. J. Levi, U. Mohideen, S. L. McCall, S. J. Pearton and R. A. Logan, "Threshold Characteristics of semiconductor microdisk lasers," *Appl. Phys. Lett.,* vol. 63, 1310-1312 (1993).

[5] M. K. Chin, D. Y. Chu, and S. T. Ho, "Estimation of spontaneous emission factor for microdisk lasers via the approximation of whispering gallery modes," *J. Appl. Phys.,* vol. 75, pp. 3302 (1994).

[6] G. P. Agrawal and N. K. Dutta, *Semiconductor Lasers*, 2nd Edition, Chapter 6, Van Nostrand Reinhold, New York (1993).

[7] R. P. Wang, M. Dumitrescu, "Theory of optical modes in semiconductor microdisk lasers," *J. App. Phys.,* vol. 81, pp. 3391 (1997).

4. MEASUREMENT TECHNIQUES AND DEVICE ANALYSIS

The performance of laser diodes under steady-state operation can be quantified by measuring current vs. voltage (I-V) curves, light power vs. current (L-I) curves, and radiated flux as a function of wavelength (optical spectra). In the first part of this Chapter, we describe experimental setups designed and built at Virginia Tech to measure these device "characteristics" and discuss the relevant calibration procedures. In the second part of this Chapter, we define key metrics for laser diode performance and show how to extract useful physical parameters from I-V, L-I, and spectral data.

4.1. Instrument Design and Calibration

An important reference condition for laser diode characterization is that of continuous-wave (CW), room-temperature (300 K) operation because many device applications would benefit from direct-current biasing without active cooling. However, at high drive currents, CW operation often leads to significant heat dissipation within the device which could manifest itself in several undesirable ways. For example, there may be a significant increase in junction temperature which would degrade the device characteristics, and thereby lead to erroneous reporting of "room-temperature" physical parameters. In addition, local heating at the metal/semiconductor interfaces may cause melting of the ohmic contacts, and dissolution of the semiconductor, which would give rise to permanent device failure. These problems can be mitigated, and perhaps even eliminated, by using a pulsed-wave (PW) current source to perform measurements.

4.1.1. Apparatus for I-V Measurements

The experimental setup for making I-V measurements under CW excitation is shown in Fig. 4.1. The Keithley 2400 source-measure unit (SMU) can deliver up to 1 A of current with a voltage compliance of 100 V. The lowest measurable current is 10 pA and the minimum detectable voltage is 1 μV. This SMU can be configured to source current (voltage) while simultaneously measuring voltage (current). Standard BNC cables transfer electrical signals between the Keithley 2400 and the device-under-test (DUT) without the need for special interface circuits.

For on-wafer testing, electrical signals are brought into contact with the DUT using precision micro-manipulator probes made by Creative Devices, Inc. The BNC cables are soldered directly to the external wire leads when measuring packaged devices. Each continuous-wave I-V data collection run is executed under computer control – via a specially designed LabVIEW program – by sourcing current in a stepwise manner over the desired range (from low to high values) while measuring the corresponding diode voltage.

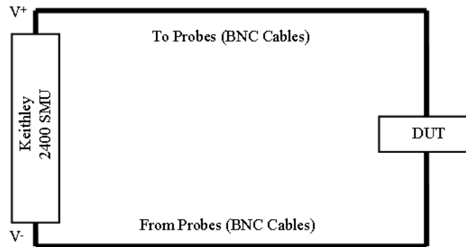

Figure 4.1: Apparatus for measuring I-V curves under CW excitation.

Since the Keithley 2400 was calibrated by the manufacturer we need only correct for the voltage drop across the BNC cables to obtain accurate I-V data. This "in-house" calibration can be done in one of two ways: (1) measure the BNC cable resistance under real operating conditions by performing an I-V sweep with the two current probes shorted together and then subtract the appropriate $V = I_d \times R_{cable}$ values from each measured voltage or (2) use the SMU in the four-point measurement mode and add two additional probes to the experimental setup to separate the current sourcing function from the voltage measurement operation.

The instrument configuration for recording I-V data under PW excitation is shown in Fig. 4.2. The Avtech 107-D current pulse generator is used to drive the DUT. One input channel of the Tektronix TDS-520 oscilloscope is connected at the "Measured V^+" and "Measured V^-" terminals to determine the voltage drop across the DUT. The second oscilloscope channel reads the voltage signal from the IST model 711 current probe located at the "Measured I" node in the circuit. The Avtech 107-D is capable of producing current pulses as short as 50 ns in duration (up to a maximum pulse width of 5 μs). The IST current probe has a conversion ratio of 1 mA / 1 mV with a maximum ampere-second product of 6 Amp-μsec. The oscilloscope is capable of

performing measurements up to 500 MHz which is more than adequate for our purposes. Each pulsed-wave I-V data collection run is performed via computer control using a modified version of the LabVIEW program mentioned above.

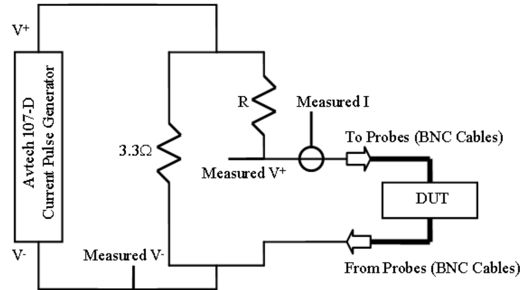

Figure 4.2: Apparatus for measuring I-V curves under PW excitation.

The Avtech 107-D was specified for other research in which we needed to deliver currents well above 1 A to a load with a voltage drop of several tens of volts. As such, when connected directly to the DUT without interface circuitry, this excitation source can deliver up to 20 A with a voltage compliance of 60 V. The downside of this robust design is that severe pulse shape distortion occurs when attempting to deliver current pulses below 700 mA. We addressed this problem by building a current divider circuit that consists of a 3.3 Ω shunt resistor connected in parallel across a series combination of the DUT with a user-defined resistor (*R*). With this simple modification, we can program the Avtech 107-D to deliver well-formed pulses in the 0.8 to 15 A range to the circuit while achieving up to a 10^4 fold reduction in actual bias current flowing to the DUT.

Since the accuracy of the CW measurement approach has been established we can use it to check the veracity of PW data collected in the manner described above. An example of such a comparison is presented in Fig. 4.3. The device under consideration was an index-guided multiple QW laser diode manufactured by NVG (model D650-5). The CW curve was recorded first by sweeping the current from a low value of 10 μA to an upper limit of 50 mA. The entire measurement process was completed in less than one minute. Since the voltage drop across the diode is roughly 2.3 V at 50 mA, a maximum electrical power of 115 mW is delivered to the

DUT for a very short time. Therefore, we do not expect significant heating related distortions of the CW data. The pulsed-wave data was collected in a piece-wise fashion, by inserting different values of *R* into the circuit, in order to cover the widest possible range of current. The agreement between CW and PW curves demonstrates the suitability of this pulsed-wave I-V measurement technique.

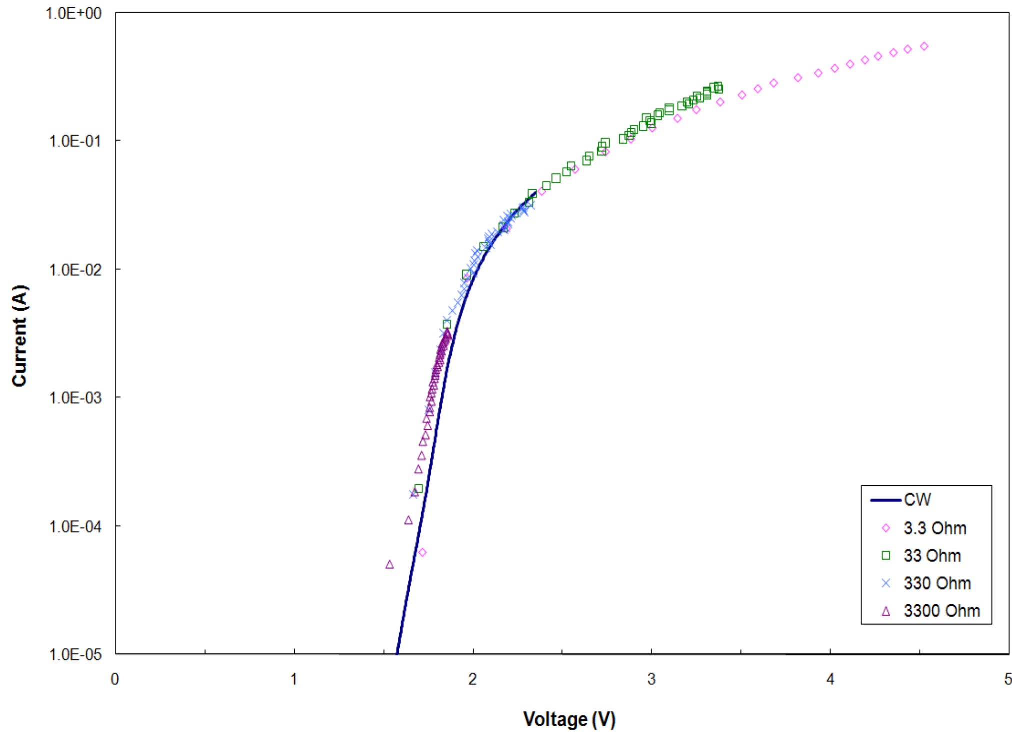

Figure 4.3: Comparison of I-V data acquired under both CW and PW conditions at 300 K. The DUT was a commercial laser diode (NVG D650-5). The resistance values shown in the legend correspond to *R* in the current divider circuit.

4.1.2. Apparatus for L-I Measurements

The discussion in this Section focuses on experimental methods for collecting and calibrating the light-power (L) component of laser diode L-I data sets acquired under both CW and PW conditions. The associated current (I) sourcing and sensing techniques were described in Section 4.1. All light power vs. current data was recorded under computer control using the in-house LabVIEW programs mentioned above.

The apparatus for performing L-I measurements under CW conditions is shown in Fig. 4.4. An optical lens is used to collect light emitted from the DUT and focus it onto the detector. The Newport 818-UV is a silicon photodiode, 1 cm^2 in area, with a spectral responsivity greater than 0.09 A/W over a wide wavelength range ($250 < \lambda < 1000$ nm). Its peak responsivity is $\mathcal{R}_{peak}$ = 0.4 A/W at 850 nm. In addition, the 818-UV detector gives a linear current (output) signal over an optical power (input) range from 10^{-12} to 10^{-4} W. *A calibration module connected to the Newport 2823-C meter converts the measured detector current into a reported value of optical power identical to that incident on the detector.* Optical density (OD) filters can be used with the detector to attenuate the input light power by up to 1000x and thereby extend the upper limit for a linear response to 100 mW.

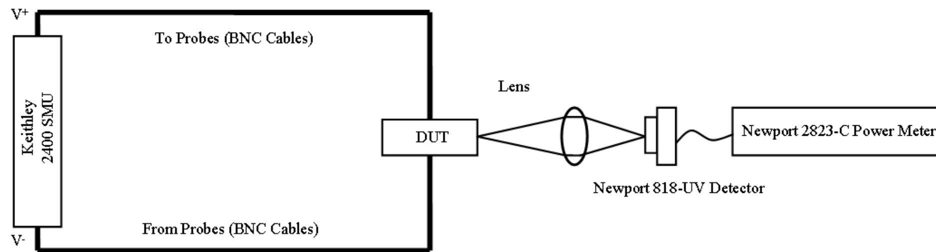

Figure 4.4: Apparatus for measuring L-I curves under CW excitation.

Since the Newport 818-UV / 2823-C combination was calibrated by the manufacturer we need only correct for the throughput of the optical system (T_{opt}) – which in this case is a simple quartz lens – to obtain accurate values of light power emitted by the DUT. In order to accomplish this task, we first purchased another optical element from Newport known as an integrating sphere (model 819-04). This four-inch diameter spherical cavity is constructed from a special thermoplastic material with an optical reflection coefficient greater than 99% from λ = 400 to 1600 nm. The cavity body has two access ports: one for inserting the DUT and the other for mounting the detector. Light emitted by the DUT is reflected many times off the inner cavity surface after which its spatial distribution is uniform and its polarization is random – *the integrating sphere presents a near ideal optical input to the detector.* The Newport 819-04 / 818-UV combination was recalibrated as one unit by the manufacturer.

The next step is to acquire two distinct L-I characteristics for the same laser diode: one using the quartz lens (QL) and the other using the integrating sphere (IS). These measurements should be performed over a current range (above threshold) were the device exhibits linear behavior. The integrating sphere collects 100% of the light emitted in the forward direction and the 819-04 / 818-UV / 2823-C combination reports absolute values of optical power. In contrast, the quartz lens collects only a fraction of the stimulated emission and it has non-zero optical transmission losses. If the two L-I curves can be made to overlap by multiplying the IS curve by a constant factor (which is less than unity) then this procedure establishes the value of T_{opt} for the quartz lens. This calibration must be done only once for a specific type of laser diode. All future QL curves from similar devices can be calibrated using T_{opt} to correct the light power (L) values in the recorded data sets.

If, however, other laser structures become of interest – *with different emission wavelengths and/or far-field emission patterns* – then the calibration procedure would have to be repeated for each new device type. Of particular concern to us are small (sub 100 μm) laser structures monolithically integrated onto much larger semiconductor chips ($\approx 1\ cm^2$). In this case, the entire chip would have to be mounted on a rigid package with wire bonds connecting the external leads to bond-pads on its surface and metal traces connecting the bond pads to individual devices. While this process is more cumbersome it is certainly doable using the existing packaging facilities at Virginia Tech.

Many of the physical processes that influence laser diode performance exhibit strong temperature dependencies. Therefore, in addition to the CW measurement capability described above, it is important that we are able to record accurate L-I data under pulsed-wave operation *were device heating can be kept to a minimum.* The instrument configuration for performing such measurements is shown in Fig. 4.5. Note that "photon collection" is accomplished via the same quartz lens arrangement employed in the CW setup. It was necessary, however, to address two new issues owing to the PW biasing conditions. First, because the optical signal from the DUT closely follows the drive current, the large-area CW detector no longer responds fast enough to a

yield well defined output current pulse. This problem was resolved by replacing the CW detector with an alternative model specially designed for PW operation.

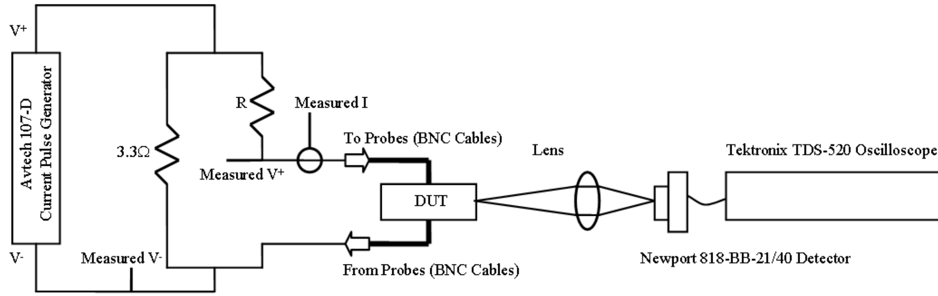

Figure 4.5: Apparatus for measuring L-I curves under PW excitation.

The two silicon photodiode options available from Newport (818-BB-21/818-BB-40) differ significantly in junction area (A_{21}= 0.12 mm^2 / A_{40}= 20 mm^2) and thus junction capacitance (C_{21}= 1.5 pF / C_{40}= 45 pF). So, there is a clear trade-off between the output current rise/fall times (τ_{21}= 0.3 ns / τ_{40}= 30 ns) and the input acceptance angles (θ_{21}= 10° / θ_{40}= 41°). A signal current rise/fall time of 30 ns is adequate for our present work, so we chose the 818-BB-40 unit for its larger optical acceptance angle.

The data acquisition procedure is best understood by referring to the pair of oscilloscope traces shown in Fig. 4.6. These particular waveforms correspond to a single bias point from an entire L-I measurement run. The pulse labeled "current waveform" comes from the IST 711 current probe and as such it represents the bias current flowing through the DUT. The drive current was supplied by the Avtech 107-D current pulse generator and delivered to the DUT via standard BNC cabling connected to a pair of precision micro-manipulator probes. This current pulse sourcing configuration is responsible for the ringing observed in the waveform. The pulse labeled "detector waveform" comes from the 818-BB-40 photodiode. The detector module contains a 50 Ω output resistor through which the signal current flows. The Tektronix TDS-520 oscilloscope was used to measure the corresponding detector output voltage. Impedance matching to the input channel of the oscilloscope was achieved using a 50 Ω termination. The ringing in the detector voltage is not surprising since the light output from the DUT should

follow the ringing in the drive current pulse. The LabVIEW program calculates average values of drive current and detector voltage using the highlighted regions in the later part of both waveforms.

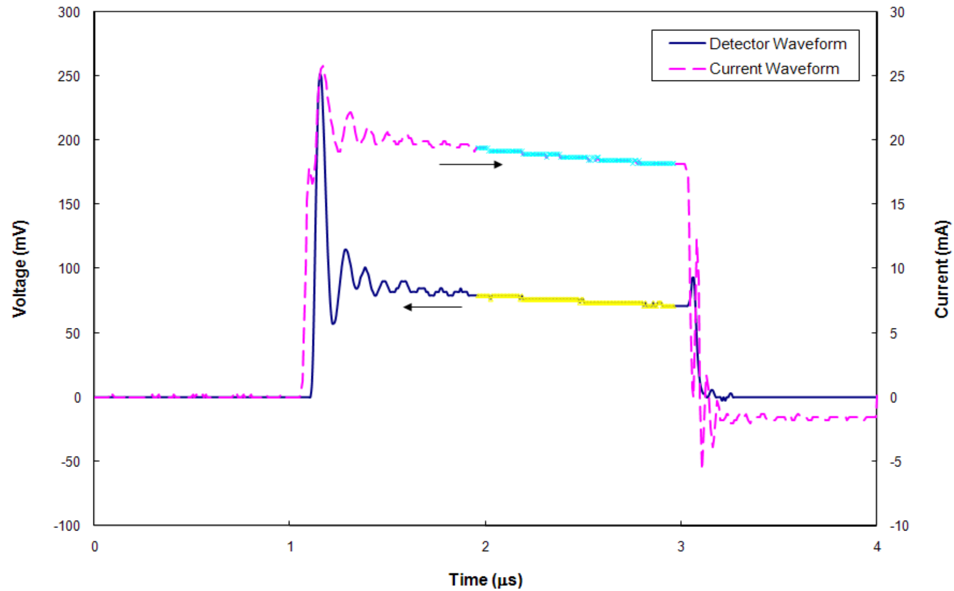

Figure 4.6: Input (current) and output (detector) waveforms from a typical pulsed-wave L-I measurement run. The current source pulses were 2 µs in duration with a repetition frequency of 200 Hz. The pulses delivered to the resistor network were swept from 0.8 to 3.2 A which corresponds to bias currents ranging from 8 to 32 mA. The DUT was a NVG D650-5 laser diode.

The second problem associated with the PW biasing and detection scheme is that the detector (output) voltage must be converted into an accurate value of optical (output) power. We utilize the calibrated CW measurement described above to accomplish this task via the following steps:

1) Perform a calibrated CW measurement over a range of bias current that is low enough to minimize device heating.

2) Perform a PW measurement over the same bias current range using the identical optical collection scheme.

3) Multiply the PW detector voltage by a correction factor to match the CW light power. This correction factor should remain the same from run-to-run provided the amount of light collected remains constant.

This correction procedure is illustrated here using a packaged laser diode (NVG D650-5) – *but it applies equally well to any device configuration that can be tested via the calibrated CW setup.*

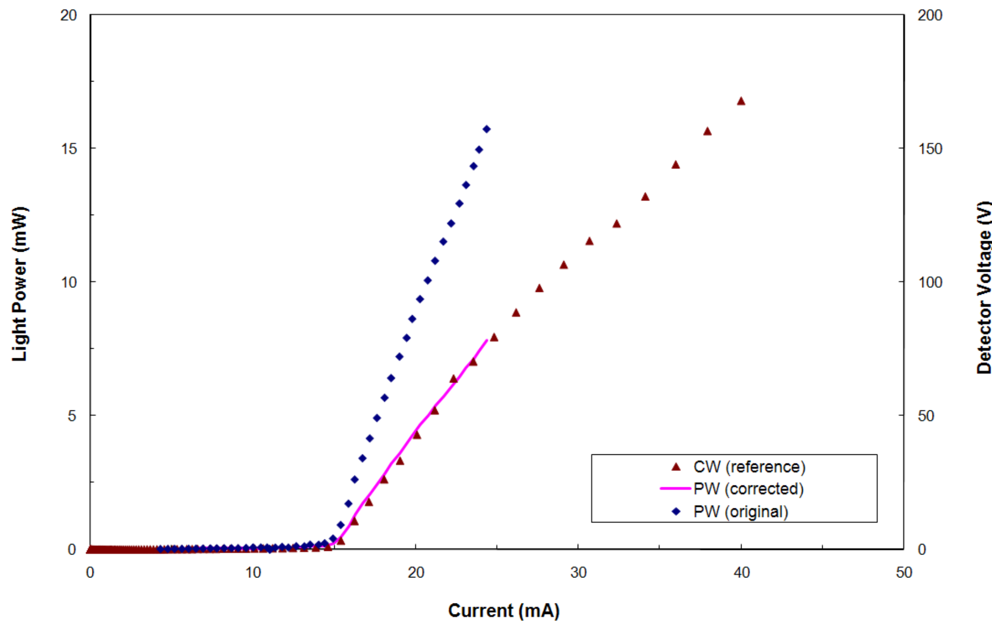

Figure 4.7: L-I data recorded under both CW and PW conditions at 300 K. The DUT was a NVG D650-5 laser diode. The reference CW data were plotted using the *Y-axis* labeled "light power" on the left hand side. The original PW data were plotted against "detector voltage" (right hand side). The solid line represents the corrected PW curve with its *Y-axis* values in mW.

The aggregate L-I data plotted in Figure 4.7 consists of *reference* CW data, its *original* PW counterpart, and the *corrected* PW curve. The corrected PW curve follows the reference CW data up to about 25 mA were device heating causes the L-I characteristic to become sub-linear. Note that the CW optical power is about 5 mW at a bias current of 20 mA in agreement with the NVG D650-5 data sheet – *this observation validates the initial calibration of the CW reference curve.*

4.1.3. Apparatus for Spectral Measurements

The instrument configuration for recording emission spectra under CW drive conditions is illustrated in Fig. 4.8. The same apparatus can be used to make PW spectral measurements by replacing the Keithley 2400 SMU with the Avtech 107-D pulsed current source and its associated interface circuitry. Light from the DUT is focused onto the entrance slit of a Roper Scientific spectrometer (SP-308). The diffraction grating inside the spectrometer disperses the light intensity over a range of angles in accordance with its spectral content. This angular intensity distribution is then focused onto the focal plane of a Princeton Instruments CCD array (PI-MAX 1024RB) which is mounted at the exit port of the spectrometer.

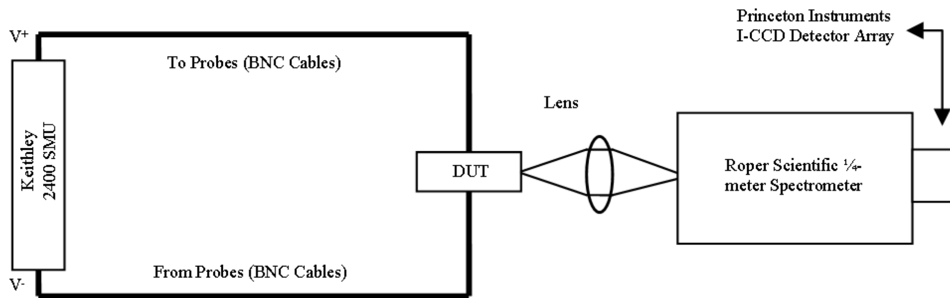

Figure 4.8: Apparatus for measuring optical spectra under CW excitation.

Each column of the CCD array receives the light intensity (I_c) emitted at a particular center wavelength (λ_c) over a predetermined wavelength range ($\Delta\lambda$). The CCD array has 1024 columns (each with an index number N) and thus the same number of distinct intensity $I_c(N)$ vs. $\lambda_c(N)$ data sets. These N = 1024 data sets are recorded and stored simultaneously by the CCD and thus represent one “wavelength slice” in the emission spectrum. The diffraction grating is then rotated using a precision stepper to capture another wavelength slice. The entire measurement process is executed under computer control using proprietary software from Roper Scientific.

Calibration of the wavelength axis is accomplished using a special Hg discharge lamp with a series of well defined optical transition energies. Calibration of the intensity component of the spectral distribution is considerably more difficult. The optical throughput of the apparatus (lenses, diffraction grating, turning mirrors, etc.) must be measured, over the entire wavelength

range of interest, and then all recorded intensity vs. wavelength data must be corrected for spectral distortions. This procedure was not necessary for our present work, so the intensity (vertical) scale is given in arbitrary units for any spectra presented herein.

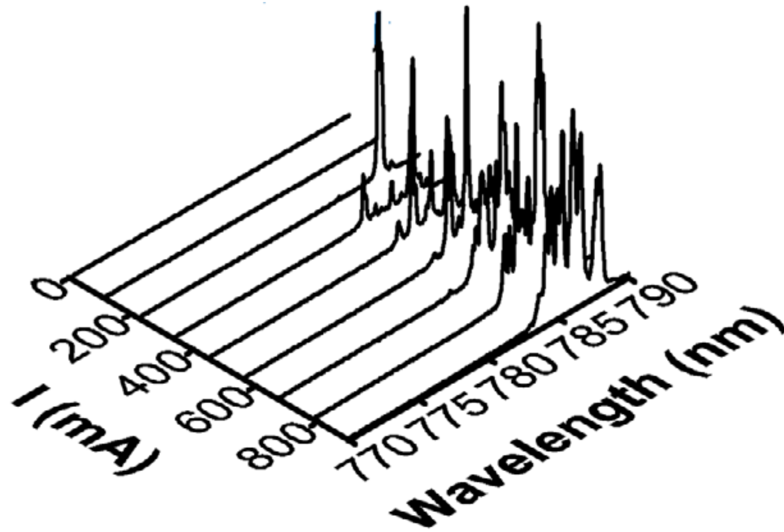

Figure 4.9: Spectral radiant flux measurements under PW excitation at 300 K. The DUT is an oxide-confined AlGaAs/GaAs QW spiral laser fabricated at Virginia Tech. The nominal radius of the spiral cavity is 250 µm and the width of the p-metal contact ring is 25 µm. The laser material used to fabricate this device is identical to that described in Chapter 3 of this manuscript.

A plot of radiant flux vs. wavelength is shown in Fig. 4.9 for an oxide-confined AlGaAs/GaAs QW spiral laser fabricated at Virginia Tech [1]. The measurements were performed in pulsed current mode to minimize the average power dissipated in the device. The pulse magnitude was varied from 0 to 1 A in increments of 10 mA (1 µs pulse width at 200 Hz repetition) and a complete spectrum was recorded at each bias current. The 3-D rendering is a convenient way to present data from several measurement runs. Only nine spectra are shown here, for visual clarity, with select bias currents below (two flat lines), just above (one curve at I≈ 220 mA), and well beyond (six traces with multiple peaks) threshold. The device reaches threshold at 190 mA with a peak emission wavelength of 787 nm. Additional (higher-order) modes appear as the laser is driven well above threshold.

4.2. Performance Metrics for Diode Lasers

When designing a semiconductor laser, the specific application determines the desired output wavelength, λ, and optical power, P_{opt}. In order to emit light near a given wavelength, an active region material is chosen based on its band-gap energy, $E_g \approx h\nu$ where h is Planck's constant and $\nu = c/\lambda$ (c is the speed of light and λ is the emission wavelength). The optical power emitted by a laser diode is described by Eq. 4.1, where η_i is the current injection efficiency, α_m the mirror loss, $\langle\alpha_i\rangle$ the internal modal loss, I the bias current, I_{th} the threshold current, and q the electron charge [2]

$$P_{opt} = \eta_i\left(\frac{\alpha_m}{\alpha_m + \langle\alpha_i\rangle}\right)\left(\frac{h\nu}{q}\right)(I - I_{th}) \qquad (4.1)$$

There are three ways to reduce the bias current necessary to produce the target value of P_{opt} – increase η_i, ensure that $\langle\alpha_i\rangle << \alpha_m$, and/or decrease I_{th}. The parameter η_i represents the fraction of bias current that gives rise to electrons and holes inside the gain region. Therefore, it should be possible to achieve $\eta_i = 1$ by eliminating all *leakage* current pathways. More details are given in Chapter 6 within the context of WGM laser performance.

The internal modal loss consists of free carrier absorption in the active layer (α_{fc}^a), and the adjacent cladding layers (α_{fc}^c), optical scattering from roughness at the cladding/core interfaces (α_{sc}), and coupling of the transverse optical mode into parasitic waveguides above and/or below the cladding layers (α_{cp}). Equation 4.2 summarizes all of these contributions to $\langle\alpha_i\rangle$

$$\langle\alpha_i\rangle = \Gamma\alpha_{fc}^a + (1-\Gamma)\alpha_{fc}^c + \alpha_{sc} + \alpha_{cp} \qquad (4.2)$$

The brackets refer to a weighting procedure that accounts for the optical losses in each layer of the laser structure. The Γ term is known as the *optical confinement factor* and it represents the

spatial overlap between the optical mode volume and the physical volume of the active region (see Appendix D). The free carrier losses should be minimized without significantly degrading electrical performance. This task can be accomplished by not introducing any intentional doping impurities into the waveguide, or the active region, and keeping the doping levels as low as possible in the upper and lower cladding layers. In conventional SCH-QW lasers, the scattering loss should be negligible owing to the superior quality of the grown interfaces between the waveguide and cladding layers. The transverse mode coupling loss should also be of no concern in well designed laser structures with adequately thick cladding layers. Once again, there is a trade-off as thick, lightly doped wide band-gap cladding layers could increase R_s significantly. The mirror loss α_m can be tailored by adjusting the cavity length and the average mirror reflectivity in the manner shown below

$$\alpha_m = \frac{1}{L_c} \ln\left(\frac{1}{R}\right) \tag{4.3}$$

We can relate optical losses to I_{th} by evoking a proper relationship between optical gain (G) and injection current density (J). Theoretical analysis suggests that G is a logarithmic function of J whenever the population of QW energy levels above the ground state is negligible [3]. Experimental validation of this hypothesis gave rise to the following expression for optical gain in QW lasers [4], where G_o and J_o are material-dependent constants.

$$\frac{G}{G_o} = 1 + \ln\left(\frac{\eta_i J}{J_o}\right) \tag{4.4}$$

At threshold the modal gain, ΓG, almost exactly balances the sum of α_m and $\langle \alpha_i \rangle$, so we have the following equality

$$\Gamma G_{th} = \left(\langle \alpha_i \rangle + \alpha_m\right) \tag{4.5}$$

Combining Eq. 4.4 and 4.5, and making the assumption that $J_{th} = \frac{I_{th}}{W_s L_c}$, where W_s is the width of the active region and L_c is the length of the cavity, we obtain an expression for I_{th} in terms of key materials and device parameters

$$I_{th} = W_s L_c \frac{J_o}{\eta_i} \exp\left(\frac{\langle \alpha_i \rangle + \alpha_m}{\Gamma G_o} - 1 \right) + I_{leak} \qquad (4.6)$$

The term I_{leak} accounts for lateral current flow beyond the lithographic stripe width where the optical field intensity is minimal. Equation 4.6 reveals that I_{th} can be reduced by increasing the injection efficiency and decreasing both the internal modal loss and the mirror loss. Note, also, that I_{th} scales downward in proportion to active region width providing that Γ_{lateral} does not deviate from unity and that I_{leak} does not increase as a consequence of the *narrow-stripe* laser fabrication process.

In order to reduce the engineering costs of dissipating waste heat, we must be able to reach the target value of P_{opt} at the lowest possible electrical power, P_{elec}. This means maximizing the wall-plug efficiency, η_{wp}, as defined by Eq. 4.7. The electrical power delivered to the laser diode is given by VI which is the product of applied voltage and bias current.

$$\eta_{wp} = \frac{P_{opt}}{P_{elec}} = \frac{P_{opt}}{VI} \qquad (4.7)$$

The applied voltage must be large enough to overcome the three electrostatic potential barriers specified by Eq. 4.8, where V_j is the voltage drop cross the depletion region of the p-n junction and R_s represents the series resistance of the p-type and n-type quasi-neutral regions. The parameter $V_{parasitic}$ signifies the presence of additional voltage drops across isotype semiconductor heterojunctions and/or semiconductor/metal interfaces.

$$V = V_j + IR_s + V_{parasitic} \qquad (4.8)$$

Any parasitic voltage drops must be negligible and the resistivity • thickness products for the quasi-neutral regions must be made as small as possible (without sacrificing optical performance) to realize acceptable values of wall-plug efficiency. These goals can only be attained by careful optimization of both the crystal growth and device fabrication processes.

4.3. Parameter Extraction for Diode Lasers

4.3.1. Analysis of I-V Characteristics

From a practical viewpoint there are two important reasons to test the electrical performance of p-n junction laser diodes: (1) establish the quality of the sample before subjecting it to further analysis and (2) determine the electrical power that is necessary for laser operation. The pair of I-V curves shown in Fig. 4.10 is representative of good quality devices. The DUT is an oxide-confined AlGaAs/GaAs QW spiral laser fabricated at Virginia Tech [1]. Note the excellent current blocking capability of the p-n junction in reverse bias and the low leakage current in forward bias. The two distinct I-V curves (POS1, POS2) were taken from different spiral lasers located several millimeters apart on the same piece of QW material. The similarity in electrical performance is indicative of well-controlled growth and fabrication processes.

If these spiral lasers had a threshold current of 100 mA, and the bias current was set 50% above I_{th}, then it would be necessary to supply about 375 mW of electrical power to reach the operating point. Even if the wall-plug efficiency was as high as 60%, there would still be around 150 mW of waste heat dissipated inside the device. This situation would give rise to a heat flux of at least 240 W/cm^2 across the film/substrate interface owing to the small device area (our estimate would be substantially larger if the heat flow path was restricted to the much smaller area defined by the p-contact ring). This simple analysis demonstrates the need for careful optimization of both the electrical and optical properties of laser diodes intended for CW operation at 300K without some form of active cooling.

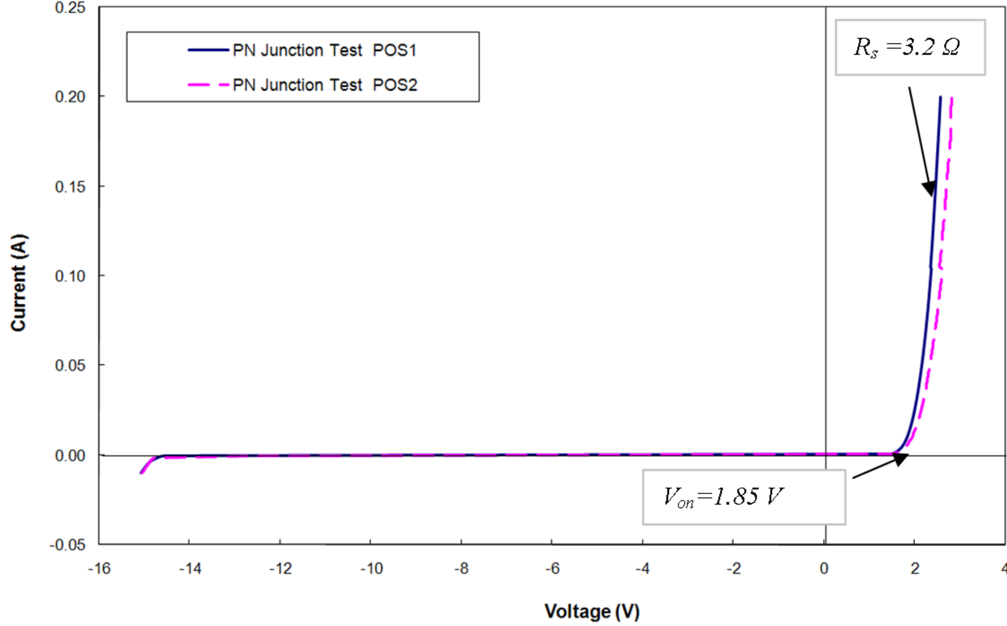

Figure 4.10: I-V data recorded using CW drive conditions at 300 K. The DUT is an oxide-confined AlGaAs/GaAs QW spiral laser fabricated at Virginia Tech. The nominal radius of the spiral cavity is 250 µm and the width of the p-metal contact ring is 25 µm. The laser material used to fabricate this device is identical to that described in Chapter 3 of this manuscript.

The electrical behavior of a p-n junction diode is conveniently described by Eq. 4.9, where k is Boltzmann's constant and T is the junction temperature. Three of the four key electrical metrics appear explicitly in this formula: reverse saturation current (I_s), diode ideality factor (η_{ideal}), and effective series resistance (R_s). The fourth parameter is known as the turn-on voltage (V_{on}).

$$I = I_s\left(e^{\frac{q(V-IR_s)}{\eta_{ideal}\cdot kT}} - 1\right) \qquad (4.9)$$

It is a straightforward exercise to obtain both V_{on} and R_s from a *linear-linear* plotting of experimental I-V data. The turn-on voltage is simply the *V-axis* intercept ($I = 0$) from the linear portion of the curve in the forward bias region. A value of V_{on} = 1.85 V was extracted in this manner from the I-V curves shown in Fig. 4.10. The target emission wavelength for this QW laser structure was λ_{QW} = 795 nm, which corresponds to an optical transition energy of E_{QW} = 1.56 eV. The turn-on voltage should be only slightly larger than this optical transition energy.

The discrepancy observed here is most likely attributable to parasitic voltage drops across the metal/GaAs(p+) interface and GaAs(p+)/AlGaAs(p) hetero-junction.

The effective series resistance of a laser diode should be evaluated in the high-voltage region ($V >> V_{on}$), where the I-V curve becomes linear and R_s is given by Eq. 4.10. Using this approach, we find $R_s = 3.2\ \Omega$ for the experimental data plotted in Fig. 4.10.

$$R_s = \left(\frac{dV}{dI} \right)_{V >> V_{on}} \qquad (4.10)$$

The diode ideality factor provides insight on the quality of material growth and fabrication processes. In the ideal case, the diode current would be attributable only to minority carrier diffusion and band-to-band radiative recombination with $\eta_{ideal} = 1$. However, any real semiconductor contains some amount of point defects and dislocations which give rise to electronic states deep within the energy band-gap [5]. These *deep-level defects* facilitate recombination of electrons and holes without photon emission and $\eta_{ideal} = 2$. The actual diode behavior is often an admixture of these two limiting cases and thus values of η_{ideal} between 1 and 2 are frequently reported in the literature.

Earlier work on GaAs [6] and AlGaAs [7] often depicts I-V characteristics dominated by $\eta_{ideal} = 2$ type behavior. Sometimes the physical location for this $\eta_{ideal} = 2$ recombination current is the *bulk* depletion region of the p-n junction [7] – this situation can be addressed during crystal growth. However, in many cases, recombination occurs primarily through surface states introduced by device processing [8]. This latter situation is a fundamental problem in III-V semiconductors, although some materials are considerably better than others (e.g., InGaAs has a much lower surface recombination velocity than GaAs). We return to this matter in Chapter 6 within the context of WGM laser performance.

Equation 4.9 can be rewritten in a form that is more useful for extracting η_{ideal} and I_s after making two straightforward modifications. First, we assume an operating current low enough so that the IR_s product in the exponent is negligible compared to V. Next, we assume the applied voltage is

large enough to make the exponential term much greater than unity. After dividing both sides of the equation by I_o = 1 A, and taking their natural logarithms, we are left with Eq. 4.11 which is our working formulation.

$$\ln\left(\frac{I}{I_o}\right) = \frac{q}{\eta_{ideal} \cdot kT} V + \ln\left(\frac{I_s}{I_o}\right) \qquad (4.11)$$

It is now obvious that both η_{ideal} and I_s can be obtained from a *log-linear* plotting of experimental I-V characteristics. The same raw I-V data shown in Fig. 4.10 is recast below in semi-logarithmic format.

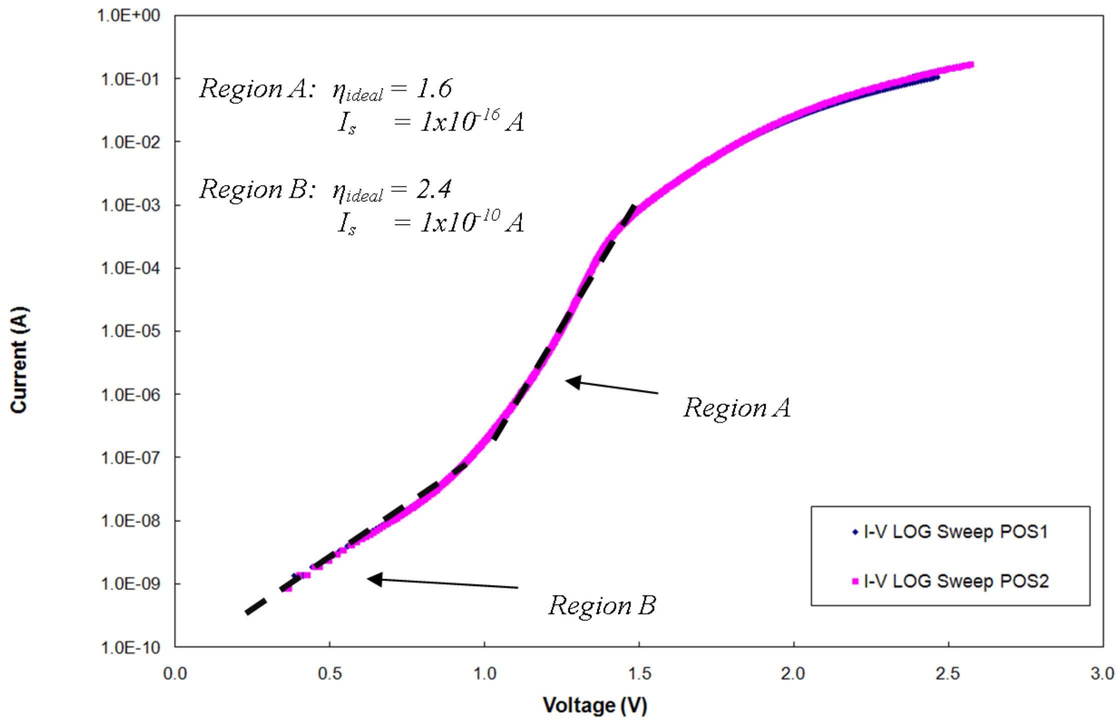

Figure 4.11: I-V data recorded using CW drive conditions at 300 K. The DUT is an oxide-confined AlGaAs/GaAs QW spiral laser fabricated at Virginia Tech. The nominal radius of the spiral cavity is 250 µm and the width of the p-metal contact ring is 25 µm. The laser material used to fabricate this device is identical to that described in Chapter 3 of this manuscript.

Two distinctly *linear* segments are evident in Fig. 4.11 at applied voltages well below V_{on} = 1.85 V. From a linear fit to data points within *Region A* we extract parameter values of η_{ideal} = 1.6 and I_s = 10^{-16} A – the latter of which was found by extrapolating to the *I-axis* intercept (V = 0).

Applying the same analytical procedure to data within *Region B* yields η_{ideal} = 2.4 and I_s = 10^{-10} A. It is evident that some other physical mechanism limits current flow above 10^{-3} A. Note that the IR_s product at I = 10^{-3} A with R_s = 3.2 Ω is much smaller than the voltage drop taken directly from the I-V curve (V = 1.5 V at I = 10^{-3} A). Therefore, the obvious degradation in the I-V curve at applied voltages greater than 1.5 V cannot be attributed to series resistance. This observation is consistent with the unusually large value of V_{on} extracted from Fig. 4.10 and ascribed above to a parasitic voltage drop.

4.3.2. Analysis of L-I Characteristics

In typical applications of laser diodes, the optical system designer first specifies a minimum acceptable value of radiated light power at a particular wavelength and then selects the appropriate component on the basis of information provided by the device manufacturer. One of the main criteria is the amount of electrical power necessary to achieve the target optical power – *the former can be reduced significantly by choosing a device with low threshold current and large L-I slope efficiency.* These important device parameters can be obtained from experimental L-I data such as that shown in Fig. 4.12.

The DUT is an edge-emitting AlGaAs/GaAs QW laser diode with a p-contact stripe width of 100 μm and a cavity length of 1000 μm [9]. The semiconductor chip is mounted on a copper slab with the p-n junction facing downward to improve heat removal during CW operation. Nevertheless, as the bias current is swept above 0.5 A under CW excitation, the L-I curve first passes through a maximum and then exhibits a negative slope (data not shown). This behavior – *often referred to as roll-over* – results from an increase in junction temperature. Note, however, that the device can be driven well above threshold under PW conditions without exhibiting roll-over or suffering from permanent failure.

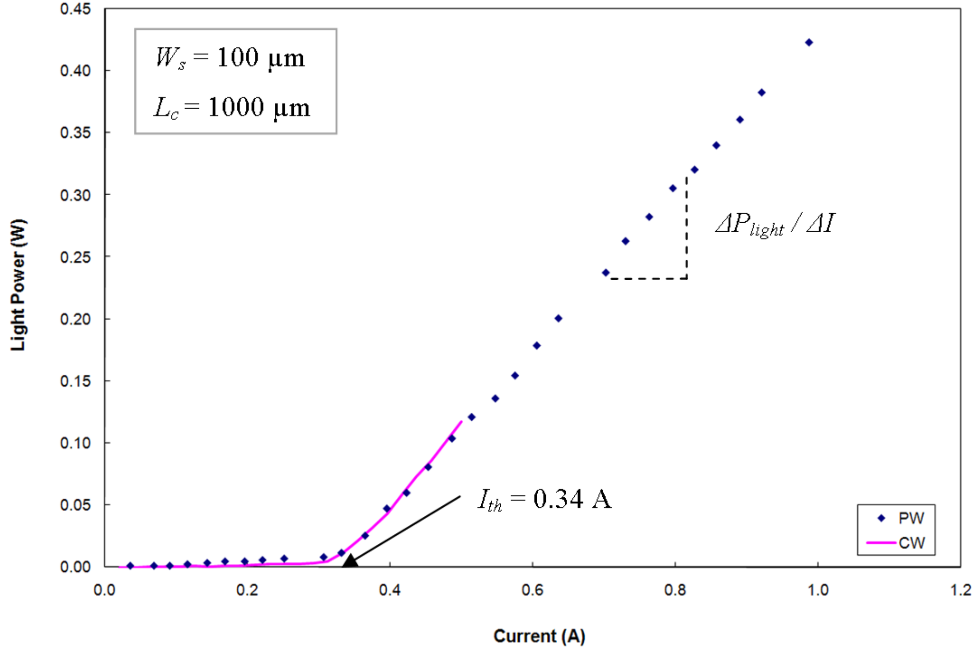

Figure 4.12: L-I data recorded under PW (symbols) and CW (solid line) excitation at 300 K. The DUT is an edge-emitting AlGaAs/GaAs QW laser diode with a p-contact stripe width of 100 µm and a cavity length of 1000 µm.

The threshold current is found by extrapolating the linear portion of the curve until it intersects the *I-axis* ($L = 0$). A value of $I_{th} = 0.34$ A was obtained in this manner from the L-I data shown above. Assuming negligible current spreading beyond the width of the p-contact stripe (i.e., W_S is the *actual width* of the lasing volume) this fitted value of I_{th} corresponds to $J_{th} = 340$ A/cm^2. Another key metric of laser performance is the slope of the L-I curve above threshold (in units of watts per ampere). This parameter can be divided by the photon energy (in electron-volts) to yield a more useful dimensionless quantity known as the *slope efficiency, η_{slope}*. Following this approach, we extract a value of $\eta_{slope} = 0.42$ ($\lambda = 806$ nm) from the L-I data plotted in Fig. 4.12. Our experimental values of J_{th} and η_{slope} are comparable to those reported in the literature for AlGaAs/GaAs QW lasers of similar construction and vintage.

4.3.3. Analysis of Emission Spectra

The spectral content of light emitted from a laser diode provides valuable information about the material structure and device geometry. Below the lasing threshold, the spontaneous emission

process is dominant and the optical spectrum takes the form of a relatively broad Gaussian-like distribution. The energy (wavelength) at which this intensity distribution reaches its maximum corresponds to the effective band-gap of the material. Such information can be used to tailor material design parameters and/or synthesis processes. In the case of a QW laser structure, the well thickness and barrier height could be adjusted, and growth interruptions introduced at the interfaces, in an attempt to match the emission wavelength with the target value for the design. Above the lasing threshold, the stimulated emission process dominates and the optical spectrum evolves into a series of narrow peaks with their wavelength separation indicative of the optical properties of the material and the geometry of the laser cavity.

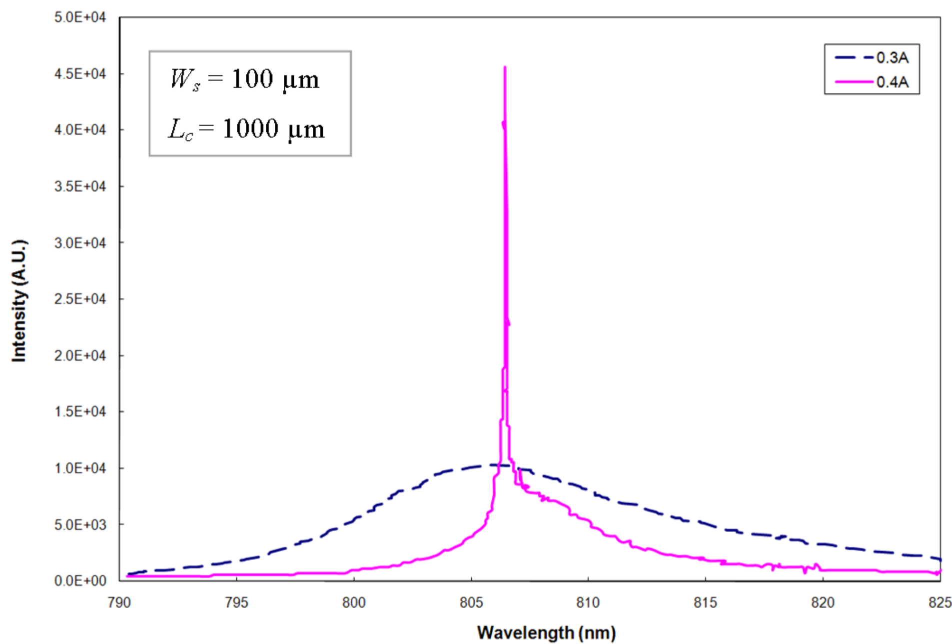

Figure 4.13: Optical spectra recorded under CW excitation at 300 K. This laser diode was fabricated in 1995 by an industrial collaborator using material nearly identical to that described in Chapter 3 of this manuscript.

A pair of emission spectra is shown in Fig. 4.13 for edge-emitting AlGaAs/GaAs QW laser diode of Section 4.2.2 [9]. When operating below threshold at I = 0.3 A (0.9I_{th}), the device emits light over a broad spectral range with a maximum at λ = 806 nm. This peak emission wavelength is close to the design target of λ_{peak} = 805 nm. The optical spectrum narrows demonstrably as the bias current is increased to I = 0.4 A (1.2I_{th}) indicating the onset of stimulated emission.

This type of *broad-area* device structure should exhibit lasing in multiple longitudinal modes. With a separation of L_c = 1000 μm between the two cleaved semiconductor facets, an effective refractive index of n_{eff} = 3.47, and λ_{peak} = 806 nm, the *free spectral range* of this dielectric cavity should be FSR = 0.09 nm. Unfortunately, the diffraction grating installed during this measurement did not provide adequate wavelength dispersion to resolve the individual longitudinal modes.

References

[1] The laser material used to fabricate this device is identical to that described in Chapter 3 of this manuscript.

[2] L. A. Coldren and S. W. Corzine, *Diode Lasers and Photonics Integrated Circuits,* Wiley, New York, 1995.

[3] P. W. A. McIllroy, A. Kurobe, and Y. Uematsu, “Ultralow threshold muliquantum well InGaAs lasers,” *IEEE J. Quantum Electron.,* vol. 21, pp. 1958-1963 (1985).

[4] A. Kurobe, H. Furuyama, S. Naritsuka, N. Sugiyama, Y. Kobubun, and M. Nakamura, “Effect of well number, cavity length, and facet reflectivity on the reduction of threshold current of GaAs/AlGaAs multiquantum well lasers,” *IEEE J. Quantum Electron.,* vol. 24, pp. 635-640 (1988).

[5] C. T. Sah, R. N. Noyce, and W. Shockley, “Carrier generation and recombination in p-n junctions,” *Proc. IRE,* vol. 45, pp. 1228-1248 (1957).

[6] H. C. Casey, Jr. and R. Z. Bachrach, “Electroluminescent shifting-peak spectra in GaAs with uniform excitation,” *J. Appl. Phys.*, vol. 44, pp. 2795 (1973).

[7] P. A. Barnes and T. L. Paoli, “Derivative Measurements of the Current-Voltage Characteristics of Double-Heterostructure Injection Lasers,” *IEEE J. Quantum Electron.*, vol. 12, pp. 633-639 (1976).

[8] H. C. Henry, R. A. Logan, and F. R. Merritt, “The effect of surface recombination on current in AlxGa1-xAs heterojunctions,” *J. Appl. Phys.*, vol. 49, pp. 3530-3542 (1978).

[9] This laser diode was fabricated in 1995 by an industrial collaborator using material nearly identical to that described in Chapter 3 of this manuscript.

5. PROCESS DEVELOPMENT FOR WGM LASERS

There are three critical process steps associated with the fabrication of our WGM lasers: (1) formation of a high-quality *μ-Pillar* optical cavity, (2) preparation of low-resistance metal contacts on both sides of the p-n junction, and (3) creation of an effective current-blocking region within the cylindrical volume defined by the inner radius of the p-metal contact ring and the combined thickness of all p-type layers. The experimental methods used to first demonstrate and then optimize these three unit processes are described in Sections 5.1, 5.2, and 5.3.

5.1. Formation of μ-Pillar Optical Cavities

The question of how best to define the optical cavity of a WGM laser is of paramount importance. Any candidate technique, regardless of the specifics, must fulfill the following requirements: (a) high degree of anisotropy, (b) low etch selectivity among materials in the multi-layer laser structure, and (c) low surface roughness and subsurface damage. The development of this unit process was separated into two tasks: (1) evaluation of candidate techniques and (2) optimization of chosen methods for our specific device design and process flow. Our key findings are described below.

5.1.1. Evaluation of Fabrication Methods

There were two fabrication techniques to consider; namely, liquid chemical or “wet” etching and gaseous plasma or “dry” etching, and we applied a common methodology to evaluate their usefulness. The starting material was a small lot of 350 μm thick, semi-insulating (SI) GaAs substrates with (100) surface orientation [1]. Each of these 50 mm diameter “epi-ready” wafers was cleaved into eight rectangular samples (7 mm x 12 mm). In preparation for every process run, we defined a photoresist (*PR*) etch mask on at least one GaAs sample using conventional lithographic techniques. The geometric mask pattern was an array of 20 μm wide *PR* stripes on 250 μm centers running parallel to one of the surface normal vectors for {011} cleavage planes. A 3-D rendering of this *test structure* is shown in Fig. 5.1 with the relevant low-index crystal planes labeled for specificity.

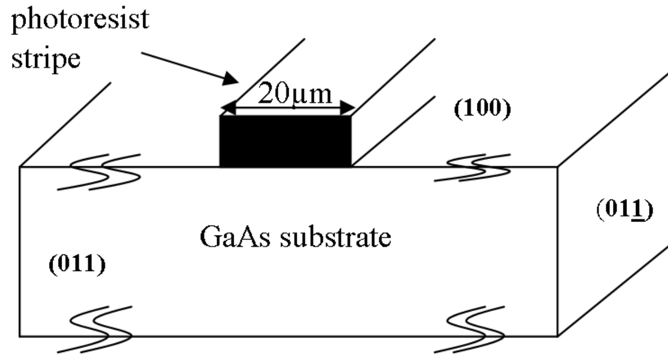

Figure 5.1: 3-D view of *test structure* used during wet and/or dry etching runs. The materials of construction are GaAs and photoresist. The relevant low-index FCC crystal planes are labeled using standard notation.

Wet etching was evaluated first owing to its simplicity and the potential for preparing smooth cavity sidewalls with no subsurface damage. The chemistry of choice was $1H_2SO_4$:$8H_2O_2$:$80H_2O$ because we used it before successfully to fabricate AlGaAs/GaAs QW ridge lasers. This etching solution does create very smooth sidewalls and it removes GaAs and $Al_xGa_{1-x}As$ materials at similar rates (15 nm per second). In this earlier work, the target ridge heights were between 0.2 and 0.5 μm so mask undercutting was not a major concern. In the present case, however, we must remove almost 4 μm of semiconductor material to define the optical cavity of a WGM laser. So, we reevaluated the $1H_2SO_4$:$8H_2O_2$:$80H_2O$ solution for this specific application.

First, we prepared two different *test structures* with *PR* stripes running along orthogonal <011> directions. Next, we etched them in a stagnant $1H_2SO_4$:$8H_2O_2$:$80H_2O$ mixture held at 20 C under normal cleanroom lighting. Finally, we cleaved them perpendicular to the *PR* stripes – that is, through either the (011) or (01$\underline{1}$) crystal planes. SEM images of GaAs sidewall profiles formed by wet etching are shown in Fig. 5.2. The photoresist was not removed after etching so as to more easily assess the extent of mask undercutting. It is obvious that undercutting was quite severe, and that it was not possible to obtain near-vertical sidewalls ($\theta \approx 90$ degrees). Moreover, the sidewall profiles exhibit distinct crystallographic *habits* as a result of strong chemical selectivity between (111A) and (111B) planes of the zincblende crystal structure.

A careful examination of recent literature suggests that these problems could be mitigated *somewhat* by choosing another wet-etch chemistry – nevertheless, the basic tendencies would remain as impediments to success. As a consequence, we concluded that wet etching was not a viable option for fabricating our μ-*Pillar* laser cavities.

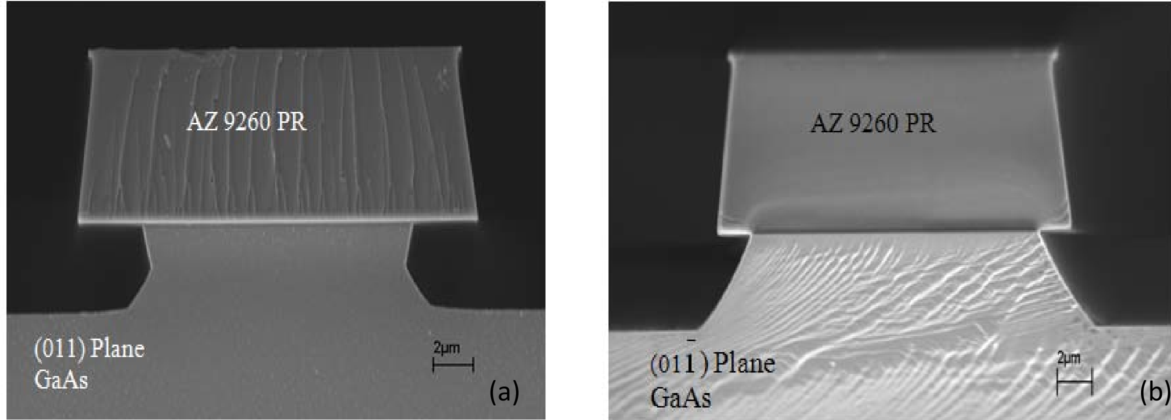

Figure 5.2: SEM images of sidewall profiles for test structures patterned using wet etching. The photoresist stripe orientation was parallel (a) or perpendicular (b) to the [011] crystal direction.

In contrast to liquid solution based etching, gaseous plasma etching can be highly anisotropic, independent of crystal orientation, insensitive to alloy mole fraction and doping species, and capable of fine pattern delineation. Anisotropic etching of GaAs was demonstrated previously by several groups using Cl_2 gas in a reactive-ion etching (RIE) system [2-4]. In most cases, the GaAs etch rate was satisfactory but the etch rate for AlGaAs was considerably lower (under identical conditions). This behavior has been attributed to the formation of aluminum oxide, which has an extremely low etching rate [5], or other non-volatile materials, in the presence of residual oxygen, water or carbon-containing materials. This *self-masking* effect gives rise to a non-uniform sidewall profile when etching AlGaAs/GaAs laser structures [6]. Several attempts have been made to address this problem by using other Cl_2-containing gas mixtures, such as CCl_4/Cl_2 [7] and Cl_2/Ar [8], but these trials have met with only limited success.

We have chosen to work with a BCl_3-Cl_2 gas mixture, expecting BCl_3 to remove the aluminum oxide [9] and to scavenge the residual oxygen and water vapor [10]. In addition, BCl_3 has a

specific advantage over CCl_4 in that it does not form carbon-based polymer films which may limit (or completely block) the chemical component of plasma etching [11]. Furthermore, we have opted to employ the *inductively-coupled plasma* (ICP) etching technique instead of the more conventional RIE method. In an ICP etching system, the act of creating the gaseous plasma of reactive ions is largely decoupled from that of accelerating these ions towards the sample surface. Consequently, the plasma density, which impacts the *chemical* component of dry etching, can be adjusted without having a strong influence on the kinetic energy of ions impinging on the surface (i.e., the *physical* component of the process).

After selecting the gas chemistry and dry etching technique, we refocused our attention on choosing an appropriate material for "masking" (protecting) the semiconductor during etching. Thin metal films of nickel [12] or chromium [13] exhibit a high etch selectivity with respect to $Al_xGa_{1-x}As$ materials when exposed to chlorine-containing plasmas. It is however difficult to remove these metal films (after etching) without simultaneously damaging the AlGaAs/GaAs QW structure. Moreover, upon rendering such polycrystalline metal films into a 2-D mask pattern, a "grain-like" texture often appears at the edges of mask features. If the dry etching process was truly anisotropic then any such mask-edge roughness would be transferred directly to the semiconductor sidewalls.

Others have shown that dielectric thin films, such as SiO_2 or Si_3N_4, can be used to produce high-quality semiconductor laser facets via dry etching [14]. This class of materials also exhibits very low etching rates in chlorine gas chemistry in comparison to those found for $Al_xGa_{1-x}As$ alloys. In contrast to metal films, these amorphous materials do not contain grain boundaries and thus should not have the same limitation with regard to mask-edge roughness. Unfortunately, mask removal (after etching) remains as a serious problem with silicon-based dielectric films. All known wet etching solutions for SiO_2 and Si_3N_4 contain strong acids that attack GaAs and/or AlGaAs (e.g., very high etch rates are observed for $Al_xGa_{1-x}As$ alloys with $x \geq 0.25$ in buffered HF solution). Another method for removing these dielectric masks is dry etching in CF_4 and/or SF_6 gas mixtures. It would be preferable, however, to avoid a second dry etching step as it may

introduce additional surface and/or sidewall damage (i.e., physical sputtering of semiconductor surfaces may occur coincidentally with removal of the dielectric film).

Given the shortcomings of other masking materials, we concluded that a thick photoresist film was the most viable alternative. We chose to evaluate AZ 9260 positive resist [15] as the *lone* mask layer in our Cl_2/BCl_3 etching process. This special polymeric formulation has several key attributes [16]:

(1) Compatible with aggressive plasmas and high temperatures and thus does not degrade during the etching process.

(2) Etch selectivity of 10:1 over GaAs and $Al_xGa_{1-x}As$ alloys in Cl_2/BCl_3 gas chemistry.

(3) Soluble in acetone and therefore easily removed after etching without degrading sidewalls of optical cavity.

This concludes our evaluation of options for defining *μ-Pillar* laser cavities. We now describe below our efforts to optimize the critical process steps.

5.1.2. Optimization of Dry Etching Process

Our process optimization work was focused on achieving two objectives: (1) defining a robust *PR* mask to protect the optical cavity during etching and (2) manipulating the dry etching process itself to achieve high-quality *μ-Pillar* sidewalls. With regard to the *PR* etch mask, we began by identifying a suitable photomask technology for lithographic pattern transfer into the AZ 9260 resist layer. The primary criteria were minimizing long-range *undulations* and short-range *roughness* along the metal stripe edges and achieving an *abrupt decrease* in metal thickness at the stripe boundaries. In order to ensure the best possible results, we chose a well-known commercial photomask vendor and made use of their most advanced manufacturing tools [17].

The second task was to form a *PR* mask that was robust enough to survive the aggressive chemical and physical conditions associated with the dry etching environment. In this regard,

the “soft-bake” (SB) and “hard-bake” (HB) conditions are the most important process variables. The final sidewall profile of the *PR* stripes is very sensitive to the conditions used for the SB step. The HB step further hardens the photoresist and thus minimizes its deterioration during the dry etching process. The process flow starts by spin-casting AZ 9260 to a specific layer thickness onto the sample, and then soft-baking it to remove volatile solvents. Since AZ 9260 is a *positive* resist it must be exposed to UV light to increase its solubility in the “developer” solution. A Karl-Suss MA-6 mask aligner was used in conjunction with the photomask to illuminate the *PR* film with UV light in the desired 2-D geometry. After developing the exposed *PR* to form the mask pattern, the sample was hard-baked to *condition* the resist for dry etching.

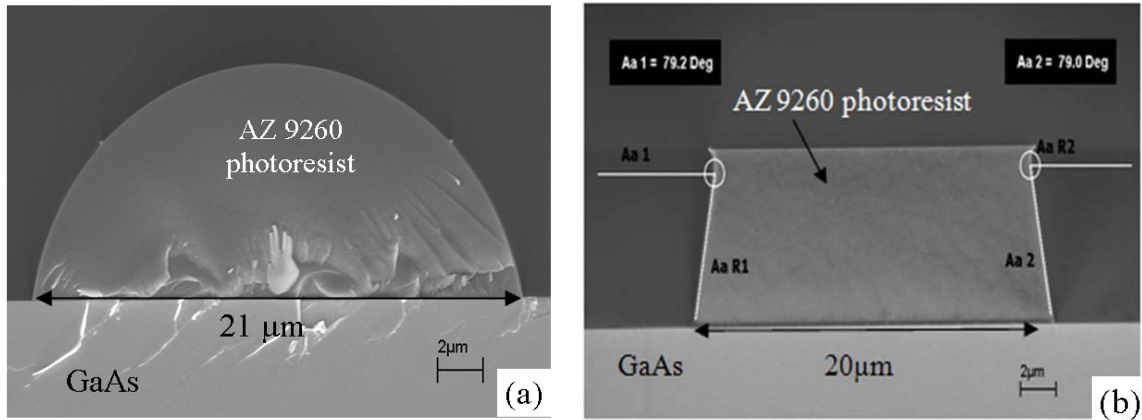

Figure 5.3: AZ 9260 profiles after soft-baking, UV exposure and development, followed by hard-baking. In (a) SB was performed at 100 °C for 1 min and in (b) SB = 115 °C for 3.5 min. In both cases, the HB step was done at 120 °C for 5 min.

On the basis of our literature review, and consultations with the photoresist manufacturer, we decided to set the hard-bake condition at 120 °C for 5 min while varying the soft-bake parameters. The SEM image in Fig. 5.3a demonstrates that soft-baking at 100 °C for 1 min gives rise to a distorted *PR* stripe profile with an effective width (at the interface with the GaAs substrate) of 21 μm instead of the stripe width on the photomask itself of 20 μm. Note that this 1 μm off-set is not expected to change much with feature size so the discrepancy would be larger for smaller features. The situation was improved considerably by adjusting the SB parameters to 115 °C and 3.5 min. In this case, shown in Fig. 5.3b, the AZ 9260 profile takes the expected shape and the sidewall angle approaches 80 degrees. Furthermore, the measured *PR* stripe width

reproduces the photomask feature size of 20 μm. The impact of dry etching on the *PR* masks formed using these two SB conditions is illustrated in Fig. 5.4. The distorted *PR* profile of Fig. 5.3a was further modified by the dry etching environment, as shown in Fig. 5.4a. However, the well-formed *PR* stripe of Fig. 5.3b held its shape during dry etching, as evidenced in Fig. 5.4b. Additional details of the optimized *PR* masking procedure may be found in Table C.1 of Appendix C.

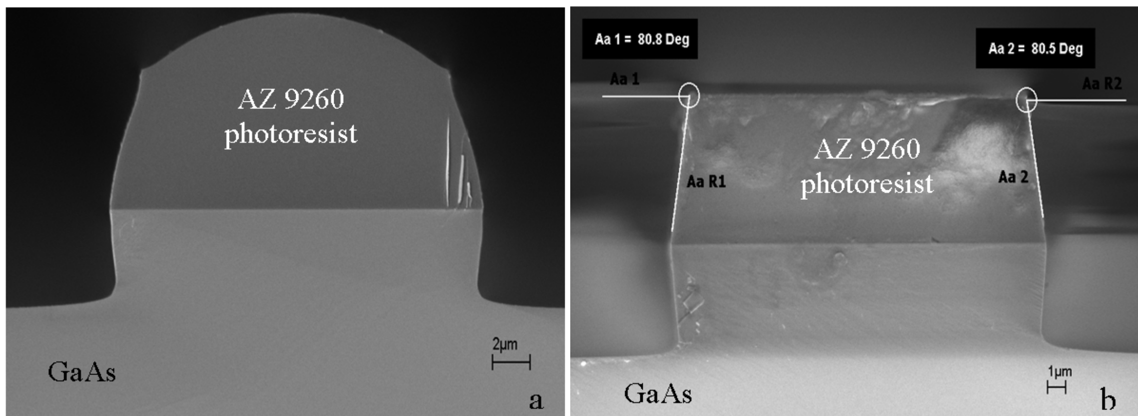

Figure 5.4: AZ 9260 profiles after completing both *PR* mask definition and dry etching processes. In (a) SB was performed at 100 °C for 1 min and in (b) SB = 115 °C for 3.5 min. In both cases, the HB step was done at 120 °C for 5 min.

The remainder of our optimization activity was focused on the ICP etching process itself. We began by establishing good ICP etching conditions for the GaAs *test structures* described above (see Fig. 5.1). In preparation for etching, each small piece of GaAs (7 x 12 mm^2) was placed on a 4" diameter silicon *handle* wafer to simplify loading/unloading into the ICP chamber. Unfortunately, this action introduced a thermal management issue since the GaAs samples were not in direct contact with the temperature controlled chuck. As a consequence, the AZ 9260 masking stripes would degrade significantly during etching and the resultant sidewall profiles were not acceptable. We addressed this problem by coating the backside of the GaAs sample with thermal paste before attaching it to the silicon wafer [18]. This modified sample mounting procedure ensured good thermal conductivity across the GaAs/Si interface and thus prevented overheating of the *PR* masking stripes.

A total of seven ICP etching runs were performed with at least one key parameter – such as Cl_2 flow rate, BCl_3 flow rate, RIE power, ICP power, or chamber pressure – differing between successive experiments. The etching time was fixed at 4 min in all cases. A complete listing of process parameters is given in Table 5.1. After etching, the GaAs test structures were cleaved perpendicular to the masking stripes, the photoresist was dissolved in acetone, and the samples were loaded into the SEM for imaging. The physical observables of most interest were the *roughness* and *verticality* of the etched GaAs sidewalls. We used a simple numbering scheme to classify sidewall roughness with 1 and 5 representing the smoothest and roughest surfaces, respectively.

Table 5.1: Parameters for ICP etching study on (100) GaAs substrates (etching time = 4 min).

Run #	**Cl_2 Flow (sccm)**	**BCl_3 Flow (sccm)**	**RIE Power (W)**	**ICP Power (W)**	**Chamber Pressure (mTorr)**	**Etch Depth (μm)**	**Sidewall Roughness**	**Sidewall Profile**
I-1	3	20	50	320	10	4.46	1	Fig. 5.5a
I-2	3	17	50	320	10	4.46	1	not shown
I-3	3	17	25	320	10	5.05	3	Fig. 5.5c
I-4	1	19	55	320	10	1.42	1	Fig. 5.5d
I-5	3	17	50	320	50	5.52	5	Fig. 5.5b
I-6	4	16	50	320	10	6.38	4	not shown
I-7	3	20	50	500	10	4.88	1	not shown

A select group of SEM photographs is presented in Fig. 5.5 with the sidewall angles labeled for clarity. The cross-sectional stripe profiles of Fig. 5.5a and 5.5d exhibit sidewall angles close to 90 degrees, which was our target value. These two sets of etching parameters also gave rise to smooth sidewalls (see Runs I-1 and I-4 in Table 5.1). However, the etching rate for Run I-1 was considerably higher than that for Run I-4. The ICP etch rate appears to be most strongly influenced by the Cl_2 molar gas ratio – the former increased from 0.35 to 1.59 μm/min in response to an increase in the latter from 0.05 to 0.2 (see Runs I-4 and I-6 in Table 5.1). Unfortunately, in the latter case, the increase in etch rate was accompanied by significant

sidewall roughening. Lowering the RIE power and/or increasing the chamber pressure gave rise to a less anisotropic etch profile, as evidenced by Fig. 5.5b and 5.5c. On balance, the ICP etching parameters of Run I-1 produced the best GaAs sidewalls (nearly vertical and very smooth) at an acceptably high etch rate.

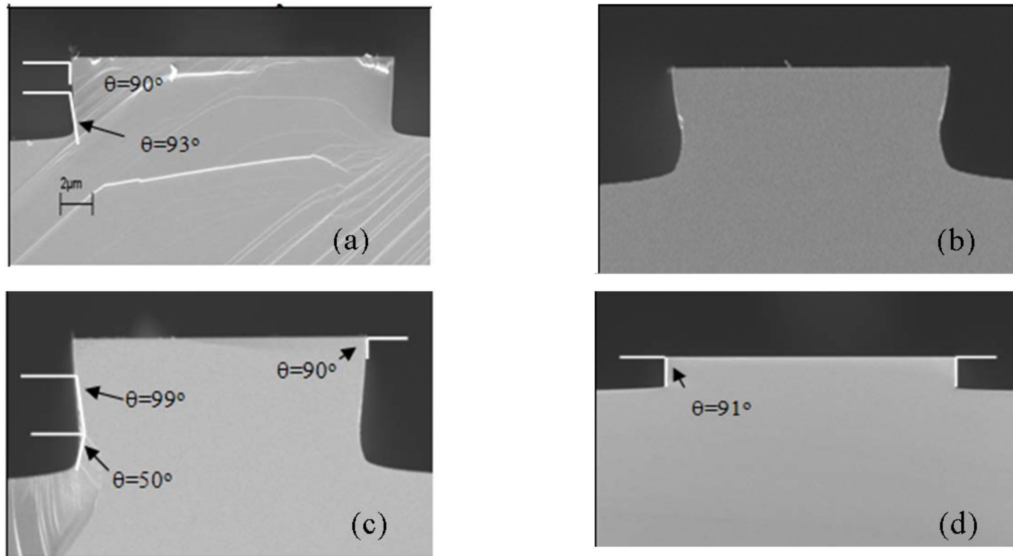

Figure 5.5: SEM images of sidewall profiles from the ICP etching study performed on GaAs test structures. Only four of the seven process runs listed in Table 5.1 are shown here for brevity: (a) Run # I-1, (b) I-5, (c) I-3, and (d) I-4.

As mentioned above, the Cl_2/BCl_3 gas chemistry has been employed by others in an RIE configuration to yield featureless AlGaAs/GaAs laser mirrors [14]. We must reproduce (or improve upon) these etch characteristics in our present work on *μ-Pillar* cavities with circular symmetry, because the optical scattering loss depends critically on sidewall quality [19]. Figure 5.6 shows two *off-axis* SEM images of GaAs sidewalls defined by ICP etching. The contrast variations observed in these photographs were quite sensitive to the specific imaging configuration. In order to minimize experimental bias, we began each SEM session by imaging the cleaved GaAs facet after adjusting the sample tilt to align the surface normal with the incident electron beam. After establishing this reference condition, the samples were tilted by a small (fixed) angle away from the electron beam and then refocused for imaging. It is obvious from Fig. 5.6a that the ICP etch parameters of Run I-5 gave rise to rough sidewalls. This level of

roughness was given the worst score of “5” in Table 5.1. In contrast, the companion SEM image of Fig. 5.6b shows that Run I-1 produced very smooth GaAs sidewalls. This degree of roughness was assigned the best score of “1” in Table 5.1.

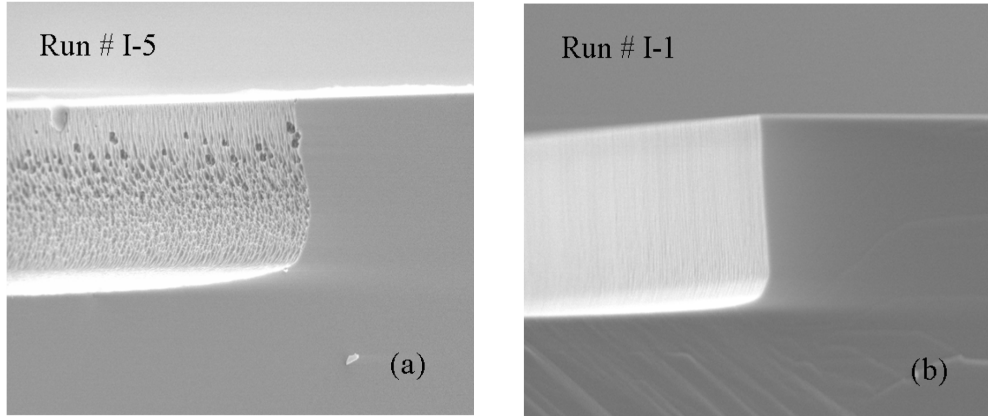

Figure 5.6: SEM images of sidewall roughness from ICP etching study on (100) GaAs substrates: (a) maximum and (b) minimum roughness.

After identifying the optimum ICP etching parameters, we devised a simple procedure to check for process uniformity and reproducibility. Four physical observables were measured at six different cleavage locations on two separate GaAs samples: θ_1 (θ_2) = sidewall angle on the left-hand (right-hand) side of the stripe, etch depth, and stripe width. The separation between any two cleavage locations was roughly 2 mm so as to capture the largest possible variations. Table 5.2 summarizes the results of this experiment. The reported standard deviations for each observable are well within acceptable limits.

Table 5.2: Average values and standard deviations for key physical observables associated with the optimized ICP etching process.

Parameter	**Units**	**Average Value**	**Standard Deviation**
stripe width	μm	20.1	0.14
etch depth	μm	4.6	0.13
θ_1	degrees	94.2	0.59
θ_2	degrees	90.2	0.62

Other workers have already demonstrated equal-rate etching of GaAs and AlGaAs using a Cl_2/BCl_3 gas mixture in an RIE system [11]. Nevertheless, given our alternative choice of ICP etching, combined with the wide range of aluminum mole fractions and doping species and concentrations under consideration, we decided to conclude this optimization study with a set of trial runs on the actual AlGaAs/GaAs QW laser material itself. On the basis of our previous results for GaAs substrates, we held the ICP power constant at 320 W and the chamber pressure at 10 mTorr throughout these experiments. In this case, however, our goal was to etch all the way through the material structure down to the GaAs substrate so as to create the largest possible refractive index step at the edge of the *μ-Pillar* laser cavity. With this objective in mind, we adjusted the process times in accordance with the observed etch rates for GaAs to obtain an etch depth of roughly 4 μm (except for run number II-5). The ICP parameters and corresponding physical observables are given in Table 5.3. The experimental trends are consistent with those found in our etching study on GaAs substrates.

Table 5.3: Parameters for ICP etching study on an AlGaAs/GaAs QW laser structure (ICP power = 320 W / chamber pressure = 10 mTorr).

Run #	**Cl_2 Flow (sccm)**	**BCl_3 Flow (sccm)**	**RIE Power (W)**	**Etch Time (sec)**	**Etch Depth (μm)**	**Sidewall Roughness**	**Sidewall Profile**
II-1	3	20	50	240	4.0	1	Fig. 5.7a
II-2	3	17	50	215	4.3	1	not shown
II-3	3	17	25	190	4.6	4	Fig. 5.7b
II-4	1	19	50	632	4.4	1	Fig. 5.7c
II-5	1	19	25	558	5.5	6	Fig. 5.7d

A representative group of SEM photographs is presented in Fig. 5.7 to illustrate these findings. Given the more physical (less chemical) nature of dry etching processes in general, we had expected that the etched sidewall profiles would follow the shape of the photoresist mask. Since this correlation was not observed during our initial study on GaAs, we did not remove the *PR* masks this time before loading the etched laser structures into the SEM for imaging. Once again,

we found that the etched sidewall angles do not correlate well with the *PR* mask profiles, as evidenced in Fig. 5.7. We attribute this behavior to limitations in the pumping capacity of our ICP etching system. Under actual process conditions, we were not able to bring the chamber pressure below 8 mTorr. According to literature reports on the RIE process, the etched sidewall angle does not mimic the *PR* mask profile unless the chamber pressure is held below 2 mTorr.

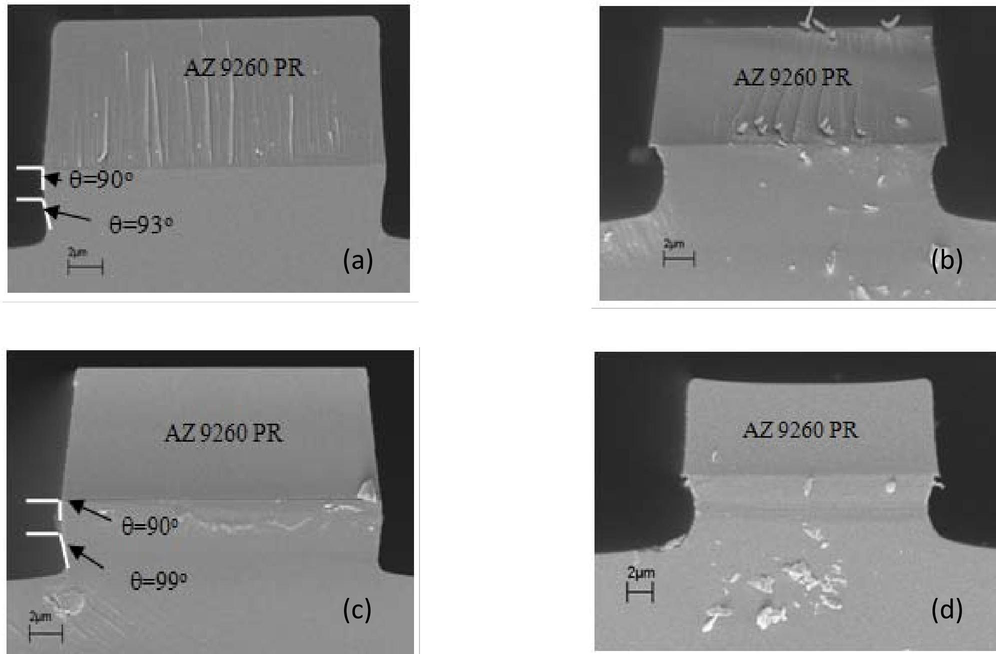

Figure 5.7: SEM images of side-wall profiles from the ICP etching study performed on AlGaAs/GaAs QW laser structures. Only four of the five process runs listed in Table 5.3 are shown here for brevity: (a) Run # II-1, (b) II-3, (c) II-4, and (d) II-5.

Despite this equipment limitation, the ICP etching parameters of Run II-1 gave rise to nearly vertical sidewall profiles and smooth surfaces for our AlGaAs/GaAs QW laser structures (note that these etch parameters are identical to those of Run I-1 from the GaAs study). Figure 5.7a reveals an etched sidewall angle of 90 degrees down to about 1 μm below the surface, which then increases slightly to 93 degrees over the remaining 3 μm of sidewall. The off-axis SEM image for this sample (not shown here) is nearly identical to Fig. 5.6b. We observed less anisotropic etch profiles when the RIE power was reduced from 50 to 25 W, as evidenced by

Fig. 5.7b and 5.7d. This behavior is consistent with our findings on ICP etching of semi-insulating GaAs substrates.

5.2. Preparation of Metal/Semiconductor Contacts

"Ohmic" metal/semiconductor junctions or *contacts* serve as the electrical interface between an active semiconductor device and its passive external drive circuitry. The contact must be able to supply the necessary bias current, and the voltage drop across it should be small compared to that across the semiconductor active region. An ideal metal/semiconductor contact should have a *linear* relationship between current and voltage – that is, it should follow Ohm's law. The highest level of device performance cannot be attained *unless the associated metal/semiconductor contacts are ohmic in nature with the lowest possible contact resistance* (R_c).

The methods used to form metal/semiconductor contacts have been studied extensively by materials engineers over several decades; nonetheless this subject remains more of an art than a science. The basic processing flow is straightforward: (1) semiconductor surface cleaning and native oxide removal, (2) contact metal deposition and patterning, and (3) thermal annealing. Residual organic contamination is removed from the semiconductor surface by soaking the sample in warm solvents (acetone, isopropyl-alcohol). Trace metal removal is accomplished by etching in acidic and/or basic solutions that do not attack the semiconductor itself. The native oxide layer at the semiconductor surface is stripped off using another acid and/or base solution. The requisite metal films are deposited under high vacuum conditions using an electron-beam evaporator. Contact patterning is done using standard lithographic techniques such as "lift-off" where the contact metals are deposited through holes in a *PR* film that is later dissolved away. Finally, the deposited metal/semiconductor composite is subjected to thermal annealing – sometimes referred to as "alloying or "sintering" – in order to improve adhesion and promote ohmic behavior.

In the present case, ohmic metal contact formation on p-n junction lasers requires that we develop optimum process conditions for both p-type and n-type semiconductor materials. The p-

side metallization consists of a Ti (30 nm) / Au (200 nm) bi-layer film. The titanium is used to promote good adhesion and the gold cover film provides a non-reactive surface suitable for wire bonding and/or die attachment. The influence of annealing time, τ_{anneal}, on the I-V characteristics for our Ti/Au p-contact metallization is shown in Fig. 5.8. These process trials were executed using p+ GaAs substrates with doping concentration nearly identical to that for the topmost p+ GaAs capping layer of the AlGaAs/GaAs QW laser structure. The contact exhibits *linear* behavior even in the as-deposited state, but the resistance is high. Annealing at 400 °C lowers R_c by factor of 6.3 relative to the as-deposited case. After annealing for 10 minutes, the surface morphology of the metal composite film begins to degrade.

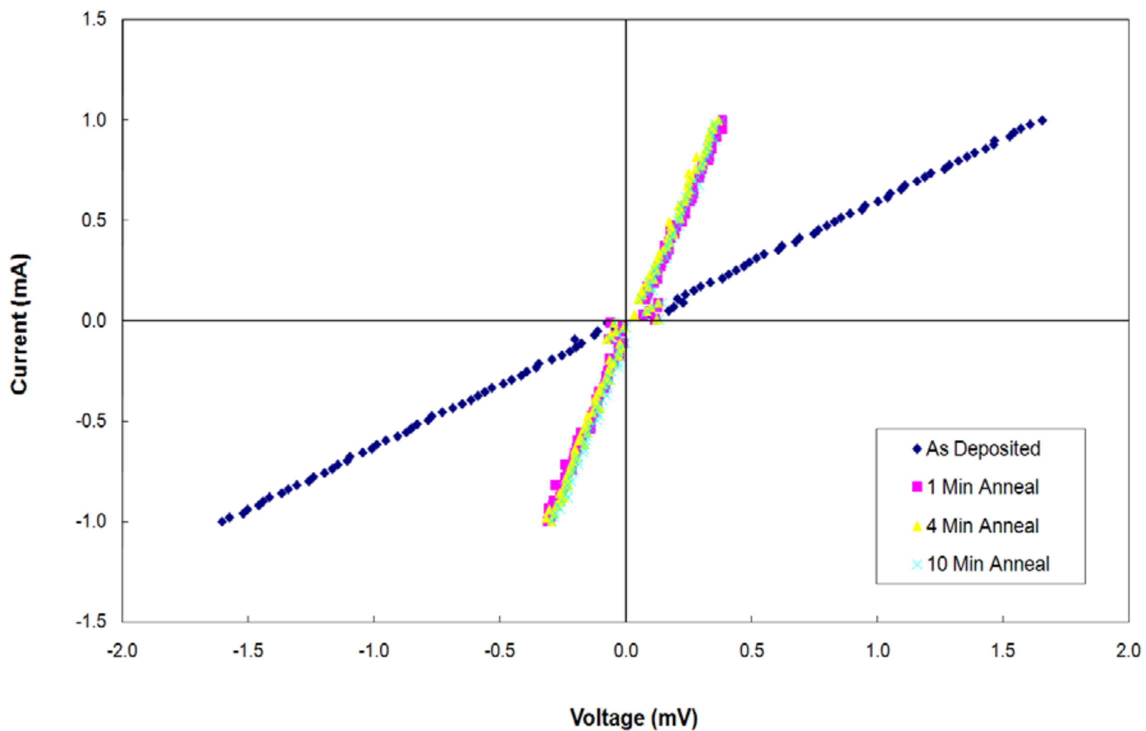

Figure 5.8: Electrical characteristics from preliminary study of p-side (Ti/Au) contact metallization. Annealing times range from $1 \leq \tau_{anneal} \leq 10$ minutes with the temperature held at T_{anneal} = 400 °C (for all cases).

The n-contact metallization consists of a Sn (20 nm) / Au (110 nm) bi-layer film. Tin is a column IV element and thus acts as a donor when incorporated on the column III sublattice of III-V compound semiconductors. The ratio of Sn to Au is chosen to form a eutectic alloy. Upon

thermal annealing, a thin layer of the GaAs substrate dissolves into the eutectic melt. As the sample cools to room temperature this multi-component liquid solution acts as a source for the recrystallization of heavily doped n-type GaAs (containing a large concentration of Sn donors). Nonetheless, the contact surface remains *Au-rich* making it less susceptible to oxidation than pure Sn – an attribute that is useful for device packaging purposes. The influence of τ_{anneal} on the I-V characteristics for our n-contact Su/Au contact metallization is shown in Fig. 5.9. These process runs were performed using n+ GaAs substrates with doping concentration identical to that for the bottom-most n+ GaAs substrate side of the AlGaAs/GaAs QW laser structure. The contact exhibits *non-linear* behavior in the as-deposited state but it becomes ohmic after annealing at 400 °C for 1 minute. Additional annealing for up to 10 minutes results in a 1.4x *increase* in R_c relative to the τ_{anneal} = 1 minute case (see Fig. 5.9, insert).

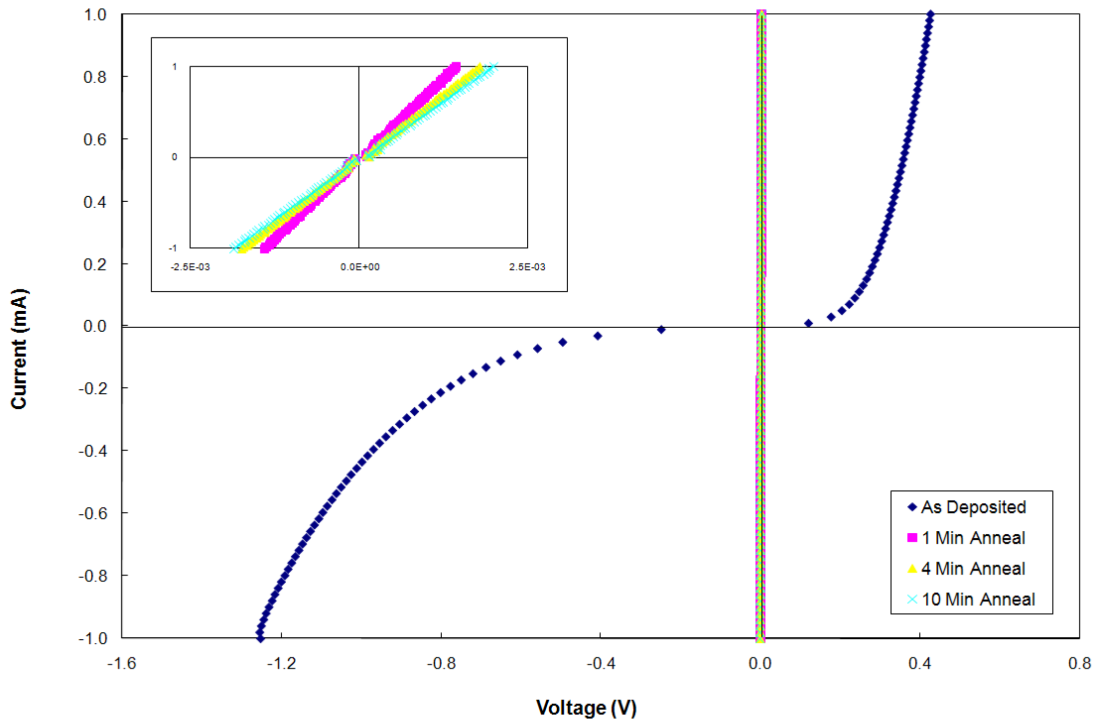

Figure 5.9: Electrical characteristics from preliminary study of n-side (Sn/Au) contact metallization. Annealing times range from 1 < τ_{anneal} < 10 minutes with the temperature held at T_{anneal} = 400 °C (for all cases). The insert is a higher resolution plot near the origin of the I-V curve.

The discrepancy between p-side and n-side contact behavior in the *as-deposited state* is attributable to the different acceptor/donor doping levels in the GaAs substrates used in the trial

runs ($N_A = 2 \times 10^{19}$ cm^{-3} / $N_D = 2 \times 10^{18}$ cm^{-3}). The ten-fold increase in acceptor doping causes substantial narrowing of the potential energy barrier at the metal-to-semiconductor interface, and thereby supports a large increase in tunneling current in response to a small change in applied voltage.

These preliminary trials demonstrated we had viable processes for making ohmic contacts to both p-type and n-type GaAs. The final judgment could not be made, however, until we tested these prototype recipes on p-n AlGaAs/GaAs QW structures [20]. A schematic of the *p-n junction test device* used during the final evaluation phase is shown in Fig. 5.10. The p-side contact metal (Ti/Au) was prepared using electron-beam evaporation and lift-off. A circular-shaped pattern was formed with a diameter of 500 μm, which then served as a mask for ICP etching of the AlGaAs/GaAs QW structure all the way down to the top-surface of the n+ GaAs substrate.

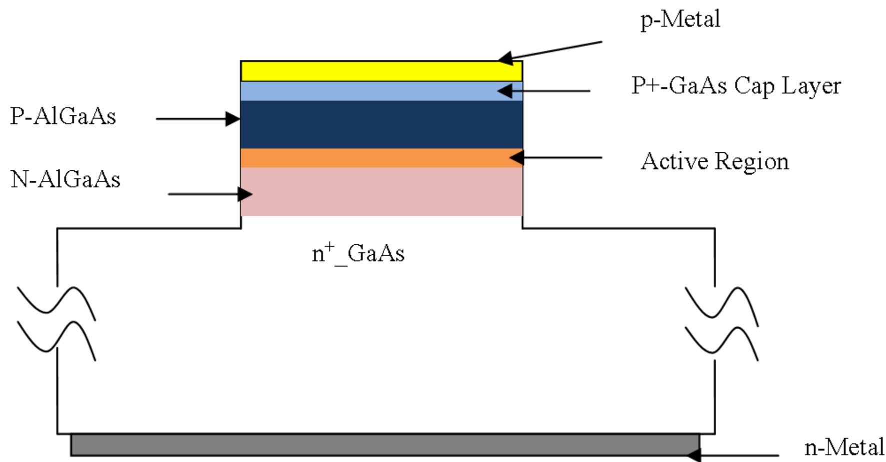

Figure 5.10: Cross-sectional view of *p-n junction test device* fabricated from AlGaAs/GaAs QW structure during the final phase of metal contact evaluation.

The n-side metallization (Sn/Au) was deposited by electron-beam evaporation. A *broad-area* contact was adequate for the back-side of the n+ GaAs substrate. After examining the results from several trial runs during which the p-side and n-side contacts were annealed using different process conditions, we concluded that it was preferable to anneal both contacts simultaneously at

400 °C for 5 minutes. This heat treatment was performed under an ambient of forming gas (3.99% mixture of H_2 in argon) to prevent metal oxidation.

The electrical performance of the *p-n junction test device* can be evaluated from the I-V data shown in Fig. 5.11. For the as-deposited case, the turn-on voltage is quite large, V_{on} = 5.1 V; however, it decreases with annealing time until reaching V_{on} = 1.48 V at τ_{anneal} = 10 minutes. This experimental value of V_{on} is actually 80 meV *below* the design target for the QW transition energy, E_{QW} = 1.56 eV. Thus, we do not expect that this *near ideal* situation would be improved by making τ_{anneal} longer than 10 minutes.

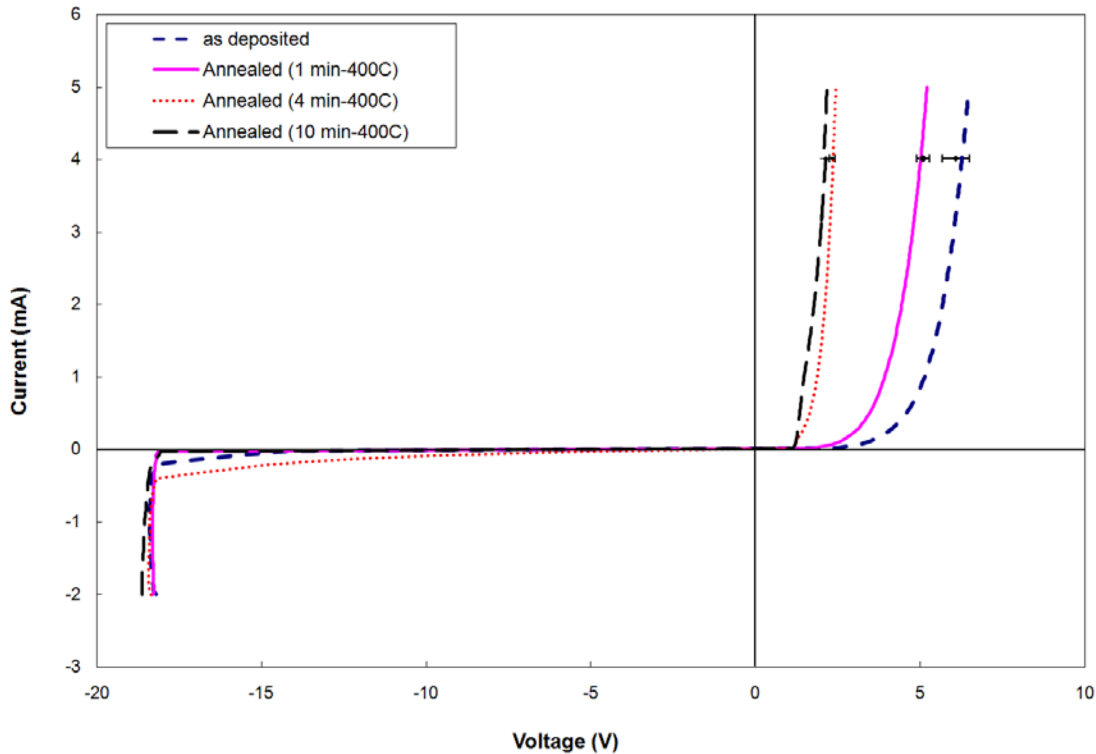

Figure 5.11: Electrical characteristics for *p-n junction test device* with p-side and n-side metal contacts formed under optimum conditions. Annealing times range from 1 < τ_{anneal} < 10 minutes with the temperature held at T_{anneal} = 400 °C (for all cases).

It is also of interest that the p-side contact on the *p-n junction test device* responds to thermal annealing in a manner very similar to that observed during our preliminary trials. The Ti/Au metallization begins to roughen, and then blisters, as the annealing time approaches ten minutes

(T_{anneal} = 400 °C). Despite these undesirable physical changes, the I-V characteristic improves slightly as the annealing time increases from 4 to 10 minutes (see Fig. 5.11).

Five separate devices were tested for each annealing condition with their locations ranging across the entire 7 mm x 12 mm sample. The individual data points with error bars overlaying each curve represent average values and standard deviations of the applied voltage necessary to induce a current flow of 4 mA. These error bars provide an estimate of the combined variability associated with crystal growth, device processing, and device testing.

5.3. Current Blocking via Hydrogen Passivation

In order to minimize the threshold current and maximize the differential quantum efficiency of semiconductor lasers, it is essential that current, carriers, and photons are all confined to a predetermined *electronic gain volume* that is similar to the *optical mode volume* [21-23]. In the transverse direction – *perpendicular to the plane containing the active region* – carrier and photon confinement is accomplished through proper design of the multi-layer semiconductor heterostructure (for all types of lasers). In the lateral direction – *perpendicular to the direction of electromagnetic mode propagation and in the plane of the active region* – confinement is often achieved "post-growth" using one of the following methods: oxide masking [24], ridge etching [25], proton bombardment [26], or semiconductor re-growth [27,28].

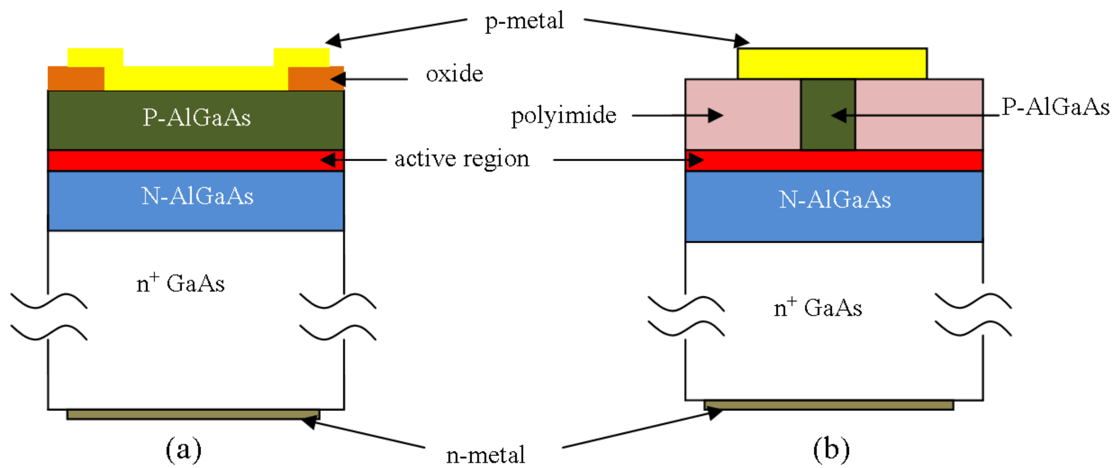

Figure 5.12: Cross-sectional view of two different device embodiments for achieving lateral confinement: (a) oxide-stripe laser and (b) ridge-waveguide laser.

Two examples are shown in Fig. 5.12 of laser devices with different levels of sophistication with regard to lateral confinement. Figure 5.12a illustrates an oxide-confined stripe laser which has the virtue of being very simple to fabricate. The area of current injection is defined by the opening in the oxide layer. This structure provides some degree of current confinement, but no carrier or photon confinement. Figure 5.12b illustrates a ridge laser which combines excellent current confinement with optical wave-guiding in the lateral direction. However, there is no lateral carrier confinement since the ridge etching process does not extend beyond the active region. Once injected into the active region carriers are free to diffuse away from the axis of symmetry directly under the ridge. The trade-off between current and photon confinement can be manipulated by changing the height of the etched ridge.

For reasons that will be made clear in Chapter 6, we have chosen to employ a different lateral current/carrier confinement technique in the fabrication of our *μ-Pillar* WGM lasers. The underlying physical mechanism is electronic compensation via hydrogen passivation [29-36] – *giving rise to the phrase hydrogenation.* It was shown previously that hydrogenation of impurities, both donors [29, 30] and acceptors [31, 32], in GaAs and AlGaAs reduces carrier concentration and produces highly resistive layers. If the hydrogenation process could be

"masked" (blocked) then a pattern of conducting and resistive material could be defined on the semiconductor chip, thereby establishing a pathway to the fabrication of narrow-stripe semiconductor laser diodes.

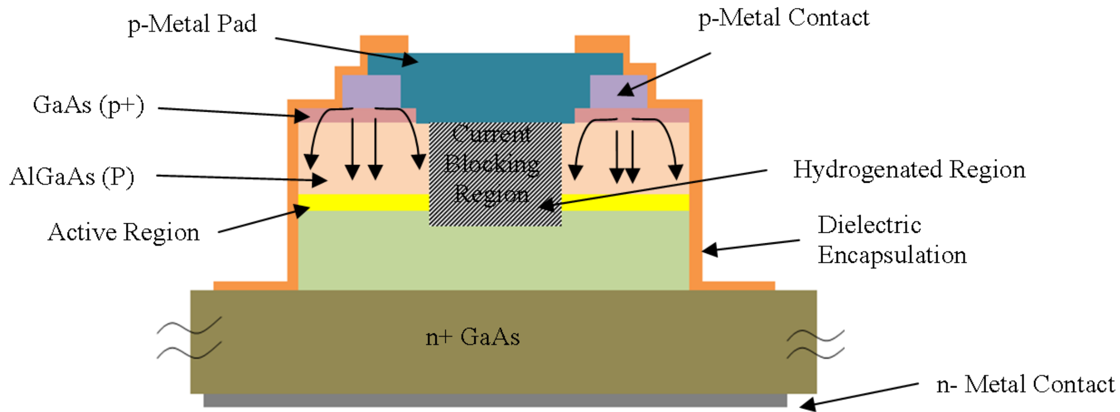

Figure 5.13: Cross-sectional view of WGM p-n junction laser with current blocking via hydrogenation within the central region of the structure (not to scale).

An AlGaAs/GaAs QW p-n junction laser – *designed specifically for WGM operation* – with current blocking via hydrogenation is shown in Figure 5.13. There are two distinct regions in the device: (1) current flows through the region directly under the p-metal contact thereby pumping the gain medium near the periphery of the optical cavity and (2) current flow is blocked in the central region of the device.

In the present work, hydrogenation was performed in a commercial PECVD system using ammonia (NH_3) as the source of hydrogen. A flow diagram for the process is presented in Fig. 5.14. The process flow starts by ramping up the temperature of the "chuck" (sample stage) to 250 °C at which juncture the sample is loaded into the PECVD chamber. Both the NH_3 flow and RF generator are turned on immediately thereafter in order to ignite the plasma.

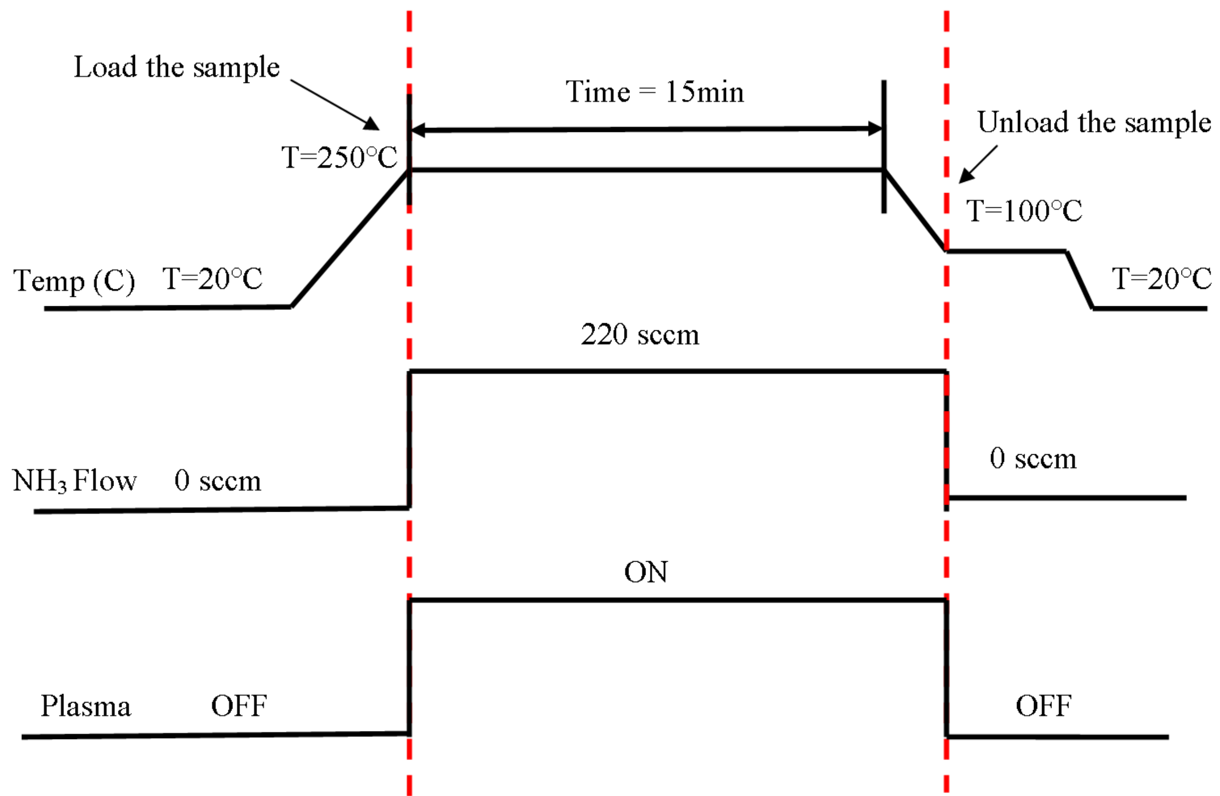

Figure 5.14: Flow diagram for implementation of hydrogenation process in the Trion Technologies PECVD system at Virginia Tech.

The sample is held under this condition throughout the "plasma exposure time" which can be defined by the user (τ_{plasma} = 15 minutes throughout the present work). The chuck temperature is then ramped down – *without changing the NH_3 flow or plasma settings* – until it reaches 100 °C. At this juncture, the NH_3 gas flow and RF generator are both turned off and the sample is unloaded from the PECVD chamber. The complete hydrogenation process recipe is given in Table C.3 of Appendix C.

It is critical that the NH_3 plasma remain "active" while the sample is cooling down (i.e., NH_3 gas flow and RF power during cool-down must be similar to those throughout τ_{plasma}). If instead the PECVD system returns to its "normal" cool-down state (high vacuum, no gas flow, no plasma) then hydrogen may *out-diffuse* from the sample, thereby "reversing" the hydrogenation process. We have direct evidence of such behavior, from our initial trial runs, in the form of I-V curves returning to their original (non-hydrogenated) state. As of this writing, however, we have not

confirmed via SIMS analysis that there is a corresponding reduction of hydrogen inside the sample.

It was demonstrated in Section 5.2 that thermal annealing at relatively high temperatures (300 to 500 °C) is necessary to form low-resistance ohmic contacts for p-n junction laser diodes. This contact annealing step is often done near the end of the overall process flow to avoid exposing the metal/semiconductor junctions to other aggressive conditions. If we were to follow this standard procedure then contact annealing would be performed after the hydrogenation step. This scenario raises the question – *how does the hydrogen profile inside the semiconductor change during thermal annealing?* It is possible that all of the hydrogen diffuses out of the sample and thus *reverses* the original hydrogenation step. We were sensitive to this issue because some earlier reports [32] claimed that electronic compensation via hydrogenation could not be sustained if contact annealing was done at temperatures above 250 °C (and we know that $T_{anneal} \leq 250$ °C is not adequate for ohmic contact formation).

Two p-n junction devices were fabricated in the manner depicted in Fig. 5.10, except that both samples were hydrogenated (HYD) before doing any other processing. The evolution of their I-V characteristics with contact annealing is shown in Fig. 5.15. For the as-deposited case, current flow is blocked until the applied (forward) voltage approaches 20 V at which point the I-V curve *snaps back* to a much lower voltage and the device begins to conduct a significant amount of current (mA range). After annealing at 400 °C for 1 minute, the I-V characteristic *under forward bias* is similar to the data shown in Fig. 5.11 (non-hydrogenated device). However, under reverse bias, this same device yields $I_{rev} \geq 1$ mA at applied voltages as low as 4 V.

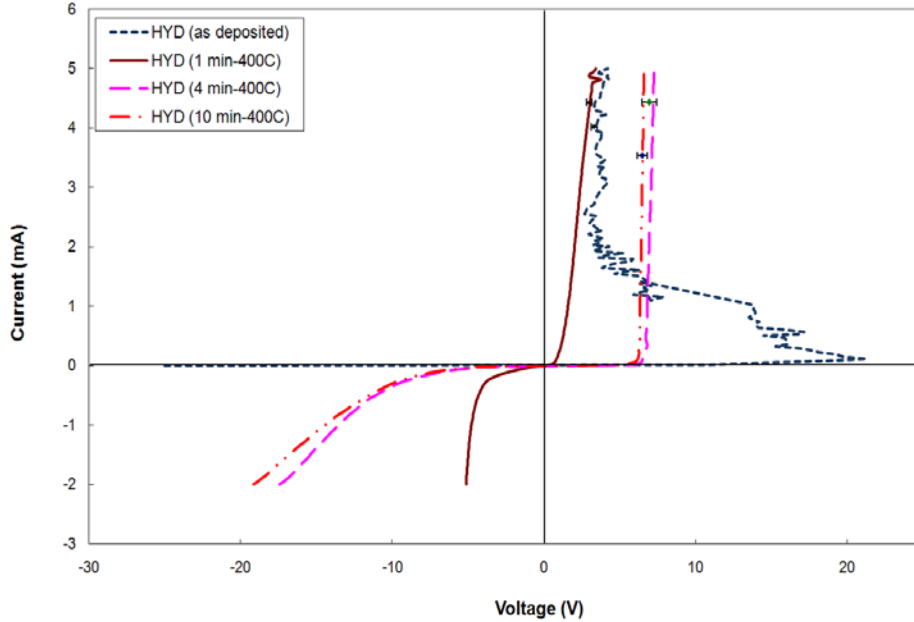

Figure 5.15: Electrical characteristics for *hydrogenated p-n junction test device* (HYD) with p-side and n-side metal contacts annealed at 400 °C. Annealing times range from $1 < \tau_{anneal} < 10$ minutes.

This performance is considerably worse than that observed for a non-hydrogenated device (e.g., I-V data in Fig. 5.11 exhibits normal reverse breakdown at about 18 V). Our ultimate goal of *current blocking* is finally realized in devices annealed for 4 or 10 minutes – *there is almost no current flow until the applied voltage exceeds 6 V (forward bias).* The data points with error bars show the variation in applied voltage at a specific current from 4 different devices on each of 2 separate samples. The small error bars suggest that our hydrogenation process is both uniform and reproducible.

Before hydrogen passivation of acceptors and/or donors can be applied to fabricate WGM lasers, we must be able to mask (block) electronic compensation in pre-selected areas of the AlGaAs/GaAs QW structure. The effectiveness of PECVD oxide as a mask against hydrogenation is evidenced by the I-V data plotted in Fig. 5.16.

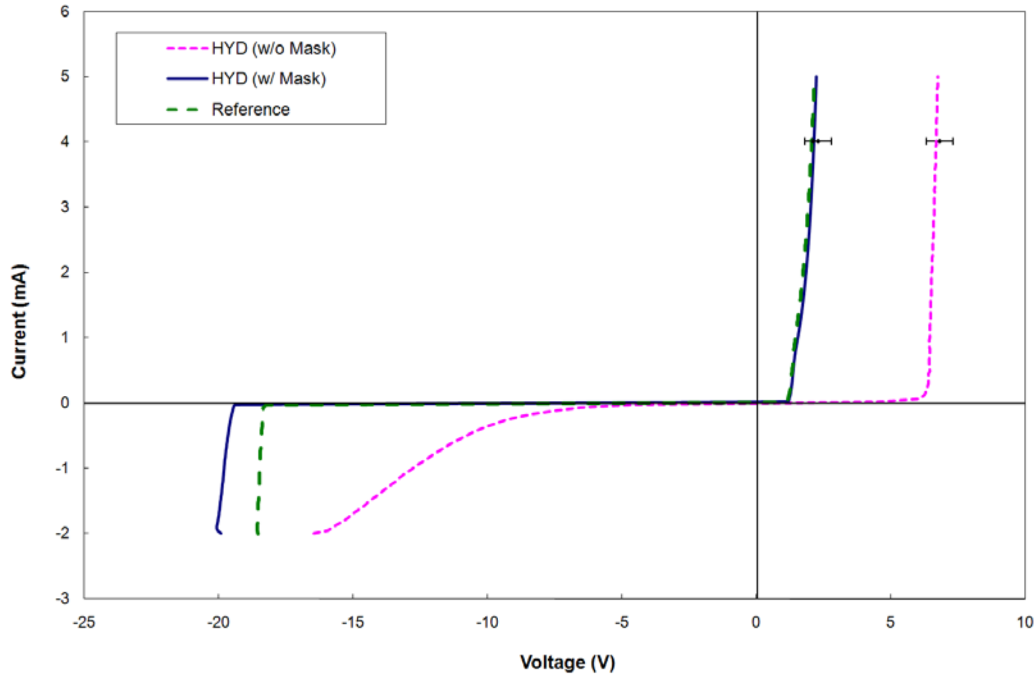

Figure 5.16: Electrical characteristics for three *p-n junction test devices* showing the effectiveness of PECVD oxide as a mask against hydrogenation. The metal contacts were annealed in forming gas at 400 °C for 5 min.

The first device labeled *"Reference"* was not exposed to hydrogenation, therefore its electrical behavior follows that shown in Fig. 5.11. The second device marked *"HYD w/o Mask"* was hydrogenated in the normal manner, thus its electrical behavior follows that shown in Fig. 5.15. The situation becomes more interesting when the *"HYD w/ Mask"* device is added to the discussion. This sample was encapsulated by a 200 nm thick layer of PECVD oxide *before* subjecting it to hydrogenation. After this faux hydrogenation step, the oxide layer was removed and the sample was reinserted into the standard process flow. It is obvious that the I-V curves for the *"Reference"* and *"HYD w/ Mask"* devices are nearly identical in all aspects (with the only exception being a *higher* reverse breakdown voltage for the *"HYD w/Mask"* case). We confirmed these initial findings by preparing a second set of samples (following the same exact process flow in each of the three distinct cases). The data points with error bars in Fig. 5.16 represent the results from measurements of 6 different devices on each of 3 samples from 2 distinct process runs. Once again, the small error bars suggest that our approach to masking the hydrogenation process is both uniform and reproducible.

We have recently begun to collaborate with Dr. Jerry Hunter of the *Nanoscale Characterization and Fabrication Lab* at Virginia Tech to learn more about the hydrogen "profile" (concentration and spatial distribution) inside our devices at various stages of processing. SIMS depth profiles are shown in Fig. 5.17 for two different samples. The aluminum profile marks transitions between the various $Al_xGa_{1-x}As$ alloy layers in the AlGaAs/GaAs QW heterostructure [20].

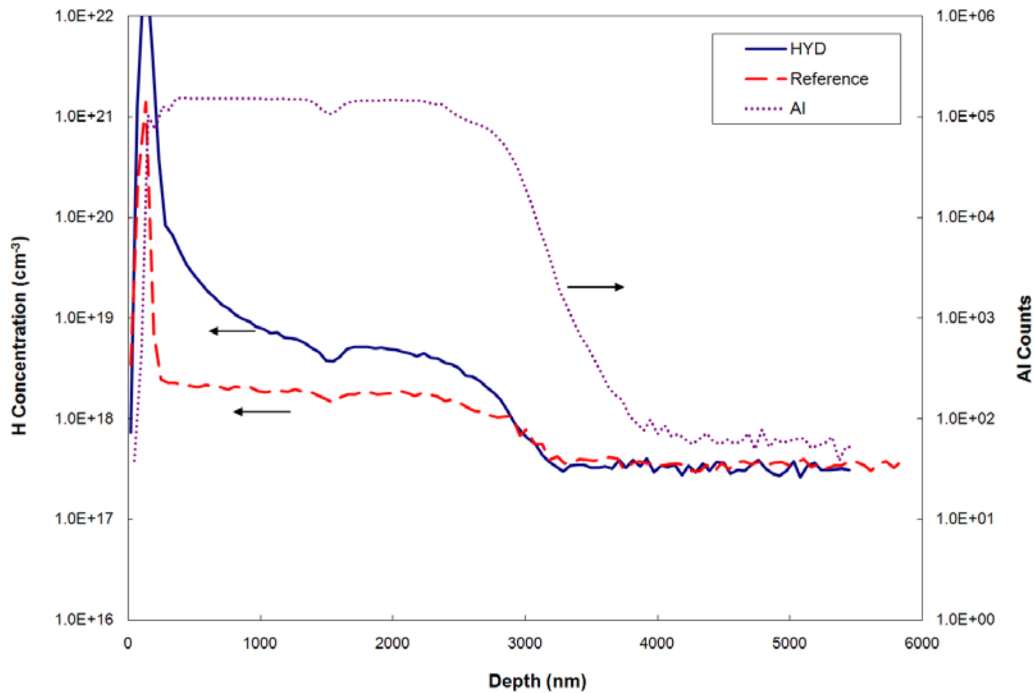

Figure 5.17: SIMS depth profiles of the hydrogen content in the reference sample (after annealing of metal contacts) and hydrogenated sample (before annealing of metal contacts).

The sample labeled *"Reference"* was not subjected to hydrogenation; however, it was annealed in forming gas (3.99% mixture of H_2 in argon) at 400 °C for 5 min to lower the ohmic contact resistance. The sample designated as *"HYD"* was hydrogenated using our standard conditions, but afterwards it was not exposed to any high temperature processing. It is notable that the hydrogen content in the *"HYD"* sample is higher than that found in the *"Reference"* sample. Further work is required to refine our understanding of the hydrogenation process itself and the impact of post-hydrogenation thermal annealing on the basic mechanisms responsible for electronic compensation.

References

[1] This lot of GaAs substrates was manufactured by Freiberger Compound Materials GmbH (e-mail: info@fcm-germany.com).

[2] L. A. Coldren, K. Iga, B. I. Miller and J. A. Rentchler, "GaInAsP/InP stripe-geometry laser with a reactive-ion-etched facet," *Appl. Phys. Lett*., vol. 37, p 681-683 (1980).

[3] G. Smolinsky, R. P. H. Chang and T. M. Mayer, "Plasma etching of III-V compound semiconductor materials and their oxides," *J. Vac. Sci & Technol.*, vol 18, pp. 12-16 (1981).

[4] R. A. Barker, T. M. Mayer and R. H. Burton, "Surface composition and etching of III-V semiconductors in Cl_2 ion beams," *Appl. Phys. Lett*., vol.40, pp. 583-586 (1982).

[5] P. G. Glöersen, "Ion-Beam etching," *J. Vac. Sci. & Technol.,* vol 12, pp. 28-35 (1975).

[6] E. Hu and R. Howard, "Reactive Ion Etching of GaAs in a Chlorine Plasma," *J. Vac. Sci. Technol.*, vol. B2, pp. 85-88 (1984)

[7] H. Nagasaka, H. Okano, and N. Motegi, *Proc. Symp. on Dry Process,* (The Institute of Electrical Engineers of Japan, Tokyo, 1982) p. 79.

[8] H. Yamada, H. Ito, and H. Inaba, *Proc. Symp. on Dry Process* (The Institute of Electrical Engineers of Japan, Tokyo, 1983) p.73.

[9] R. G. Poulsen, H. Nentwich, and S. Ingrey: Proc. Int. Electron Devices Meeting, Washington, D. C., 1976 (Electron Device Society of IEEE, New York, 1976) p. 205.

[10] K. Tokunaga, F. C. Redeker, D. A. Danner, and D. W. Hess, "Comparison of Aluminum Etch Rates in Carbon Tetrachloride and Boron Trichloride Plasmas," *J. Electrochem. Soc.,* vol. 128, pp. 851-855 (1981).

[11] H. Tamura and H. Kurihara, "GaAs and GaAlAs Reactive Ion Etching in BCl3-Cl2 Mixture," *Jpn. J. Appl. Phys.,* vol. 23, pp L731-L733 (1984).

[12] M. W. Geis, G. A. Lincoln, N. E. Efrernow, and W. J. Piacentini, “A novel anisotropic dry etching technique,” *J. Vac. Sci. Technol.,* vol. 19, pp. 1390-1393 (1981).

[13] J. D. Chinn, I. Adesida, and E. D. Wolf, “Chemically assisted ion beam etching for submicron structures,” *J. Vac. Sci. Technol. B,* vol. 1, pp. 1028-1032 (1983).

[14] A. Behfar-Rad, S. S. Wong, J. M. Ballantyne, B. A. Soltz, and C. M. Harding, “Rectangular and L-shaped GaAs/AlGaAs lasers with very high quality etched facets,” *Appl. Phys. Lett*., vol. 54, pp. 493-495 (1989).

[15] Note that using photoresist *alone* as the mask layer eliminates one pattern transfer step and thereby simplifies the overall process.

[16] This highly specialized photoresist was manufactured by AZ Electronic Materials.

[17] This photomask was manufactured by Advance Reproduction Corporation, North Andover, MA 01845 (http://www.advancerepro.com).

[18] This highly conductive thermal paste is known as “Cool-Grease” (part # 7018). It is manufactured by AI Technology, Inc. (e-mail: ait@aitechnology.com).

[19] M. S. Stern, P. C. Kendal, R. C. Hewson-Browne, P. N. Robson, D. A. Quinney, “Scattering loss from rough sidewalls in semiconductor rib waveguides,” *Electron. Lett.,* vol. 25, pp 1231-1232 (1989).

[20] The laser material used to fabricate this device is identical to that described in Chapter 3 of this manuscript.

[21] For pedagogical convenience, we assume that the optical-mode-to-electronic-gain volume ratio or overall *confinement factor* can be separated into three orthogonal components: longitudinal (Γ_{long}), transverse (Γ_{trans}), and lateral (Γ_{lat}).

[22] Along the longitudinal direction – *parallel to the direction of electromagnetic wave propagation* – the overlap between the electron gain and the optical mode is close to unity for conventional Fabry-Perot edge-emitting lasers.

[23] The assumption that $\Gamma_{long} = 1$ is not appropriate in the case of vertical-cavity surface emitting lasers (VCSELs); however, a full analysis of this situation is beyond the scope of this thesis.

[24] J. C. Dyment, "Hermite-Gaussian Mode Patterns in GaAs Junction Lasers," *Appl. Phys. Lett.,* vol. 10, pp 84-86 (1967).

[25] T. Tsukada, H. Nakashima, J. Umeda, S. Nakamura, N. Chinone, R. Ito, and O. Nakada, "Very-Low-Current Operation of Mesa-Stripe-Geometry Double-Heterostructure Injection Lasers," Appl. Phys. Lett., vol. 20, pp 344-345 (1972).

[26] J. C. Dyment, L. A. D'Asaro, J. C. North, B. I. Miller, and J. E. Ripper, "Proton-bombardment formation of stripe-geometry heterostructure laser for 300K CW operation," *Proc. IEEE(Lett.)*, vol. 60, pp.726-728 (1972).

[27] T. Tsukada, "GaAs-$Ga_{1-x}Al_xAs$ buried-heterostructure injection lasers," *J. Appl. Phys,* vol. 45, pp. 4899-4906 (1974).

[28] R. D. Burnham and D. R. Scifres, "Etched buried heterostructure GaAs/GaAlAs injection lasers," *Appl. Phys. Lett.*, vol. 27, pp. 510-511 (1975).

[29] S. J. Pearton, W.C. Dautremount-Smith, J. Chevallier, C. W. Tu, and K. D. Cummings, "Hydrogenation of shallow-donor levels in GaAs," *J. Appl. Phys.*, vol. 59, pp. 2821-2827 (1986).

[30] N. Pan, B. Lee, S. S. Bose, M. H. Kim, J. S. Hughes, G. E. Stillman, Ken-ichi Arai, and Y. Nashimoto, "Si donor neutralization in high-purity GaAs", *Appl. Phys. Lett.*, vol. 50, pp. 1832-1834 (1987).

[31] N. M. Johnson, R. D. Burnham, R. A. Street, and R. L. Thornton, "Hydrogen passivation of shallow-acceptor impurities in p-type GaAs," *Phys. Rev. B,* vol. 33, pp. 1102-1105 (1986).

[32] N. Pan, S. S. Bose, M. H. Kim, G. E. Stillman, F. Chambers, G. Devane, C. R. Ito, and M. Feng, “Hydrogen passivation of C acceptors in high-purity GaAs,” *Appl. Phys. Lett.*, vol. 51, pp. 596-598 (1987).

[33] J. Chevallier, W. C. Dautremont-Smith, C. W. Tu, and S. J. Pearton, “Donor neutralization in GaAs(Si) by atomic hydrogen,” *Appl. Phys. Lett.*, vol. 47, pp. 108-110 (1985).

[34] A. Jalil, J. Chevallier, R. Azoulay, and A. Mircea, “Electron mobility studies of the donor neutralization by atomic hydrogen in GaAs doped with silicon,” *J. Appl. Phys.*, vol. 59. pp. 3774-3777 (1986).

[35] W. C. Dautremont-Smith, J. C. Nabity, V. Swaminathan, Michael Stavola, J. Chevallier, C. W. Tu, and S. J. Pearton, “Passivation of deep level defects in molecular beam epitaxial GaAs by hydrogen plasma exposure,” *Appl. Phys. Lett.*, vol. 49, pp.1098-1100 (1986).

[36] Jorg Weber, S. J. Pearton, and W. C. Dautremonth-Smith, “Photoluminescence study of the shallow donor neutralization in GaAs(Si) by atomic hydrogen,” *Appl. Phys. Lett*., vol. 49, pp.1181-1183 (1986).

6. DESIGN CONSIDERATIONS FOR WGM LASERS

The performance of a WGM cavity is usually described in terms of its capacity to store energy. Obviously, this capacity is constrained by processes that dissipate energy from the cavity. These loss processes can be classified into internal (material, leakage, scattering) and external (coupling). The storage capacities and loss effects of various cavity types can be quantified by their *cavity quality factor* or Q [1-5]. The most basic definition of cavity Q is that it represents the number of cycles the optical field undergoes before its energy decays to a value 1/e times its original value. This is nothing more than saying that the energy within the cavity decays as $e^{-\omega t/Q}$ which gives rise to the differential form of Eq. 6.1, where U is the stored energy and $P_d = -\frac{dU}{dt}$ is the dissipated power.

$$\frac{dU}{dt} = -\frac{\omega}{Q}U \qquad (6.1)$$

Any real cavity must suffer from optical losses and thus its corresponding electromagnetic modes must have a finite line-width in frequency (or wavelength) space. This frequency line-width $\Delta\omega$ represents the ratio of dissipated power to stored energy for the cavity. Therefore, the quality factor of a *real* cavity is most conveniently defined as $Q = \omega/\Delta\omega$ where ω is the center frequency of the mode. An alternative way of stating the same thing is $Q = \omega\tau_{ph}$ where τ_{ph} is the average time a photon stays remains in existence before being absorbed within or coupled outside of the cavity. This quantity is often referred to as the *photon lifetime* in the cavity. It is sometimes convenient to define Q in terms of the photon decay length L_{ph} which is proportional to τ_{ph}. This alternative definition is presented in Eq. 6.2, where λ is the center wavelength of the mode and n_g is its group index of refraction.

$$Q = \frac{2\pi n_g L_{ph}}{\lambda} \qquad (6.2)$$

An inverse decay length $\alpha = L_{ph}^{-1}$ is often quoted in the literature (instead of L_{ph} itself). This is particularly true for device structures such as optical waveguides in which loss per unit length is a common metric (sometimes given in units of cm^{-1} and other times in dB/cm). This is also true for material absorption losses. For comparison purposes, we can use Eq. 6.2 to convert optical loss values reported by others (in cm^{-1}) into an equivalent value of cavity Q.

$$\frac{1}{Q} = -\frac{1}{\omega U}\frac{dU}{dt} \tag{6.3}$$

When considering how individual loss mechanisms contribute to the overall Q of the cavity, it is beneficial to rearrange Eq. 6.1 as shown above in Eq. 6.3. Within this framework, the total quality factor [6, 7] for any real cavity is given by

$$\begin{aligned}\frac{1}{Q_{tot}} &= \frac{P_{tot}}{\omega U} = \frac{P_{mat}}{\omega U} + \frac{P_{scat}}{\omega U} + \frac{P_{rad}}{\omega U} + \frac{P_{coup}}{\omega U} \\ &= \underbrace{\frac{1}{Q_{mat}} + \frac{1}{Q_{scat}} + \frac{1}{Q_{rad}}}_{Intrinsic_Quality_Factor} + \underbrace{\frac{1}{Q_{coup}}}_{External_Quality_factor}\end{aligned} \tag{6.4}$$

where Q_{mat} refers to free carrier and band-to-band absorption losses, Q_{scat} accounts for scattering from imperfections at the cavity sidewalls, Q_{rad} represents the diffraction loss that accompanies *TIR* at curved boundaries, and Q_{coup} describes the impact of electromagnetic mode mismatch at the output coupler on the efficiency of light extraction from the cavity.

The Q factor of micro-resonators can be extremely high (> 10^8) because of the strong confinement of photons within as small modal volume [8, 9], thus making this cavity design attractive for laser devices [10]. The cavity Q of a WGM laser should *increase* in response to (1) a *decrease* in material absorption, (2) an *increase* in refractive index contrast between the cavity material and its surroundings, (3) a *reduction* of surface roughness at the cavity boundary [11], and (3) an *increase* in the cavity diameter [1]. Measured values of Q for micro-ring and micro-

disk resonators typically do not exceed 10^5. Others have shown that semiconductor micro-ring resonators with d_{cavity} = 10 μm and vertical coupling to a bus waveguide have $Q = 2.5\times10^3$ [12]. An "unloaded" Q on the order of 10^5 was demonstrated in 80 μm diameter micro-disk resonators [13]. Very small micro-disk semiconductor resonators with $d_{cavity} \leq 5$ μm exhibit Q values in the range of 10^4 [14, 15].

The material structure for a WGM *μ-Pillar* laser is identical to that of an *EE* laser, but the geometry of the optical cavity is very different. As a consequence, the relationships between the input variables (material properties and device design parameters) and the output quantities (WGM laser performance) is likely to differ *at least in detail* from the usual formulation for *EE* lasers. A cross-sectional drawing of our WGM laser is shown in Fig. 6.1 for illustration purposes. This schematic represents the state of the device after completion of the entire fabrication process.

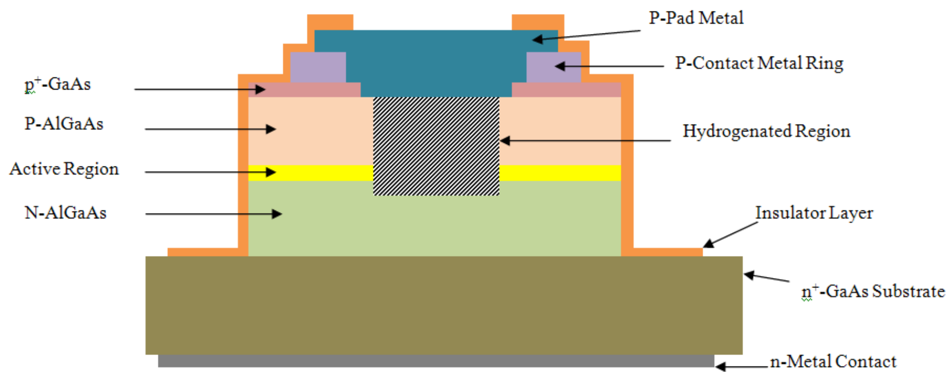

Figure 6.1: Side-view drawing of WGM laser structure after completing the fabrication process.

It may prove useful to visualize the operating characteristics of WGM lasers within the context of equations originally derived for *EE* devices. Toward this end, we restate below with only minor changes two important equations from Chapter 4. First, we convert α_m of Eq. 4.6 to α_{useful} and rewrite it below as Eq. 6.5. Then, we excerpt an important piece of Eq. 4.1, make the same

substitution, and restate it below as Eq. 6.6. The new quantity F_{opt} is a dimensionless parameter sometimes referred to as optical extraction efficiency.

$$I_{th} = WL\frac{J_o}{\eta_i}\exp\left(\frac{\langle\alpha_i\rangle + \alpha_{useful}}{\Gamma G_o} - 1\right) + I_{leak} \qquad (6.5)$$

$$F_{opt} = \left(\frac{\alpha_{useful}}{\alpha_{useful} + \langle\alpha_i\rangle}\right) \qquad (6.6)$$

Now let's consider a special case in which the WGM laser has perfect cylindrical symmetry – i.e., there is no output coupler of any kind connected to the *μ-Disk* or *μ-Pillar* cavity. According to Eq. 6.4 the remain losses are attributable to diffraction (Q_{rad}), which provides the laser output power, and material absorption (Q_{mat}) and scattering mechanisms (Q_{scat}), neither of which give useful light output. Following the arguments made in Chapter 4, it is reasonable to expect that I_{th} for a WGM laser can be made as low as possible by decreasing the *total* optical loss ($\langle\alpha_i\rangle$ + α_{useful}), reducing the area of the "pumped" laser stripe (represented by $W{\cdot}L$ in Eq. 6.5), and eliminating the leakage current. In the present context, the scattering loss component of $\langle\alpha_i\rangle$ has been reduced by optimizing the ICP etching process (i.e., forming the smoothest possible cavity sidewalls). Further reduction in this residual level of light scattering can be achieved by coating the cavity sidewall with a thin dielectric film. Both of these issues are considered in more detail in Section 6.2. This focus on lowering $\langle\alpha_i\rangle$ has the additional benefit of bringing F_{opt} very close to unity if we can make $\langle\alpha_i\rangle << \alpha_{useful}$.

Reductions in laser stripe width and I_{leak} can both be accomplished by using our new hydrogenation technique. This matter is discussed at some length in Section 6.3. In closing, we mention that one very important factor that differentiates WGM and *EE* lasers is not reflected explicitly in Eq. 6.5 and 6.6. That is, the difference in the optical confinement factor $\Gamma_{\text{in-plane}}$ within the 2-D plane of the active region. Owing to the nature of WGMs, any electrical pumping

that occurs outside a narrow stripe close to the periphery of the cavity only adds to the amount of total current necessary to reach threshold without providing any real benefit. Once again, this issue can be addressed using our new method of current confinement as described in Section 6.3.

6.1. Optical Losses via Diffraction

The cavity Q for a WGM laser is ultimately limited by the diffraction losses associated with the particular lasing modes [16, 17]. Following the discussion and analysis presented in Reference [18], the relationship between a WGM of order M and the optical transmission coefficient T_M is given by

$$T_M = e^{\left(-a_{oM}\left(\frac{2}{3}\right)\cos^3(\theta(M))\right)} \qquad (6.7)$$

where $\theta(M) = \frac{(M-1)\pi}{2M}$ is the glancing angle at which the optical ray impinges on the cavity sidewall and $a_{oM} = \frac{2\pi R n_{eff}}{\lambda}$. For large M, the cavity Q defined by $U_M(t) = U_o e^{(-\omega \cdot t/Q)}$ can be expressed as $Q_M = \pi / T_M$ which leads to

$$Q_M = \pi \cdot e^{\left(\left(\frac{2}{3}\right)a_{oM}\cos^3\theta(M)\right)} \qquad (6.8)$$

Let us consider the GaN *μ-Disk* resonator mentioned in Chapter 2 with R_0 = 2.5 μm, n = 2.65, and λ = 375 nm. By applying Eq. 6.8 to evaluate the two WGM solutions of Fig. 2.11, we find Q values in excess of 10^{13}! There is an enormous discrepancy between this diffraction limited Q and the much smaller values found experimentally for semiconductor micro-cavity resonators (Q ≤ 10^5). This demonstrates the crucial roles played by careful material structure design and device process optimization in the realization of high-performance WGM lasers.

6.2. Optical Losses via Scattering

In well designed WGM lasers, the peak of the optical wave should travel very close to the etched cavity sidewall. Thus optical losses can be considerable because of scattering from wall imperfections and material degradation during etching. The importance of this issue is demonstrated by the data presented in Fig. 6.2. In this particular case, the semiconductor material is a 2 μm thick GaN layer grown by MOCVD on a sapphire substrate. It was fashioned by dry etching into *μ-Pillar* cavities with R_0 = 250 μm. The SEM image on the upper right side of Fig. 6.2 depicts a sample prepared in 1997 at Yale University using a home-built *RIE* system with a non-optimized Cl_2/BCl_3 process. In contrast, the SEM image on the upper left side of Fig. 6.2 exemplifies a high-quality *μ-Pillar* cavity. It was prepared at Xerox PARC in 2003 via chemically assisted ion beam etching (CAIBE) using chlorine gas chemistry.

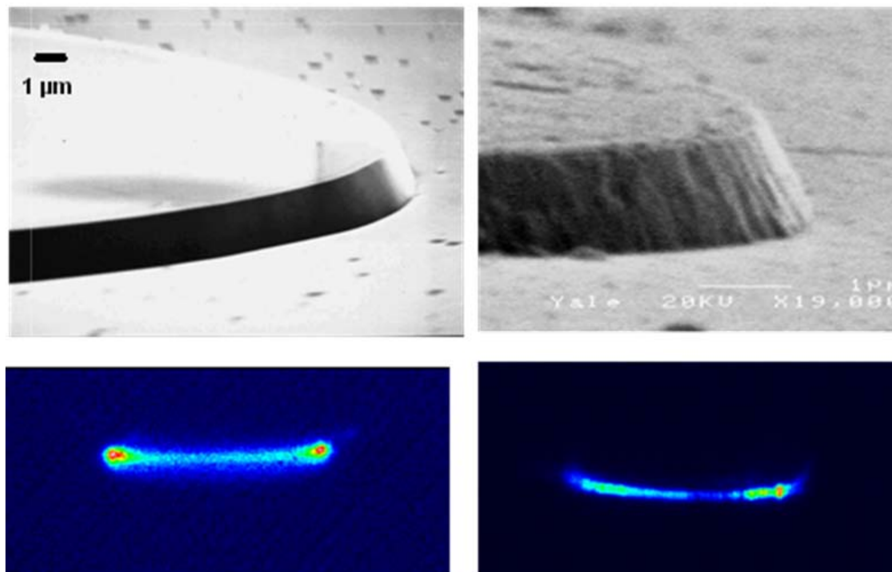

Figure 6.2: SEM images (upper panels) and CCD photographs (lower panels) of two GaN *μ-Pillar* cavities fabricated by dry etching.

The two photographs on the bottom side of Fig. 6.2 are near-field images of the sidewalls of these two *μ-Pillar* cavities when being driven under high-level excitation. The stimulated emission from the smooth GaN cavity (on the left) is localized at the edges of the *μ-Pillar* where the diffraction losses are high. In contrast, the near field image for the rough GaN cavity (right

hand side) is very irregular and it does not show the expected intensity maxima at the leftmost and rightmost extremities.

Of course, the material of interest in the present work is an AlGaAs/GaAs QW structure (see Section 3.1 of Chapter 3). We demonstrated the ability to produce smooth cavity sidewalls via ICP etching in Fig. 5.6b of Chapter 5. As small slice of that SEM image is shown again on the leftmost side of Fig. 6.3. We attempted to quantify the level of residual roughness on this semiconductor sidewall by using an atomic-force microscope (AFM). However, we did not have the proper tip fixtures to record data from the actual sidewall itself so instead we analyzed the planar (etched) surface of the same GaAs sample. This AFM 3-D image is shown on the rightmost side of Fig. 6.3.

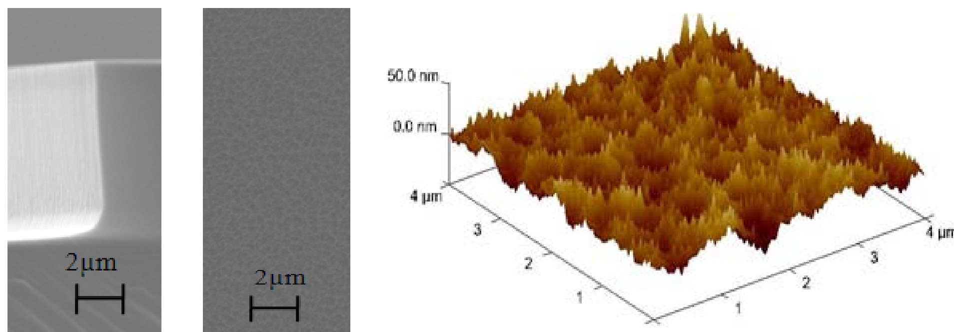

Figure 6.3: SEM image of GaAs sidewall (left) and planar surface (middle) prepared by ICP etching. The AFM image (right) provides an estimate of the actual surface roughness with $R_a = 6.02$ nm.

The accepted metric for surface roughness is a parameter known as R_a and our etched GaAs surface has a value of $R_a = 6.02$ nm. The corresponding SEM image for this very same planar (etched) surface is shown in the middle panel of Fig. 6.3. The two SEM images were recorded under identical conditions. Note that the "apparent roughness" is very similar in these two cases; therefore, we assume the actual cavity sidewall roughness is on the order of 6.02 nm. This compares favorably with the target of $R_a \leq \lambda/30$ ($\lambda = 795$ nm) so as to minimize the impact of optical scattering on the overall Q of the cavity.

A significant reduction in waveguide propagation loss has been demonstrated for AlGaAs/GaAs QW structures using a process known as "oxidation smoothing" via wet oxidation [19]. It was also shown by these workers that significant smoothing of surface roughness (down to 5 nm) can be attained with O_2-enhanced wet oxidation [20]. Equation 6.9 shows that the scattering loss is directly proportional to the refractive index steps at the interfaces between the semiconductor and air [21]. Coating the AlGaAs/GaAs cavity sidewalls with a thin dielectric film such as Al_2O_3 would reduce the value of Δn between the semiconductor and its surroundings, and therefore, should lead to a reduction in scattering loss as given by

$$\alpha_{scat} \propto \sum (\Delta n_i^2)^2 \frac{|E(x_i)|^2}{\int |E(x_i)|^2 dx} \qquad (6.9)$$

where α_{scat} is the scattering loss, Δn_i^2 is difference of the squares of the refractive indices at the ith interface, and $E(x_i)$ is the electric field at the interface. However, this wet oxidation approach shows a strong preference for high Al-content III-V alloys [22, 23]. Given that the Al mole fraction changes from x = 0.85 in the cladding layers to x = 0.25 in the OCL, we were concerned that such an approach would create a spatially non-uniform dielectric layer along the growth direction. So, we used the PECVD method instead to deposit SiN_y and SiO_x films on our WGM laser structures. Complete PECVD process recipes are presented in Appendix C (see Tables C.6 and C.7).

6.3. Electrical Losses via Current Leakage

The term leakage current is used herein to denote two different physical mechanisms [24]: (1) lateral current spreading in the narrow-band-gap p+ capping layer and the wide-band-gap p-type upper cladding layer and (2) lateral diffusion of carriers in the OCL and QW layers. Several different laser designs have been developed to address this problem. These device structures can be classified as gain-guided lasers or weak/strong index guided lasers. The gain guided structure shown in Fig. 6.4 uses a dielectric layer for current blocking. The current is injected through the

opening in the dielectric which produces gain in that region and hence the lasing mode is confined to that region.

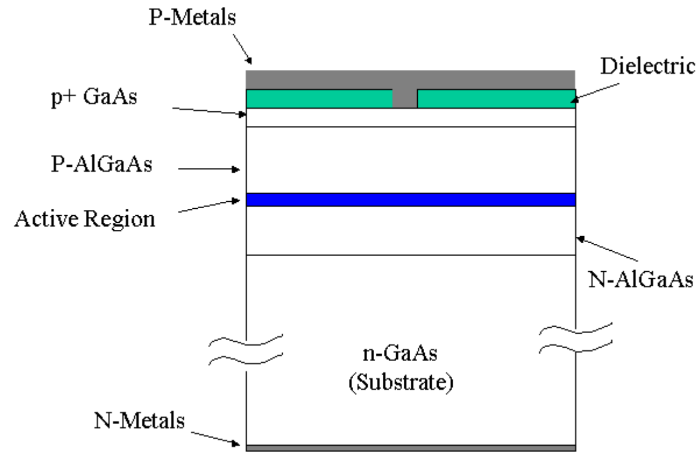

Figure 6.4: Schematic of a gain guided laser.

The weak index guided structure shown in Fig. 6.5 has a ridge etched into the upper cladding layer plus a dielectric coating to insulate the exposed cladding material from the p-side metal contact. The current is injected in the region of the ridge, and the optical mode overlaps the dielectric material (which has a low index of refraction) in the sidewalls of the ridge. This results in weak index guiding but better current confinement than the gain guided structure.

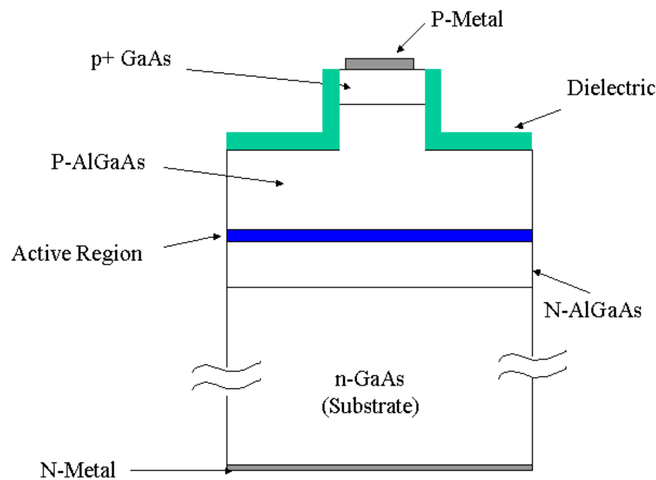

Figure 6.5: Schematic of an index guided laser.

Lateral current spreading can be eliminated altogether by etching down to the interface between the upper cladding layer and the OCL [25, 26]. However, in this case, the lateral diffusion of carriers outside the active laser stripe remains as a significant problem [27, 28]. The strong index guided laser is a variant of the index guided structure with the ridge etched all the way through the p-n junction. This configuration provides strong electrical and optical lateral confinement but suffers from high surface recombination.

The experimental findings reported in Section 5.3 of Chapter 5 demonstrate that our hydrogenation process can be applied successfully to block the flow of current from the p-side metal contact to the active region of the laser structure. This new process technology is the cornerstone of our effort to fabricate *narrow-ring* WGM lasers. The objective is to prevent current flow in regions of the device not in close proximity to the cavity sidewalls where the high-Q WGM have their maximum electromagnetic field intensity. In this regard there are clear benefits to de-coupling the hydrogenation process from the metal annealing process. One such advantage is providing the flexibility for optimizing each process separately. Another benefit is providing the option of performing the hydrogenation as the last step in the fabrication process. In this case, the hydrogen can be diffused into the sample from the exposed semiconductor side-wall so as to move the active laser stripe away from the cavity edge. This may prove useful in controlling lateral carrier diffusion within the QW active region driven by surface recombination. In order to decouple the hydrogenation process from the metal contact annealing step it is essential that our low-resistance ohmic contacts survive the thermal stresses associated with the PECVD oxide deposition (350 °C) and hydrogenation processes (250 °C). Both of these conditions have been met at the current stage of process development.

6.4. Electrical Losses via Carrier Recombination

Others workers have shown that electrical characteristics of semiconductor lasers can be improved by coating the exposed surfaces near the p-n junction with an insulating layer of Si_3N_4 or SiO_2 [29]. The combination of AlGaAs/GaAs materials and small-diameter *μ-Disk* cavities with high *surface-to-volume* ratios is particularly troublesome because the high-*Q* laser modes

are confined close to the disk edge where carrier recombination via surface states may dominate over spontaneous emission which is necessary as a "seed" for stimulated emission and lasing [30, 31]. The surface recombination velocity is considerably smaller in the InGaAs/InP material system and as such this issue is somewhat less problematic. Nevertheless, even in this favorable situation, it is likely that non-radiative surface recombination will ultimately limit device performance.

Equation 6.10 shows that several mechanisms may contribute to the total current required to reach the threshold for laser operation, where V_{ol} is the volume of the active region and N_{th} is the threshold carrier density [32]. The objective then is to minimize all carrier recombination mechanisms other than spontaneous emission (middle term in Eq. 6.10) so as to make the experimental I_{th} as low as possible when the carrier density reaches the value of N_{th} necessary for lasing. The cubic term represents Auger recombination which is predetermined by the choice of material system, so it does not warrant further discussion here. The linear term is attributable to leakage current and surface recombination current both of which have been targeted in our laser fabrication process.

$$I_{th} = \left(\frac{q_e V_{ol}}{\eta_i}\right)\left(AN_{th} + BN_{th}^{2} + CN_{th}^{3}\right) \qquad (6.10)$$

During device processing, the GaAs surface is exposed to oxidizing media, i.e., moisture in air, which results in the formation of native oxides, such as Ga_2O_3 and As_2O_3, on the surface of the GaAs sample. There is evidence, in literature, that the source of the poor electronic properties arises because As_2O_3 is unstable in the presence of GaAs and reacts to form elemental As according to [33-35]

$$As_2O_3 + 2GaAs \rightarrow 4As + Ga_2O_3 \qquad (6.11)$$

The formation of elemental As creates surface states near the middle of the band-gap which pin the Fermi level and thereby enhance the non-radiative surface recombination [33, 35-37],

whereas, Ga_2O_3 is a wide bandgap non-conductive species, and it should not produce surface leakage [35]. Literature shows that removal of As from the surface of GaAs devices improves the performance of such devices. For example, the work of Chang *et al.* [38] on GaAs MOS devices showed that the poor performance of these devices was due to the existence of interface states as a result of the formation of an arsenic layer at the semiconductor-oxide interface.

Therefore, it is important to eliminate or reduce arsenic-bearing oxides from the surface of GaAs and AlGaAs compounds. Wet chemical treatments such as sulfide treatment of the GaAs surface have been effective in reducing surface state density and chemically passivating the surface [39, 40]. However, this sulfide solution is sensitive to temperature and it also etches the GaAs semiconductor. Therefore, process reproducibility is a challenge and it is essential that the properties of the sulfide solution be carefully monitored. It has been shown by several other groups [35, 41-46] that exposing native oxide contaminated GaAs to hydrogen plasmas (H_2, NH_3, H_2S) reduces the amount of elemental arsenic and arsenic oxide on the surface according to

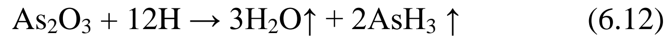

$$As_2O_3 + 12H \rightarrow 3H_2O\uparrow + 2AsH_3\uparrow \qquad (6.12)$$

$$As + 3H \rightarrow AsH_3\uparrow \qquad (6.13)$$

These chemical reactions occur at significant rates even at room temperature. This processing method also removes Ga_2O_3 by the following reaction [35]

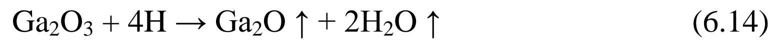

$$Ga_2O_3 + 4H \rightarrow Ga_2O\uparrow + 2H_2O\uparrow \qquad (6.14)$$

Several techniques have been introduced to determine the quality of various forms of GaAs surface passivation. These methods have been designed to acquire and interpret data regarding physical quantities such as photoluminescence intensity [47], Schottky barrier height [48], interface state density [49], surface recombination velocity [31], and surface sheet resistivity [50]. Though much progress has been made on understanding the oxide contaminated GaAs surface [51-53], we are not aware of any comprehensive studies of the impact on electrical and

optical performance of *μ-Disk* or *μ-Pillar* lasers. In our WGM lasers, we utilize surface treatment scheme that involves two steps: (1) electrical passivation of the device surface by exposing it to an NH_3 plasma discharge followed by (2) optical modification of the cavity sidewall via deposition of a thin coating of amorphous silicon nitride. Our device fabrication procedures were specifically designed to accommodate these "passivation" steps at the optimum juncture in the overall process flow.

6.5. Output Coupling from WGM Lasers

The isotropic radiation pattern of light emitted by *μ-Disk* or *μ-Pillar* lasers greatly limits their practical usefulness. As a result, many research groups have attempted to achieve directional light emission or "out-coupling" by making perturbing the pure cylindrical symmetry of such dielectric cavities [54-57]. We briefly review some of this prior work in Sections 6.5.1 and 6.5.2, so as to put into context our decision to focus on WGM-based spiral lasers. We then discuss in Section 6.5.3 our specific laser designs and make connections back to the device fabrication issues studied throughout this body of work.

6.5.1. Output Coupling via Y-Junctions

The earliest reports of directional coupling from conventional ring lasers made use of various geometrical configurations such as Y-junction couplers [58-60] and multi-mode interference couplers [61, 62]. In general, there was an effort to avoid exposing the p-n junction to air so lateral wave guiding was enabled via a shallow ridge like structure. The index of refraction difference between the channel and the surrounding medium was not very large and thus the radius of curvature was kept relatively large. An example of one such ring laser with a Y-junction output coupler is shown in Fig. 6.6. This form of output coupling seems to have a significant negative impact on laser performance as evidenced by reported L-I slope efficiencies in the range of 2 to 3% [29, 59, 60]. With further optimization of the coupling geometry [64], the value of η_{slope} was increased to 5% which is still unacceptable for most applications.

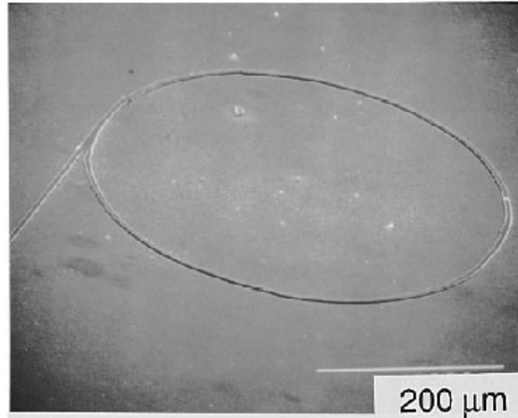

Figure 6.6: SEM image of a semiconductor ring laser with an integrated Y-junction out-coupler (Reprinted with permission from M. C. Shih *et. al.*, Appl. Phys. Lett., vol. 66, pp. 2608-2610 (1995). Copyright [1995], American Institute of Physics).

6.5.2. Output Coupling via Evanescent Waves

The most heavily investigated scheme for out-coupling light from high-Q dielectric resonators makes use of evanescent waves that penetrate a short distance into the surrounding medium [65, 66]. There are two ways to couple light from the bus-waveguide to the microring or microdisk using evanescent-field couplers. One approach relies on lateral coupling as illustrated in Fig. 6.7a. In this case, the bus-waveguide is in the same plane as the micro-ring cavity and hence the dielectric material must be identical in the two components [67, 68]. The evanescent wave intensity decays exponentially outside the dielectric medium, so the coupling efficiency depends critically on the width of the gap separating the two structures. In order to achieve any reasonable level of out-coupling, the gap width should be of sub-micron dimensions. As a consequence, it is necessary to use electron-beam lithography to pattern the masking layer in preparation for dry etching [69. 70]. In addition, this same physical limitation makes the design very sensitive to small variations in the lithography and etching processes. Finally, it is not at all straightforward to construct separate active and passive regions in various locations since the material that constitutes the optical core is the same everywhere.

The alternative method makes use of evanescent coupling along the vertical dimension as depicted in Fig. 6.7b [71, 72]. Vertical coupling allows for two optical cores with the ring and

bus made from different materials. Therefore, ring level optical core can contain the active region for controlling gain or loss while the bus level can have a passive core for low loss transport [71, 72]. In this case, the coupling strength is determined by the thickness of the layer between the ring and bus planes. This gap thickness can be controlled precisely and reproducibly using modern thin film deposition techniques. On the downside, the fabrication process is somewhat cumbersome since the bus and ring features must be defined in separate lithography steps.

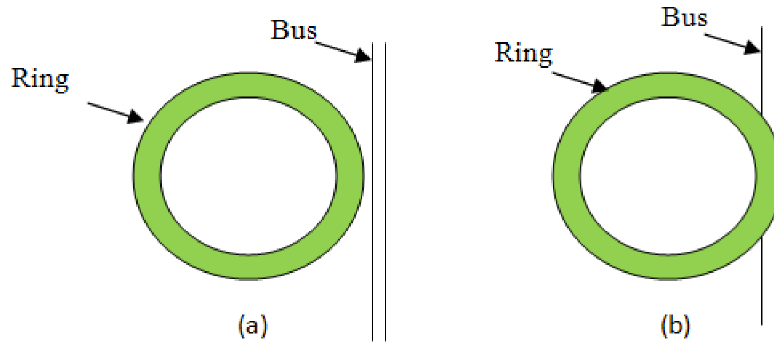

Figure 6.7: Plan-view drawing of a laterally coupled ring resonator in (a) and a vertically coupled structure in (b).

6.5.3. Output Coupling via Spiral Cavities

Pioneering work by R. K. Chang and colleagues at Yale University has demonstrated well-controlled and highly directional output light emission from WGM confined within in spiral-shaped laser cavities [73]. A plan view diagram of such a cavity structure is presented in Fig. 6.8. The periphery of the spiral cavity is defined by as follows

$$r(\phi) = r_o\left(1 + \frac{\varepsilon\phi}{2\pi}\right), \qquad (6.15)$$

where r_o is the radius of the spiral micro-cavity at $\phi = 0$, ε is the deformation factor, and $r_o\varepsilon$ is the size of the spiral notch. Efficient out-coupling of light is facilitated via diffraction of WGMs

at the notch [74]. It was found that the angle of emission relative to the notch surface can vary depending on the roughness of the spiral sidewalls among other factors. Notwithstanding this complication, light emission is observed normal to the notch as originally anticipated when the spiral cavity is prepared with smooth sidewalls [75]. In our present work, we have used the spiral cavity design to out-couple light from WGM laser structures. Investigating the effect of varying the cavity radius (r_{cavity}), the width of the pumped region (δ_{SW}), the separation between the pumped region and the edge of the cavity (δ_{ME}), the sidewall roughness, and the sidewall profile on the laser performance, we have also studied the effect of the deformation parameter (ε) on the light output.

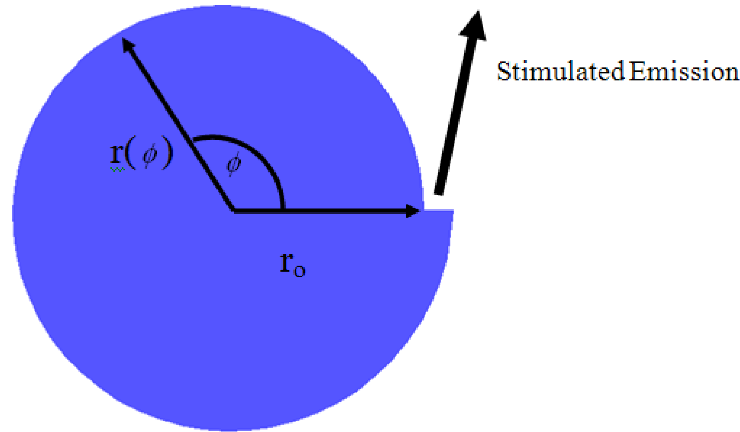

Figure 6.8: Plan view drawing of a spiral-shaped WGM laser.

In order to study the effect of diffraction loss on the performance of such lasers, rcavity is varied while keeping both δSW and δME constant. Moreover, the sidewall of the optical cavity is covered with a SiNy dielectric film and the thickness is varied by design to study the effect of reduced light scattering on laser performance. Furthermore, we have also varied δME while keeping rcavity and δSW constant to investigate the effect of the overlap of the pumped region with either the fundamental radial mode and/or the higher order radial modes. Lastly, we varied δSW while keeping rcavity constant to show how a smaller "active" volume impacts laser. Additional details are provided in Appendix E regarding laser design parameters and their connection to the device fabrication process.

References

[1] E. A. J. Marcatili, “Bends in optical dielectric guides,” *Bell Syst. Tech. J*., vol. 48, pp. 2103-2132 (1969).

[2] V. B. Braginsky *et. al.,* “ Quality-factor and nonlinear properties of optical whispering-galley modes”, *Phys. Lett. A*, vol. 137, pp. 393-396 (1989).

[3] R.K. Chang and A. J. Campillo,*Optical Processes in Microcavites,* World Scientific, Singapore (1996).

[4] M.L. Gorodetsky, A. A. Savchenkov, and V.S.Ilchenko,”Ultimate Q of optical microsphere resonators,” *Opt. Lett*., vol. 21, pp. 453-455 (1996).

[5] K. Srinivasan, M. Borselli, T. J. Johnson, P. E. Barclay, O. Painter, A. Stintz and S. Krishna, “ Optical loss and lasing characteristics of high-quality-factor AlGaAs microdisk resonators with embedded quantum dots”, *Appl. Phys. Lett.,* vol. 86 pp.151106 (2005).

[6] M.L. Gorodetsky, A. A. Savchenkov, and V.S.Ilchenko,”Ultimate Q of optical microsphere resonators,” *Opt. Lett*., vol. 21, pp. 453-455 (1996).

[7] S. C. Hill and R. E. Benner, “Morphology-dependent resonances associated with stimulated process in microspheres,” *J. Opt. Soc. Am. B*, vol. 3, pp 1509 (1986).

[8] D. K. Armani, T. J. Kippenberg, S. M. Spillane, K. J. Vahala,” Ultra-high-Q toroid microcavity on a chip”. *Lett. to Nature, or Nature*, vol. 421, pp. 925-928 (2003).

[9] S. M. Spillane, T. J. Kippenberg, K. J. Vahala,” Ultralow-threshold Raman laser using a spherical dielectric microcavity’, *Nature* , vol. 415, pp. 621-623 (2002).

[10] C. G. B. Garret, W. Kaiser, W. L. Bond,” Stimulated Emission into Optical whispering Modes of Spheres,” *Phys. Rev*., vol. 124, pp.1807-1809 (1961).

[11] B. E. Little and S. T. Chu, "Estimating surface-roughness loss and output coupling in microdisk resonators," *Opt. Lett*., vol. 21, pp. 1390-1392 (1996).

[12] M. K. Chin, D. Y. Chu, and S. T. Ho, "Estimation of the spontaneous emission factor for microdisk lasers via the approximation of whispering gallery modes, "*J. Appl. Phys.*, vol. 75, pp. 3302-3307 (1994).

[13] N. C. Frateschi and A. F. J. Levi, "Resonant modes and laser spectrum of microdisk lasers," *Appl. Phys. Lett.,* vol. 66, pp. 2932-2934 (1995).

[14] S. J. Choi, K. Djordjev, S. J. Choi, P. D. Dapkus, W. Lin, G. Griffel, R. Menna, and J. Connolly, " Microring Resonators Vertically Coupled to Buried Heterostructure Bus Waveguides," *IEEE Photon. Technol. Lett.*, vol. 16, pp. 828-830 (2004).

[15] B.E. Little, S. T. Chu, P.P. Absil, J. V. Hryniewicz, F. G. Johnson, F. Seiferth, D. Gill, V. Van, O. King, and M. Trakalo, " Very High-Order Microring Resonator Filters for WDM Applications," *IEEE Photon. Technol. Lett.,* vol. 16, pp. 2263-2265 (2004).

[16] B. Gayral, J. M. Gerard, A. Lemaitre, C. Dupuis, L. Manin, and J. L. Pelouard, "High-Q Wet-Etched GaAs Microdisks Containing InAs Quantum Boxes," *Appl. Phys. Lett.*, vol. 75, pp 1908-1910 (1999).

[17] B. Gayral and J. M. Gerard, "Strong Purcell Effect for InAs Quantum Boxes in High-Q Wet-Etched Microdisks, " *Physica E*, vol. 7, pp.641-645 (2000).

[18] N. C. Frateschi and A. F. J. Levi, "The Spectrum of microdisk lasers", *J. Appl. Phys.*, vol. 80, pp. 644-653 (1996).

[19] Di Liang, Douglas C. Hall and Gregory M. Peake "Oxidation Smoothing of Sidewall Roughness in AlGaAs Heterostructure Waveguides," *LEOS 2005: The 18th Annual Lasers and Electro Optics Society Meeting*, paper TuY 4 (Sydney, Australia, October 23-27 (2005).

[20] D. Liang and D. C. Hall, "Reduction of etched AlGaAs sidewall roughness by oxygen-enhanced wet thermal oxidation," *Appl. Phys. Lett.,* vol 91, 061110 (2007).

[21] E.C.M. Pennings, J. Van Schoonhoven, J. W. M. Van Uffelen, and M. K. Smith: “Reduction bending and scattering losses in new optical “double-ridge” waveguide”, *Electron. Lett.,*vol. 25 (11), pp. 746-748 (1989).

[22] J. M. Dallesasse, N. Holonyak Jr., A. R. Sugg, T. A. Richard, and N. El-Zein,”Hydrolyzation oxidation of $Al_xGa_{1-x}As$-AlAs-GaAs quantum well heterostructures and superlattices,” *Appl. Phys. Lett.,* vol. 57, pp. 2844-2846 (1990).

[23] K. D. Choquette, K. M. Geib, C. I. H. Ashby, R. D. Twesten, O. Blum, H. Q. Hou, D. M. Follstaedt, B. E. Hammons, D. Mathes, and R. Hull, “Advances in selective wet oxidation of AlGaAs alloys,” *IEEE J. Sel. Topics Quantum Electron.,* vol. 3, no.3, pp. 916-926 (1997).

[24] W. B. Joyce, “Current-crowded carrier confinement in double-heterostructure lasers, “ *J. Appl. Phys.,* vol. 51, pp.2394-2401 (1980).

[25] W. T. Tsang, R. Kapre, M. C. Wu, and Y. K. Chen, “Low-threshold InGaAs strined-layer quantum well lasers (=0.98um) with GaInP cladding layers prepared by chemical beam epitaxy,” *Appl. Phys. Lett.,* vol. 61, pp. 755-757 (1992).

[26] C. P. Chao, S. Y. Hu, K. –K. Law, D. B. Young, J. L. Merz, and A. C. Gossard, “Low-threshold InGaAs/GaAs strained layer single quantum well lasers with simple ridge Waveguide structure,” *J. Appl. Phys.,* vol. 69, pp. 7892-7894 (1991).

[27] S. Y. Hu, D. B. Young, S. W. Corzine, A. C. Gossard, and L. A. Coldren, “ High efficiency and low-threshold InGaAs/AlGaAs quantum-well lasers,” *J. Appl. Phys.*, vol, 76, pp 3932-3934 (1994).

[28] S. Y. Hu, D. B. Young, A. C. Gossard, and L. A. Coldren, “The effect of lateral leakage current on the experimental Gain/Current-Density Curve in Quantum-Well Ridge-Waveguide Lasers,” *IEEE J. Quantum Electronics*, vol.30, pp 2245-2250 (1994).

[29] L.A. Coldren and S. W. Corzine, Diode Lasers and Photonics Integrated Circuits. New York: Wiley (1995).

[30] T. Krauss, P.J.R. Laybourn," Very Low Threshold current operation of semiconductor ring lasers", *IEE Proceedings-J*, vol. 139, no. 6, pp. 383-388 (1992).

[31] S. L. McCall , A. F. J. Levi, R. E. Slusher, S. J. Pearton, and R. A. Logan," Whispering-gallery mode microdisk lasers," *Appl. Phys. Lett.*, vol. 60, pp. 289-291 (1992).

[32] B. Corbett and W. M. Kelly, "Surface recombination in dry etched AlGaAs/GaAs double heterostructure *p-i-n* mesa diodes," *Appl. Phys. Lett.*, vol 62, pp. 87-89 (1993).

[33] G. P. Schwartz, G. J. Gualtieri, J. E. Griffith, and B. Schwartz," Interfacial Arsenic Growth in Anodic Oxide/GaAs Structures," *J. Electrochem. Soc.*, vol. 128, pp.410-415 (1981).

[34] C. D. Thurmond, G. P. Schwartz, G. W. Kammlott, and B. Schwartz," GaAs Oxidation and the Ga-As-O Equilibrium Phase Diagram," *J. Electrochem. Soc.*, vol. 127, pp. 1366-1371 (1980).

[35] F. Capasso and G. F. Williams," A Proposed Hydrogenation/Nitridization Passivation Mechanism for GaAs and Other III-V Semiconductor Decvices, Including InGaAs Long Wavelength Photodetectors", *J. Electrochem. Soc.*, vol. 129, pp. 821 (1982).

[36] W. E. Spicer, I. Lindau, P. Skeath, and C. Y. Su, and P. Chye, "Unified defect model and beyond," *J. Vac. Sci. Technol.*, vol. 17, pp. 1019 (1980).

[37] W. E. Spicer, Z. Liliental-Weber, E. Weber, N. Newman, T. Kendelewicz, R. Cao, C. McCants, P. Mahowald,K. Miyano, and I. Lindau," The advanced unified defect model for Schottky barrier formatioin," *J. Vac. Sci. Technol.*, vol. B6, pp.1245-1251 (1988).

[38] R. P. H. Chang, T. T. Sheng, C. C. Chang, and J. J. Coleman, " The effect of interface arsenic domains on the electrical properties of GaAs MOS structure," *Appl. Phys. Lett.*, vol. 33, pp. 341-342 (1978).

[39] W. S. Hobson, U. Mohideen, S. J. Pearton, R. E. Slusher, and F. Ren, "SiN_x/Sulfide Passivated GaAs-AlGaAs Microdisk Lasers," *Electron. Lett.*, vol. 29, pp. 2199-2200 (1993).

[40] C. J. Sandroff, R. N. Nottenburg, J. C. Bischoff, and R. Bhat," Dramatic enhancement in the gain of a GaAs/AlGaAs heterostrucure bipolar transistor by surface chemical passivation," *Appl. Phys. Lett.,* vol. 51, pp. 33-35 (1987).

[41] P. W. Li, Q. Wang, and E. S. Yang, "Chemical and electrical characterization of AlGaAs/GaAs heterojuntion bipolar transistors treated by electron cyclotron resonanc plasmas," *Appl. Phys. Lett*., vol. 60, pp. 1996-1998 (1992).

[42] A. Callegari, P. D. Hoh, D. A. Buchanan, and D. Lacey, " Unpinned gallium oxide/GaAs interface by hydrogen and nitrogen surface plasma treatment," *Appl. Phys. Lett.*, vol. 54, pp. 332-334 (1989).

[43] Z. Lu, M. T. Schmidt, D. Chen, R. M. Osgood Jr. ,W. M. Holber, D. V. Podlesnik, and J. Forster, " GaAs-oxide removal using an electron cyclotron resonance hydrogen plasma," *Appl. Phys. Lett*.,vol. 58, pp. 1143-1145 (1991).

[44] C. Y. Wu and M. S. Lin," Influence of NH_3 plasma pretreatment on the properties of plasma-enhanced chemical-vapor-deposited SiON on GaAs interface," *J. Appl. Phys.*, vol. 60, pp. 2050-2057 (1986).

[45] R. A. Gottscho, B. L. Preppernau, S. J. Pearton, A. B. Emerson, and K. P. Giapis," Real-time monitoring of low-temperature hydrogen plasma passivation of GaAs," *J. Appl. Phys*., vol. 68, pp. 440-445 (1990).

[46] E. Yoon, R. A. Gottscho, V. M. Donnelly, and H. S. Luftman, " GaAs surface modification by room-tempreture hydrogen plasma passivation," *Appl. Phys. Lett*., vol. 60, pp. 2681-2683 (1992).

[47] E. S. Aydil, Z. H. Zhou, R. A. Gottscho, and Y. J. Chabal, " Real time *in situ* monitoring of surfaces during glow discharge processing: NH_3 and H_2 plasma passivation of GaAs," *J. Vac. Sci. Technol. B*, vol. 13, pp. 258-267 (1995).

[48] C. J. Sandroff, M. S. Hegde, L. A. Farrow, R. Bhat, J. P. Harbison, and C. C. Chang," Enhanced electronic properties of GaAs surfaces chemically passivated by selenium reactions," *J. Appl. Phys*.,vol. 67, pp. 586-588 (1990).

[49] J. –F. Fan, H. Oigawa, and Y. Nannichi," Metal-dependent Schottky barrier height with the $(NH_4)_2S_x$-treated GaAs," *Jpn J. Appl. Phys*.,vol. **27**, p. L2125 (1988).

[50] Jun-Youn Kim, Jawoong Lee, Jungyeon Kim, Bongkoo Kang, and O'Dae Kwan "Effect of surface treatment on leakage current of GaAs/AlGaAs laser microcavities", *Appl. Phys. Lett*., vol. 82, pp. 4504 (2003).

[51] H. H. Wieder, " Perspective on III-V Compound MIS-Structure," *J. Vac. Sci. Technol.,* vol. 15, pp. 1498-1506 (1978).

[52] J. M. Woodall and J. L. Freeouf, " GaAs metallization: Some problems and trends," *J. Vac. Sci. Technol.*,vol. 19, pp. 794 -798 (1981).

[53] U. Mohideen, W. S. Hobson, S. J. Pearton, F. Ren, and R. E. Slusher, " GaAs/AlGaAs microdisk lasers," *Appl. Phys. Lett*. vol. 64, pp. 1911 (1994).

[54] Y. Yamamoto and R. E. Slusher, " Optical Processes in Microcavities," *Phys. Today* , vol. 46, pp.66-73 (1993).

[55] K. Vahala, "Optical microcavities," *Nature* , vol. 424, pp. 839-846 (2003).

[56] J. P. Zhang, D. Y. Chu, S. L. Wu, S. T. Ho, W. G. Bi, C. W. Tu, and R. C. Tiberio, " Photonic-wire laser," *Phys. Rev. Lett.*, vol. 75, pp. 2678-2681 (1995).

[57] S. A. Backes, J. R. A. Cleaver, A. P. Heberle, and K. Kohler," Microdisk laser structures for mode control and directional emission," *J. Vac.Sci.Technol. B* , *Microelectron*., vol. 16, pp. 3817-3820 (1998).

[58] A. S. –H. Liao and S. Wang, "Semiconductor injection lasers with a circular resonator," *Appl. Phys. Lett.*, vol, 36, pp. 801-803 (1980).

[59] T. Krauss, P. J. R. Laybourn, and J. S. Roberts, “Cw operation of semiconductor ring lasers,” *Electron Lett.,* vol. 26, pp. 2095-2097 (1990).

[60] J. P. Hohimer, G. A. Vawter, D. C. Craft, and G. R. Hadley, “ Improving the performance of semiconductor ring lasers by controlled reflection feedback,” *Appl. Phys. Lett.,* vol. 61, pp. 1013-1015 (1992).

[61] R. van Roijen, E. C. M. Pennings, M. J. N. van Stralen, J. M. M. van der Heijden, T. van Dongen, and B. H. Verbeek, “Compact InP-based ring lasers employing multi-mode interference couplers and combiners,” *Appl. Phys. Lett.,* vol. 64, pp. 1753-1755 (1994).

[62] T. Krauss, R. M. De La Tue, I. Contijo, P. J. R. Laybourn, and J. S. Roberts, “ Strip-loaded semiconductor ring lasers employing multimode interference (MMI) output couplers,” *Appl. Phys. Lett.*, vol. 64. pp. 2788-2790 (1994).

[63] P. B. Hansen, G. Raybon, M. –D. Chien, U. Koren, B. I. Miller, M. G. Young, J. –M. Verdiell, and C. A. Burrus, “ A 1.54 um monolithic semiconductor ring laser: Cw and mode-locked operation, “ *IEEE Photon. Technol, Lett.,* vol. 4, pp. 411-413 (1992).

[64] S. Oku, M. Okayasu, and M. Ikeda, “Control of unidirectional oscillation in semiconductor orbiter lasers,” *IEEE Photon, Technol. Lett.,* vol.3, pp. 1066-1068 (1991).

[65] J. P. Hohimer, G. R. Hadley, and G. A. Vawter, “Semiconductor ring lasers with reflection output couplers, “*Appl. Phys. Lett.,* vol. 63, pp. 278-280 (1993).

[66] G. D. Chern, H. E. Tureci, A. Douglas Stone, M. Kneissl, N. M. Johnson, and R. K. Chang,” Unidirectional lasing from InGaN multiple-quantum-well spiral-shaped micropillars,” *Appl. Phys. Lett*., vol. 83, pp. 1710-1712 (2003).

[67] M. C. Shih , M. H. Hu, M. B. Frelier, M. Levy, R. Scarmozzino, R. M. Osgood, Jr., I. W. Tao, and W. I. Wang, “Fabrication of an InGaAs single quantum well circular ring laser by direct laser patterning,” *Appl. Phys. Lett.*, vol. 66, pp. 2608-2610 (1995)

[68] B. E. Little, S. T. Chu, and H. A. Haus, "Micro-ring resonator channel dropping filters," *presented at IEEE Lasers and Electro-Optics society, 8th Annual Meeting* (1995).

[69] D. Rafizadeh, J. P. Zhang, S. C. Hagness, A. Taflove, K. A. Stair, S. T. Ho, and R. C. Tiberio, "Waveguide-coupled AlGaAs/GaAs microcavity ring and disk resonators with high finesse and 21.6-nm free spectral range," *Optics Letters,* vol. 22, pp. 1244-1246 (1997).

[70] Y.-L. Pan, and R. K. Chang, " Highly Efficient Prism Coupling to Whispering Gallery Modes of a Square Miro-Cavity," *Applied Physics Letter,* vol. 82, pp. 487-489 (2003).

[71] A. Yariv, "Critical Coupling and its Control in Optical Waveguide-Ring Resonator Systems," *IEEE Photonics Technology Letters,* vol. 14, pp. 483-485 (2002).

[72] B. E. Little, S. T. Chu, W. Pan, D. Ripin, T. Kaneko, Y. Kokubun, and E. P. Ippen, "Viertically coupled glass microring resonator channel dropping filters," *IEEE Photonics Technology Letters*, vol. 11, pp. 215-217 (1999).

[73] M. K. Chin and S. T. Ho, "Design and modeling of Waveguide-coupled single-mode microring resonators," *Journal of Lightwave Technology*, vol. 16, pp 1433-1446 (1998).

[74] M. Kneissl, M. Teepe, N. Miyahsita, N. M. Johnson, G. D. Chern, R. K. Chang," Current-injection spiral-shaped microcavity disk laser diodes with unidirectional emission," *Appl. Phys. Lett*. vol 84, pp. 2485-2487 (2004).

[75] G. Chern, G. E. Fernandes, R. K. Chang, Q. Song, L. Xu, M. Kneissl, and N. Hohnson, " High-Q-Preserving Coupling Between a Spiral and a semicircle Micro-Cavity," *Optics Letters*, vol. 32, pp. 1093-1095 (2007).

7. SUMMARY AND CONCLUSIONS

Significant technical barriers remain to the wide spread adoption of WGM lasers as the essential building block in large-scale photonic integrated circuits. The first challenge is to reduce the electrical power consumption at desirable levels of light output power. The second target is to obtain highly directional light emission without sacrificing other laser performance metrics and to provide a convenient means for coupling light into adjacent circuit elements. It is our viewpoint that the best opportunity for success lies in the pursuit of relatively small but nevertheless high-performance *μ-Pillar lasers* with spiral-geometry cavities.

The body of work represented by this Ph.D. dissertation, and its companion oral presentation, demonstrates two different kinds of contribution, one internal to Virginia Tech and the other involving the broader community of researchers working on the science and technology of semiconductor lasers. With regard to the former, process technology for making WGM lasers was developed from scratch and then carefully optimized to achieve various milestones along the way. Key focal points include (1) a highly refined ICP etching process for fabricating *μ-Pillar* optical cavities with sidewall roughness of less than 10 nm and (2) a new approach for current and carrier confinement via hydrogenation of doping impurities that is fully compatible with all other processing steps and robust in comparison with earlier reports on similar techniques. WGM laser devices have been built with these new processing capabilities and tested using purpose-made experimental apparatus following careful calibration procedures.

With regard to contributions having impact beyond Virginia Tech, a comprehensive photolithographic mask has been designed and manufactured that enables investigation of the interplay between device geometry and WGM laser performance. Emphasis has been placed on designing experiments to determining the impact of diffraction and scattering losses, current and carrier confinement, and surface recombination on electrical/optical device characteristics. For example, it has been demonstrated that the hydrogenation procedure can be decoupled from the ohmic contact formation process. This enables post-hydrogenation annealing over a wide range

of conditions as necessary to improve current confinement without compromising the quality of the metal/semiconductor electrodes. In addition, a methodology has been developed for separating out process optimization work from the task of identifying the most promising means of directional light out-coupling. Our device fabrication methods can be proven on WGM lasers with pure cylindrical symmetry, hence results from these experiments should be independent of the details of our approach to light output coupling. Particular attention has been paid to the fact that device geometries that give the best performance for purely symmetrical cavities may not yield the highest level of light emission from the spiral output notch. Such considerations seem to be missing from much of the earlier work reported in the literature.

Finally, it has been demonstrated that our processing techniques and device designs yield WGM laser that can be used in photonic integrated circuits. Our individual WGM lasers outperform those designed and fabricated at Xero PARC. These devices have been incorporated into multi-element, coupled-cavity optical circuits as part of our collaboration with Dr. R. K. Chang's group at Yale University. The effects of selective current injection into composite structures containing up to three coupled *μ-Pillar* cavities have been studied in some detail. This direct coupling scheme enables low-loss transmission of lasing modes between elements, as well as efficient coupling of amplified spontaneous emission between adjacent resonators. With this capability in hand it is now possible to consider building digital photonic gates for the purpose of executing AND, OR, and NOT logic functions.

Appendix A: Analysis of Optical Modes in Slab Waveguides

An analysis of the transverse optical modes in slab waveguides is presented herein. In order to simplify the analysis, a 1-D waveguide approach was implemented and only even TE modes were given consideration. A 2-D numerical calculation should be pursued if it is desirable to have more accurate solutions; however, it is not necessary in the present case. Figure A.1 shows a schematic of in-plane laser showing the selected coordinate system. We can see here that the optical propagation axis is the z-axis, which will be referred to as the *longitudinal* direction. The y-direction is the direction of growth, which will be referred to as the *transverse* direction. The x-direction is in the plane of the substrate and it will be called the *lateral* direction.

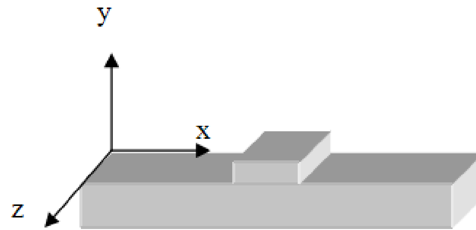

Figure A.1: Schematic of in-plane laser showing selected coordinate system.

A schematic of energy vs. position diagram is shown in Fig. A.2. The thickness of the optical confinement layer (OCL) is denoted as *b*. The thickness of the quantum well (QW) layer is denoted as *a*.

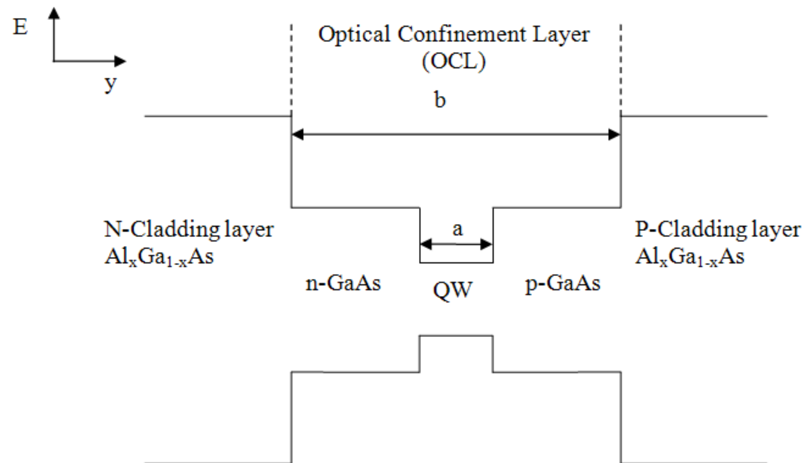

Figure A.2: Schematic of energy vs. position diagram for separate confinement quantum well heterostructure laser.

The refractive index profile with the optical field distribution is shown in Fig. A.3. From the refractive index profile, we can see that we have a symmetric five layer dielectric slab waveguide.

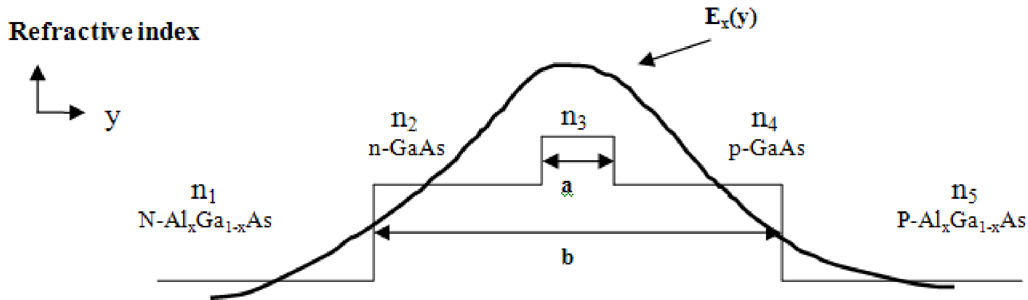

Figure A.3: Refractive index profile with the optical-field distribution

Since the dimension of the active layer *a*, is much smaller than the dimension of the OCL *b*, and the refractive index weakly depends on doping type, then, we can simplify the analysis to demonstrate the waveguiding proprieties by using the symmetric three layer slab waveguide showing in Fig. A.4.

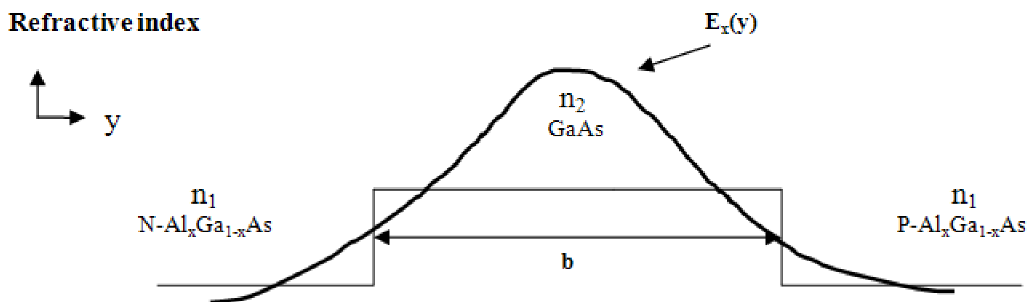

Figure A.4: shows the refractive index profile with the optical-field distribution using the symmetric three layer slab waveguide assumption because a<<b , $n_1 \approx n_5$, and $n_2 \approx n_3 \approx n_4$.

Viewing Fig.A.4 in the yz-plane we can get a schematic of a one dimensional three-layer slab waveguids shown in Fig.A.5. Region I consists of P-cladding layer and regionIII

consists of N-cladding layer. Both cladding layers are $Al_{0.8}Ga_{0.2}As$. Region II consists of GaAs as the optical confinement layer.

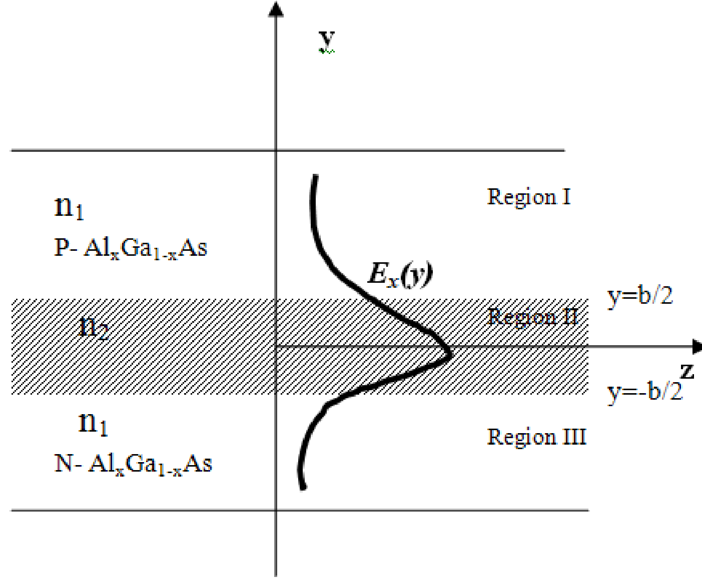

Figure A.5: Schematic of the symmetric three layer slab waveguide

Following the analysis in [1] and starting from Maxwell's equations expressed as:

$$\nabla \times \vec{E} = -\frac{\partial \vec{B}}{\partial t} = -\mu_o \frac{\partial \vec{H}}{\partial t} \qquad \text{(A.1)}$$

$$\nabla \times \vec{H} = \varepsilon \frac{\partial \vec{E}}{\partial t} \qquad \text{(A.2)}$$

The vector wave equation for $\vec{E}$ field becomes:

$$\nabla^2 \vec{E} = \mu_0 \varepsilon \frac{\partial^2 \vec{E}}{\partial t^2} \qquad \text{(A.3)}$$

Where ε is the dielectric constant and μ_o is the magnetic permeability. Eq.(A.3) can be reduced to three independent scalar wave equations as follows:

$$\nabla^2 E_x = \mu_o \varepsilon \frac{\partial^2 E_x}{\partial t^2} \qquad \text{(A.4)}$$

$$\nabla^2 E_y = \mu_o \varepsilon \frac{\partial^2 E_y}{\partial t^2} \qquad \text{(A.5)}$$

$$\nabla^2 E_z = \mu_o \varepsilon \frac{\partial^2 E_z}{\partial t^2} \qquad \text{(A.6)}$$

Upon expanding the curl of E and H in Eq(s). (A.1) and (A.2), we get the following:

$$a_x\left(\frac{\partial E_z}{\partial y}-\frac{\partial E_y}{\partial z}\right)-a_y\left(\frac{\partial E_z}{\partial x}-\frac{\partial E_x}{\partial z}\right)+a_z\left(\frac{\partial E_y}{\partial x}-\frac{\partial E_x}{\partial y}\right)=-\mu_o\left[a_x\left(\frac{\partial H_x}{\partial t}\right)+a_y\left(\frac{\partial H_y}{\partial t}\right)+a_z\left(\frac{\partial H_z}{\partial t}\right)\right] \quad (A.7)$$

$$a_x\left(\frac{\partial H_z}{\partial y}-\frac{\partial H_y}{\partial z}\right)-a_y\left(\frac{\partial H_z}{\partial x}-\frac{\partial H_x}{\partial z}\right)+a_z\left(\frac{\partial H_y}{\partial x}-\frac{\partial H_x}{\partial y}\right)=\varepsilon\left[a_x\left(\frac{\partial E_x}{\partial t}\right)+a_y\left(\frac{\partial E_y}{\partial t}\right)+a_z\left(\frac{\partial E_z}{\partial t}\right)\right] \quad (A.8)$$

The wave equation for TE modes was analyzed in [1]. The center of the active layer is y=0. The waveguide is considered to be infinite in the lateral direction (x-direction) and thus no variations for fields with respect to x; therefore, we will have the following:

$$\frac{\partial}{\partial x} = 0 \qquad \text{(A.9)}$$

$$E_z = 0 \qquad \text{(A.10)}$$

From (A.7), (A.8), (A.9), and (A.10) we get:

$$H_x = E_y = 0$$

Therefore, Eq(s).(A.5) and (A.6) can be eliminated, and only Eq.(A.4) is considered. The wave equation that governs TE modes can be written as:

$$\frac{\partial^2 E_x}{\partial y^2} + \frac{\partial^2 E_x}{\partial z^2} = \mu_o \varepsilon \frac{\partial^2 E_x}{\partial t^2} \qquad \text{(A.11)}$$

To solve Eq.(A.11), the analysis in [1] will be followed and the separation of variables technique [2] will be used. We will start by assuming a solution of the form

$$E_x(y,z,t) = YZT \qquad \text{(A.12)}$$

Where Y represents a function of y only, Z represents a function of z only, and T represents a function of t only. If we substitute Eq.(A.12) into Eq.(A.11), we will get the following:

$$Y''ZT + YZ''T = \mu_o \varepsilon YZT'' \qquad \text{(A.13)}$$

Now, if we divide Eq.(A.13) by Eq.(A.12) will get

$$\frac{Y''}{Y}+\frac{Z''}{Z}=\mu_o\varepsilon\frac{T''}{T} \qquad \text{(A.14)}$$

From Eq.(A.14), we find that the left-hand side does not depend on time. Hence, the right-hand side can't vary with time and, therefore, should equal a constant.

$$\mu_o\varepsilon\frac{T''}{T}=-K^2 \qquad \text{(A.15)}$$

Eq.(A.15) can be written as:

$$T''+\left(\frac{K}{\sqrt{\mu_o\varepsilon}}\right)\cdot T=0 \qquad \text{(A.16)}$$

The solution of Eq.(A.16) is

$$T = A\cdot e^{j\cdot\left(\frac{K}{\sqrt{\mu_o\varepsilon}}\right)\cdot t}+B\cdot e^{-j\cdot\left(\frac{K}{\sqrt{\mu_o\varepsilon}}\right)\cdot t} \qquad \text{(A.17)}$$

For sinusoidal dependence,

$$e^{j(\omega)t}=e^{j\cdot\left(\frac{K}{\sqrt{\mu_o\varepsilon}}\right)t} \qquad \text{(A.18)}$$

From Eq.(A.18), we find that

$$K^2=\omega^2\mu_o\varepsilon \qquad \text{(A.19)}$$

Now, we can write Eq.(A.14) as

$$\frac{Y''}{Y}+\frac{Z''}{Z}=-\omega^2\mu_o\varepsilon \qquad \text{(A.20)}$$

If we write Eq.(A.20) as

$$\frac{Z''}{Z} = -\left(\frac{Y''}{Y}\right) - \omega^2 \mu_o \varepsilon \qquad \text{(A.21)}$$

We can see from Eq.(A.21) that the left-hand side does not vary with y; therefore, the right-hand side cannot vary with y and should equal a constant

$$-\left(\frac{Y''}{Y}\right) - \omega^2 \mu_o \varepsilon = -\beta^2 \qquad \text{(A.22)}$$

Rearranging Eq.(A.22), we get

$$Y'' + (\omega^2 \mu_o \varepsilon - \beta^2) Y = 0 \qquad \text{(A.23)}$$

We know that from [1]

$$\omega^2 \mu_o \varepsilon = n^2 k_o{}^2 \qquad \text{(A.24)}$$

We can write Eq.(A.23) as:

$$\frac{d^2 E_x(y)}{dy^2} + (n^2 k_o{}^2 - \beta^2) E_x(y) = 0 \qquad \text{(A.25)}$$

Where n is the index of refraction, k_o is the free space propagation constant and β is the phase or the axial propagation constant. In region II, We can assume solutions of the form,

$$E_x(y) = A\cos(\chi y) + B\sin(\chi y) \qquad \text{(A.26)}$$

For even TE modes, Eq.(A.26) becomes:

$$E_x(y) = A\cos(\chi y) \qquad \text{(A.27)}$$

In region I, we can assume solutions of the form,

$$E_x(y) = Ce^{-\gamma y} \qquad \text{(A.28)}$$

Substituting Eq.(A.27) into Eq.(A.25), we get

$$\chi^2 = n_2^{\ 2} k_o^{\ 2} - \beta^2 \quad \text{(A.29)}$$

And substituting Eq.(A.28) into Eq.(A.25), we get

$$\gamma^2 = \beta^2 - n_1^{\ 2} k_o^{\ 2} \quad \text{(A.30)}$$

To get the characteristic equation, we need to apply the boundary condition at the dielectric interface between region I and region II. The boundary condition between region I and region II require that the tangential components of both electric and magnetic fields be continuous [1]. Therefore, the following can be stated:

$$E_{x_regionI}(y) = E_{x_regionII}(y) \qquad \text{at} \qquad y=b/2 \quad \text{(A.31)}$$

$$\frac{\partial E_{x_regionI}(y)}{\partial y} = \frac{\partial E_{x_regionII}(y)}{\partial y} \qquad \text{at} \qquad y=b/2 \quad \text{(A.32)}$$

Dividing Eq.(A.32) by Eq.(A.31), and applying the boundary condition at y=b/2. We can get the characteristic equation,

$$\tan\left(\frac{\chi b}{2}\right) = \frac{\gamma}{\chi} \quad \text{(A.33)}$$

In order to find χ and γ, the characteristic equation, Eq.(A.33), needs to be solved graphically or numerically. The graphical solution is based on the technique presented in [3]. We first need to write Eq.(A.33) as:

$$\left(\frac{\chi b}{2}\right)\tan\left(\frac{\chi b}{2}\right) = \left(\frac{\gamma b}{2}\right) \quad \text{(A.34)}$$

Then, from Eq.(A.29) and Eq.(A.30), we eliminate β and multiply the result by $\left(\frac{b}{2}\right)^2$ to obtain the following equation,

$$\left(\frac{\gamma b}{2}\right)^2 + \left(\frac{\chi b}{2}\right)^2 = \left(\frac{k_o b}{2}\right)^2 \left(n_2^{\ 2} - n_1^{\ 2}\right) \quad \text{(A.35)}$$

The cut-off values for each higher-order mode are given by the intersection of the curves generated by Eq.(A.34) with the $\left(\frac{\chi b}{2}\right)$ axis. For even modes, m, where m= 2, 4, 6, this occurs at $\left(\frac{\chi b}{2}\right)=\frac{m\pi}{2}$. So rearranging Eq.(A.35) and solving for *b*, yield the following equation.

$$b=\frac{m\lambda_o}{2\cdot\left(\sqrt{n_2^{\,2}-n_1^{\,2}}\right)} \tag{A.36}$$

Equation (A.36) will give you the value of *b* at cutoff.

The thickness of the optical confinement layer (OCL) is represented by *b*. In our material structure, see Table 3.1, *b*=0.26μm. Also, the emission wavelength of our laser device is λ_o=795*nm*, therefore, k_o is calculated using the following equation as follows:

$$k_0=\frac{2\pi}{\lambda_o}=7.9\times10^4\,cm^{-1} \tag{A.37}$$

The optical parameters of the materials are taken from [4]. For GaAs, n_2 = 3.6 and for $Al_{0.85}Ga_{0.15}As$, $n_1\approx3.16$. The intersection of Eq.(A.34) and Eq.(A.35) will give the desired solution, see Fig.A.6.

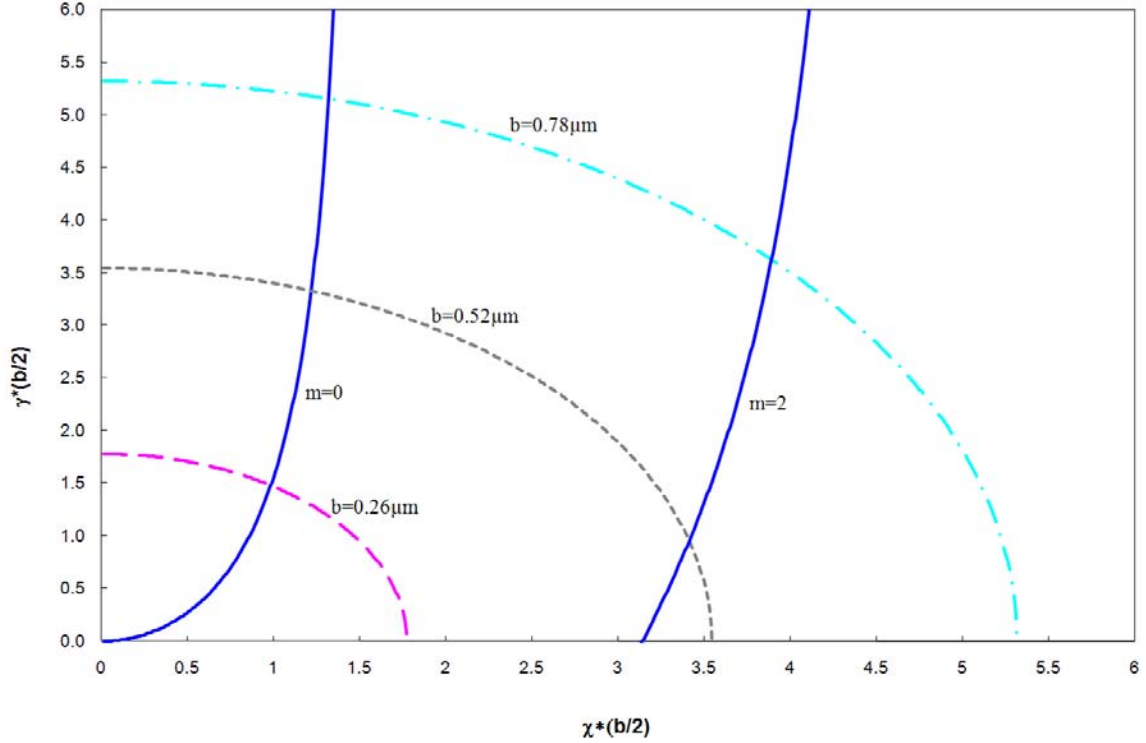

Figure A.6: Graphical solution of the characteristic equation for the even TE modes. The intersection shows the desired solution.

Only the positive values of (γ^{*}b/2) are considered because negative values of (γ^{*}b/2) are unguided waves [1]. For b=0.26, 0.52, and 0.78 µm, circles of radii given by the right side of Eq.A.35 are shown by the dotted lines in Fig.A.6. At b= 0.26 µm, an intersection near (χ*b/2) ≈0.98 is obtained only with the m=0 curve, which is the solution for the lowest-order or fundamental mode. No matter how small b becomes, this mode is never cutoff in symmetric structure [1]. The values of χ and γ obtained in this way permit calculation of the field distribution. Increasing b to 0.52 µm leads to an intersection close to (χ^{*}b/2) ≈1.2 for the m=0 mode and (χ^{*}b/2) ≈3.4 for the m=2 mode. Furthermore, for b=0.78 µm, the intersection occurs at (χ^{*}b/2) ≈ 1.3 for m=0 mode and (χ^{*}b/2) ≈3.8 for m=2 mode.

Table A.1: shows the OCL thickness (b) with the corresponding index mode (m), χ , γ , and the propagation constant (β).

b (μm)	m	χ (cm^{-1})	γ (cm^{-1})	β (cm^{-1})
0.26	0	7.54×10^{4}	1.12×10^{5}	2.74×10^{5}
0.52	0,2	$4.69\times10^{4}, 1.31\times10^{5}$	$1.28\times10^{5}, 3.61\times10^{4}$	$2.81\times10^{5}, 2.52\times10^{5}$
0.78	0,2	$3.38\times10^{4}, 9.97\times10^{4}$	$1.32\times10^{5}, 9.26\times10^{4}$	$2.83\times10^{5}, 2.66\times10^{5}$

References:

[1] Cassy H. C. and Panish M.B. 1978 *Hetrostructure Laser. Part A: Fundamental Principles.*

[2] H. F. Weinberger, “Partial Differential Equations,” p. 63. Blaisdell, Waltham, Massachusetts, 1965.

[3]R. E. Collin, “Field Theory of Guided Waves,” p. 470. McGraw-Hill, New York, 1960.

[4] http://www.ioffe.rssi.ru/SVA/NSM/Semicond/index.html

Appendix B:Analysis of Optical Modes in Cylindrical Waveguides

In this appendix a detailed mode analysis for micropillar lasers is presented.

1. Basic Concepts and Governing Equations

A theoretical analysis of micropillar cavity is presented based on Maxwell's equations, which govern all electromagnetic phenomena. These equations are expressed as:

$$\nabla \times \vec{E} = -\frac{\partial \vec{B}}{\partial t} \quad \text{(B.1)}$$

$$\nabla \times \vec{H} = \vec{J} + \frac{\partial \vec{D}}{\partial t} \quad \text{(B.2)}$$

$$\nabla \cdot \vec{D} = \rho \quad \text{(B.3)}$$

$$\nabla \cdot \vec{B} = 0 \quad \text{(B.4)}$$

where the vector fields $\vec{E}$, $\vec{H}$, $\vec{D}$, and $\vec{B}$ as well as the source quantities $\vec{J}$ and ρ are generally functions of three spatial coordinates and time. In these equations $\vec{E}$ is the electric field intensity, $\vec{H}$ is the magnetic field intensity, $\vec{D}$ is the electric flux density, $\vec{B}$ is the magnetic flux density, $\vec{J}$ is the electric current density, and ρ is the volume charge density, and are measured, respectively, in V/m, A/m, C/m^2, Wb/m^2, A/ m^2, and C/m^3. Assuming that time variations are harmonic (that is, sinusoidal with frequency ω as cos(ωt) or sin (ωt)). The time dependence in complex form can be considered to be as $e^{j\omega t}$. Then, the phasor forms of Maxwell's equations are written as

$$\nabla \times \vec{E} = -j\omega \vec{B} \quad \text{(B.5)}$$

$$\nabla \times \vec{H} = \vec{J} + j\omega \vec{D} \quad \text{(B.6)}$$

$$\nabla \cdot \vec{D} = \rho \quad \text{(B.7)}$$

$$\nabla \cdot \vec{B} = 0 \quad \text{(B.8)}$$

Combining the equations (B.5) to (B.8) with the constitutive relations expressed as,

$$\vec{D} = \varepsilon\vec{E} \qquad \text{(B.9)}$$

$$\vec{B} = \mu\vec{H} \qquad \text{(B.10)}$$

Maxwell's equations are obtained in terms of two fields $\vec{E}$ and $\vec{H}$,

$$\nabla \times \vec{E} = -j\omega\mu\vec{H} \qquad \text{(B.11)}$$

$$\nabla \times \vec{H} = \vec{J} + j\omega\varepsilon\vec{E} \qquad \text{(B.12)}$$

$$\nabla \cdot (\varepsilon\vec{E}) = \rho \qquad \text{(B.13)}$$

$$\nabla \cdot (\mu\vec{H}) = 0 \qquad \text{(B.14)}$$

Solutions to any electromagnetic problem must satisfy Maxwell's equations and the associated boundary conditions. However, Maxwell's equations are a coupled set of equations as $\vec{E}$ and $\vec{H}$ are simultaneously present in the curl equations in (B.11) and (B.12). To solve Maxwell's equations, we need to have equations only in terms of $\vec{E}$ or $\vec{H}$ alone. This can be achieved using the following procedure. Taking the curl of both sides of (B.11), yields

$$\nabla \times \nabla \times \vec{E} = \nabla \times (-j\omega\mu\vec{H}) = -j\omega\mu\nabla \times \vec{H} \qquad \text{(B.15)}$$

It is emphasized that this analysis is limited to media which are homogeneous (ε and μ are constant), linear (ε and μ are not functions of fields; if the medium is nonlinear, ε and μ can change with the field intensity/light intensity), and isotropic (ε and μ do not depend on the direction of fields). We further assume that the medium is source-free; that is $\vec{J} = 0$ and $\rho = 0$. Now using the vector identity $\nabla \times \nabla \times \vec{A} = \nabla(\nabla \cdot \vec{A}) - \nabla^2\vec{A}$ in (B.15), we obtain

$$\nabla(\nabla \cdot \vec{E}) - \nabla^2\vec{E} = -j\omega\mu\nabla \times \vec{H} \qquad \text{(B.16)}$$

Since $\nabla \cdot (\varepsilon\vec{E}) = \varepsilon\nabla \cdot \vec{E} = \rho = 0$ and $\nabla \times \vec{H} = j\omega\varepsilon\vec{E}$, then (B.16) reduces to

$$\nabla^2 \vec{E} + \omega^2 \mu\varepsilon \vec{E} = 0 \qquad \text{(B.17)}$$

In a similar manner, it can be shown that

$$\nabla^2 \vec{H} + \omega^2 \mu\varepsilon \vec{H} = 0 \qquad \text{(B.18)}$$

Equations (B.17) and (B.18) are called Helmholtz wave equations. Since, in the Cartesian coordinate system $\nabla^2 \vec{E} = (\nabla^2 E_x)\hat{a}_x + (\nabla^2 E_y)\hat{a}_y + (\nabla^2 E_z)\hat{a}_z$, it can be said that every Cartesian component of $\vec{E}$ and $\vec{H}$ denoted as ψ $(= E_x,\ E_y,\ E_z,\ H_x, H_y, \text{or}\ H_z)$ satisfies the scalar-wave equation; namely,

$$\nabla^2 \psi + \omega^2 \mu\varepsilon \psi = 0 \qquad \text{(B.19)}$$

2. Solution of Helmholtz Wave Equation for Microdisk Cavity

Fig.B.1 shows the schematic illustration of a micropillar laser. It consists of a thin semiconductor disk of thickness d, radius R_o, and refractive index n_1, constituting the active region of laser, sandwiched between two layers of lower refractive index n_3. The dielectric discontinuity along the z-axis strongly confines the modal field to the active layer in the vertical z-direction. Total internal reflection at the interface boundary $r = R_0$, due to the dielectric discontinuity in the radial direction *r*, leads to the formation of Whispering Gallery resonance inside the cavity [1].

The modal solutions in the microdisk cavity, representing Whispering Gallery modes (WGMs), can be obtained by using the method of separation of variables in the cylindrical coordinate system (r, θ, z). The z-dependence is assumed to follow the slab-waveguide model for TE or TM modes. This dependence, as discussed later, is described as $\cos(uz)$ with $u = k_0\sqrt{n_1^2 - n_{eff}^2}$; $k_0 = \omega\sqrt{\mu_0\varepsilon_0} = 2\pi/\lambda$, for the fundamental mode inside the cavity (| z | < d/2) and as exponentially decaying function $e^{-w|z|}$ with $w = k_0\sqrt{n_{eff}^2 - n_3^2}$

away from the interfaces between the active region and the cladding layers with refractive index n_3 (| z | > d/2). Thus, inside the micropillar cavity $\psi(r,\theta,z)$ can be expressed as

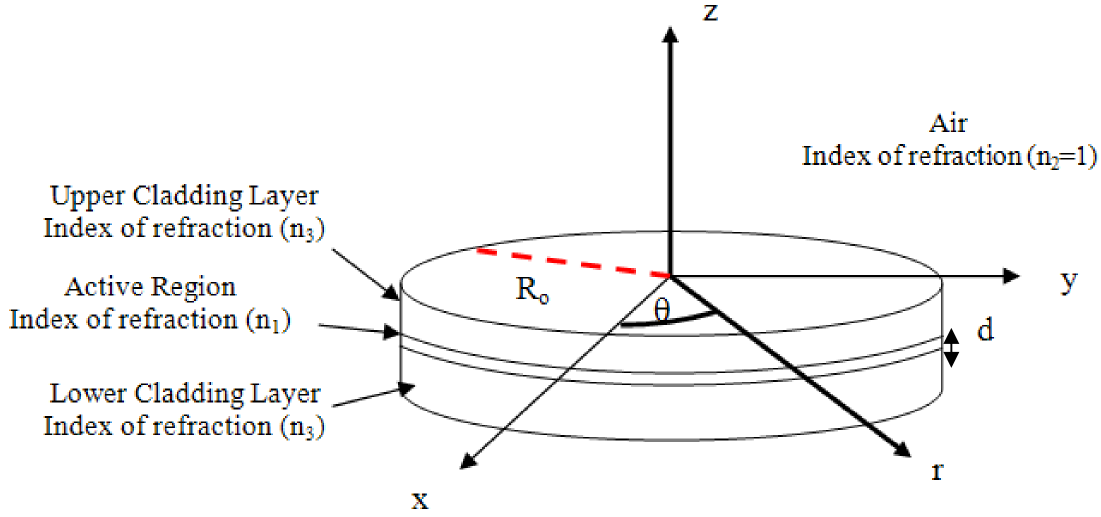

Figure B.1: Geometry and parameters for micropillar cavity

$$\psi(r,\theta,z) = R(r)\Theta(\theta)\cos(uz), r < R_o \;\&\; \frac{-d}{2} < z < \frac{d}{2} \qquad \text{(B.20)}$$

In the cylindrical coordinate system $\nabla^2\psi = \frac{1}{r}\frac{\partial}{\partial r}\left(r\frac{\partial\psi}{\partial r}\right) + \frac{1}{r^2}\frac{\partial^2\psi}{\partial\theta^2} + \frac{\partial^2\psi}{\partial z^2}$, then, (B.20) can be written as

$$\nabla^2\psi = \left[\Theta\frac{1}{r}\frac{d}{dr}\left(r\frac{dR}{dr}\right) + \frac{R}{r^2}\frac{d^2\Theta}{d\theta^2} - u^2R\Theta\right]\cos(uz) \qquad \text{(B.21)}$$

Putting (B.21) in (B.19), yields

$$\left[\Theta\frac{1}{r}\frac{d}{dr}\left(r\frac{dR}{dr}\right) + \frac{R}{r^2}\frac{d^2\Theta}{d\theta^2} - u^2R\Theta + \omega^2\mu_1\varepsilon_1R\Theta\right]\cos(uz) = 0 \quad \text{(B.22)}$$

which means that the square bracket in (B.22) must be equal to zero; that is,

$$\Theta\frac{1}{r}\frac{d}{dr}\left(r\frac{dR}{dr}\right)+\frac{R}{r^2}\frac{d^2\Theta}{d\theta^2}-(\omega^2\mu_o\varepsilon_o n_1^2-u^2)R\Theta=0 \qquad \text{(B.23)}$$

However, $\omega^2\mu_o\varepsilon_o n_1^2-u^2=k_0^2n_1^2-(k_0^2n_1^2-k_0^2n_{eff}^2)=k_0^2n_{eff}^2$, then (B.23) reduces to

$$\Theta\frac{1}{r}\frac{d}{dr}\left(r\frac{dR}{dr}\right)+\frac{R}{r^2}\frac{d^2\Theta}{d\theta^2}-k_0^2n_{eff}^2R\Theta=0 \qquad \text{(B.24)}$$

Now multiplying (B.24) by $\frac{r^2}{R\Theta}$, yields

$$\frac{r}{R}\frac{d}{dr}\left(r\frac{dR}{dr}\right)+\frac{1}{\Theta}\frac{d^2\Theta}{d\theta^2}+k^2r^2=0 \qquad \text{(B.25)}$$

where $k=k_0n_{eff}$. Since $\frac{d}{dr}(r\frac{dR}{dr})=\frac{dR}{dr}+r\frac{d^2R}{dr^2}$, then (B.25) reduces to

$$\frac{r}{R}\left(r\frac{d^2R}{dr^2}+\frac{dR}{dr}\right)+k^2r^2+\frac{1}{\Theta}\frac{d^2\Theta}{d\theta^2}=0 \qquad \text{(B.26)}$$

We observe that the first part of the left hand side of (B.26) is only a function of r while the second part is only a function of θ. The only way that (B.26) can be satisfied is if each part is constant. That is, the partial differential equation (B.26) is separated into two ordinary differential equations expressed as

$$\frac{r}{R}\left(r\frac{d^2R}{dr^2}+\frac{dR}{dr}\right)+k^2r^2=\overline{Z}^2 \qquad \text{(B.27)}$$

$$\frac{1}{\Theta}\frac{d^2\Theta}{d\theta^2}=-\overline{Z}^2 \qquad \text{(B.28)}$$

where $\bar{Z}$ is a constant. The above equations are rewritten as:

$$r^2 \frac{d^2R}{dr^2} + r\frac{dR}{dr} + (k^2r^2 - \bar{Z}^2)R = 0 \qquad \text{(B.29)}$$

$$\frac{d^2\Theta}{d\theta^2} + \bar{Z}^2\Theta = 0 \qquad \text{(B.30)}$$

The solution to (B.30) is

$$\Theta(\theta) = Be^{j\bar{Z}\theta},\ \ Be^{-j\bar{Z}\theta} \qquad \text{(B.31)}$$

where B is a constant. This dependence on θ, i.e. $e^{\pm j\bar{Z}\theta}$, implies traveling wave in the $\mp$ azimuthal direction. Thus, so far it can be said that the solutions are of standing wave type in the z-direction as implied by $\cos(uz)$ and traveling wave in the θ direction. Equation (B.29) is the Bessel differential equation. The solution of this equation is expressed as

$$R(r) = A_{\bar{Z}}J_{\bar{Z}}(kr) + A'_{\bar{Z}}Y_{\bar{Z}}(kr) \qquad \text{(B.32)}$$

where $A_{\bar{Z}}$ and $A'_{\bar{Z}}$ are constant coefficients and $J_{\bar{Z}}$ and $Y_{\bar{Z}}$ are Bessel functions of the first and second kinds, respectively. However, $Y_{\bar{Z}}(kr)$ must be excluded from the solution, because this function is unbounded (goes to $-\infty$) at $r = 0$ (on the axis of the cavity). Thus, in summary,

$$\psi(r,\theta,z) = A_{\bar{Z}}J_{\bar{Z}}(kr)\cos(uz)e^{\pm j\bar{Z}\theta}\ ,\ r < R_o\ \ \&\ \frac{-d}{2} < z < \frac{d}{2} \qquad \text{(B.33)}$$

In the solution (B.33), the constant $\bar{Z}$ must be an integer, because at a given point (r_o, θ_o, z_o) if multiple integers of 2π are added to θ_o, the physical location of the point does not change and the corresponding solution must not change either. Hence,

$$e^{\pm j\bar{Z}\theta_o} = e \pm^{j\bar{Z}(\theta_o + 2I\pi)}, \quad I = 1,2,3,..... \qquad \text{(B.34)}$$

The above solution remains valid if $e^{\pm j2\pi I\bar{Z}} = 1$, or $I\bar{Z} =$ integer which means $\bar{Z}$ must be an integer. Letting $\bar{Z} \equiv M = 0,\ \pm1,\ \pm2,.....$, then

$$\psi(r,\theta,z) = A_M J_M(kr)\cos(uz)e^{\pm jM\theta}, r < R_o \ \& \frac{-d}{2} < z < \frac{d}{2} \qquad \text{(B.35)}$$

For the above solution to represents WGMs, the boundary condition $\psi(R_o,\theta,z) = 0$ should apply, which results in

$$J_M(kR_o) = 0 \qquad \text{(B.36)}$$

3. Resonance Frequencies

The first root of (B.36) corresponds to WGMs, which can be obtained for several lower order modes from Table B.1.

Table B.1: First roots of $J_M(kR_o) = 0$ for several values of M.

M	0	1	2	3	4	5
$a_o = kR_o$	2.405	3.832	5.136	6.380	7.588	8.771

Using the results in Table B.1, the resonance frequency of the micropillar cavity is obtained from

$$a_o = kR_0 = n_{eff}k_0R_0 = n_{eff}R_0\frac{\omega_r}{c},$$

or

$$n_{eff} = \frac{a_o c}{\omega_r R_0} \qquad \text{(B.37)}$$

where $c = 3\times10^{8}\ m/s$ is the velocity of light in free space. There are, in fact, two unknowns in (B.37); ω_r and n_{eff}. Another equation is needed in order to find the resonance frequency ω_r. The second equation is obtained from the slab waveguide model of cavity in the transverse z-direction.

References

[1] G.P.Agrawal and N. K. Dutta, *Semiconductor Lasers*, 2nd Edition, Chapter 6, Van Nostrand Reinhold, New York, 1993.

Appendix C: Procedures for WGM Laser Fabrication

In this appendix, there are two main sections. In the first sections, I will try to pin point some guidelines regarding important issues during each processing step that, in my experience, need to be followed in order to have a successful and reproducible fabrication run. In the second section, a detailed process flow for the two types of WGM lasers is described. The first type uses the hydrogenation to create a current blocking region, whereas the second type uses the oxide to block current.

I: Procedure for Sample Handling During Processing

1) Photolithography

Photolithography is the process of transferring a pattern from a photomask onto the surface of a substrate. The pattern is transferred via an intermediate photosensitive polymer film called photoresist. This method allows multiple devices to be patterned at once. In order to start your photolithography process, the substrate must be clean and completely dehydrated of adsorbed water to ensure good adhesion of the photoresist. Using tweezers, place wafer on the spinner chuck and make sure it is centered. You can carry the sample from one place to another in the lab by holding the sample on one side with tweezers. Once you decide what side of the sample you want the tweezers to touch, you need to choose that same side every-time you carry the sample around the lab. This way, you minimize the damage and contamination that will be caused by the tweezers touching the surface of the sample.

Optional: Using the appropriate eyedropper, pour a small puddle of HMDS (hexamethyldisilazane) on the center of the wafer and start the spinning process. Wear protective goggles in case the wafer shatters. After spinning, let the wafer air dry for a minute before proceeding with the photoresist. The HMDS is an adhesion promoter and will help the photoresist stick to the wafer. In general, if the wafer is clean and dry, the HMDS is probably not needed.

Always store your photoresist in the refrigerator to extend its lifetime when not in use. It is essential that you take your photoresist outside the refrigerator and leave it at room temperature to stabilize *four to five hours* before starting your photolithography step. Always store the photoresist portion that you want to use in an eyedropper bottle so you don't contaminate the whole photoresist bottle.

Carefully draw photoresist from its eyedropper bottle. Make sure not to let the eyedropper touch the sides of the bottle mouth, as it will pick up old dry photoresist particles, which sometimes form at the bottle lip. Any particles in the photoresist mixture will ruin the spin-on process. Form a puddle of photoresist in the center of the wafer, approximately ½ the area of the wafer; this is called *static dispensing* of the photoresist. Then, spin the wafer and dispense a drop or two of photoresist on the sample, this is called *dynamic dispensing* of the photoresist. Make sure, after the spinning process is over that the photoresist is over most of the wafer surface and that the photoresist looks uniform across the whole sample.

Note: don't worry about the edge of the sample. The photoresist will normally be thicker at the edge of the sample and will not develop properly.

2) Soft Bake

The photoresist must be cured before photolithography can proceed. To do this, the resist-coated wafer is placed on a hot plate for some time, depending on your process recipe. Always make sure to measure the surface of the hot plate with a surface thermometer and never depend on the digital indicator on the hot plate. In addition, since the temperature on the surface of the hot plate varies from one location to the other, you need to make sure that the location where you calibrate your temperature on the surface of the hot plate is marked and always used in future processing.

3) Exposing and Developing the Photoresist

The exposure of positive photoresist to a short wavelength (ultraviolet) light causes a chemical reaction, which makes the photoresist soluble in base solutions (developers). In this way, transparent locations on the photomask will correspond to areas of the photoresist being

removed. Here, I will try to note what to look for after you expose and/or develop your sample during your lithography process.

If there is insufficient light energy reaching the photoresist, the chemical reaction will be incomplete, and the photoresist will not become completely soluble. In this case, the pattern will not, or will only partially develop. This is called *underexposure*. The most common effect of *underexposure* is that pattern corners and edges, which receive slightly less light than the center of the pattern, will not 'clear' during the developing process. Thus, rounded corners such as in Fig.C.1 will be seen in an underexposed photoresist.

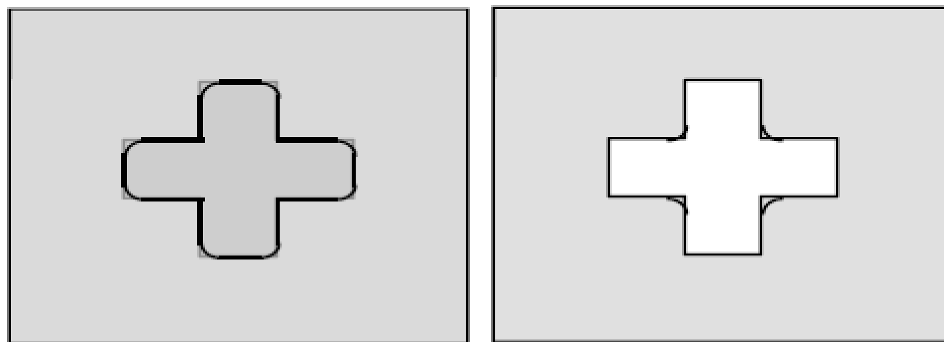

Figure C.1: Underexposed or underdeveloped photoresist pattern

If too much light energy reaches the photoresist, the chemical reaction can spread outside of the bounds of the exposed area. This is mostly caused by stray light reaching areas that are supposed to be masked. The stray light will reach the masked photoresist from the unmasked areas due to reflections and diffraction at the mask boundaries. This is called *overexposure*. The most common effect of *overexposure* can be seen in Fig.C.2. The overexposure process can lead to smaller, rounded feature sizes, and ragged edges.

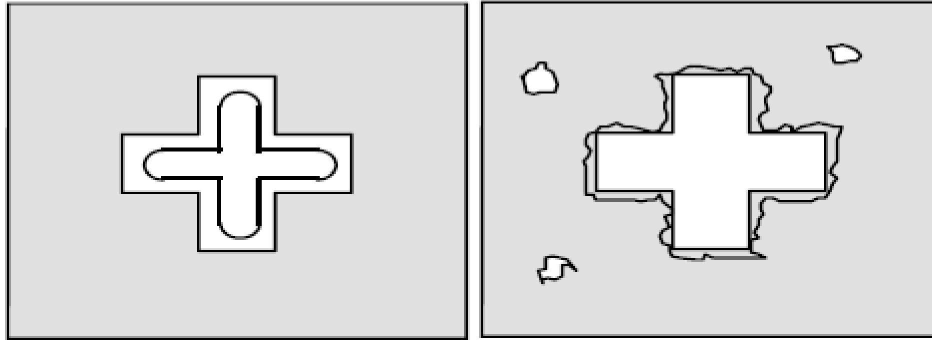

Figure C.2: Overexposure or overdeveloped photoresist pattern

The effects of the developing solution are much like the exposure. *Underdeveloping* can lead to residual photoresist in an exposed area and rounded edges, whereas *overdeveloping* can lead to smaller, rounded feature sizes, with extra pinholes and/or ragged edges in masked regions.

Determining the proper *Dose* for the specific photoresist thickness will make it easier to determine the exposure time for your lithography. This may be found by either calling the company that sells the specific photoresist and ask them about the dose required for the proper photoresist thickness or find the data sheet for the specific photoresist and determine the dose as a function of thickness. One must always recheck the exposure time, since exposure and develop times can change depending upon the type of the photoresist and the quality of the developing solution used.

The following procedure will help you calculate your exposure time:

1) Determine the specific thickness of your photoresist. This can be done by spinning your photoresist with a certain speed at a specific time and measuring your photoresist thickness from **Dektak**
2) Once you find your thickness, go to the photoresist data sheet and find out the *dose* (mJ/cm^2) required for the specific thickness.
3) Decide on the intensity (mW/cm^2) at which you want to expose your photoresist .
4) Calculate your exposure time using Eq.C1 as follows:

$$T_{exposure-calculated} = \frac{dose(mJ/cm^2)}{Intensity(mW/cm^2)} \qquad \text{(C.1)}$$

4) Wet Etching and Developing

When etching your sample using acids, always wear goggles and thick gloves. Remember to use Teflon beakers when dealing with HF or BOE. Use a dipper during your etching or developing process instead of soaking your metal tweezers inside your solution, because your tweezers may contaminate your solution.

5) Oxide Deposition

Make sure that the oxide (SiOx) insulator layer is dry before proceeding with your processing steps. If the insulator is left too long (overnight), then you need to dehydrate the sample by placing the sample on a hot plat at 200C for 5 min. However, it is always preferable to proceed with your lithography for patterning the oxide right after oxide deposition.

6) Pre-Metalization Dip Process

The pre-metallization dip is an essential step in the fabrication process. This step assures that the surface of the semiconductor is contamination free from native oxide, PECVD oxide, and any organics that maybe on the surface of the sample from previous steps in the process prior to metalization. After deposing oxide on the p-side of the sample using PECVD, you have two choices to pattern the oxide. If oxide patterning is done using ***wet etching***, then perform pre-metallization dip using hydrochloric acid (HCl acid) to remove surface oxides from both sides of the sample (p+ GaAs side and n+ GaAs substrate). There is no need to dip the sample *again* in buffered oxide acid (BOE acid) since the sample has already been dipped in BOE during oxide patterning process. However, if oxide patterning is done using ***dry etching***, then the pre-metallizaiton dip needs to be done in either HCl or BOE depending on the type of metalization being conducted.

For depositing the p-side metals, the pre-metalization dip needs to be done in HCl only. The reason for this is because BOE will etch the oxide from the p-side. However, when deposing the n-side metals, it is essential that the pre-metalization dip is done in BOE and that the p-side is covered with photoresist to avoid etching the oxide.

The reason for choosing BOE as a pre-metalization dip for the n-side when choosing dry etching to pattern the oxide is because during the oxide deposition process in the PECVD, some oxide residue might have been deposited on the backside of the sample (n+ GaAs side). During the dry etching process, the backside of the sample is mounted on a 4' Si wafer and is not exposed to the CF_4 gas in the chamber, and therefore, if not etched in BOE, this may cause your metal to peel off the backside of the sample due to poor adhesion between the oxide and the metal layers.

7) Metal Evaporation using E-beam

This process works by heating a metal in a vacuum chamber to a hot enough temperature so that the vapor pressure of the metal is significant. The wafers in the chamber are left at room temperature. By controlling the temperature and composition of the metal being evaporated, the amount of time evaporation takes place, and the temperature of the wafer, the final amount, structure, and composition of the metal on the wafer can be controlled. For metals with a low melting point, the metal is placed in a crucible and the current is sent through it. The current heats the metal, but not the crucible, so the only thing that evaporates is the metal. This will not work for metals with a high melting point, however, because higher temperatures will cause the crucible material to evaporate as well and contaminate the film on the wafer. To heat these materials, an electron beam is focused on a very small area on the metal to be evaporated. The electrons heat the metal as they collide with it and melt a small portion of the metal. The crucible never heats to the point that it contributes significantly to the vapor pressure.

E-beam evaporation will not work well for alloys and compounds. The problem arises from the fact that the different parts of the alloy or compound may have different vapor pressure for a given temperature. In a material made of two metals, the metal with the lower melting point will have a vapor pressure higher than the second metal. Therefore, more of the metal with lower melting point will be deposited on the wafer and therefore, it is not recommended.

Also, make sure to use the proper crucible type for each specific metal. For example, it was found that by using a carbon base crucible, like Graphite or Fire-Rite, to evaporate gold in the e-beam, caused the surface of the sample to be contaminated with “carbon pits”, see Fig.C.3.

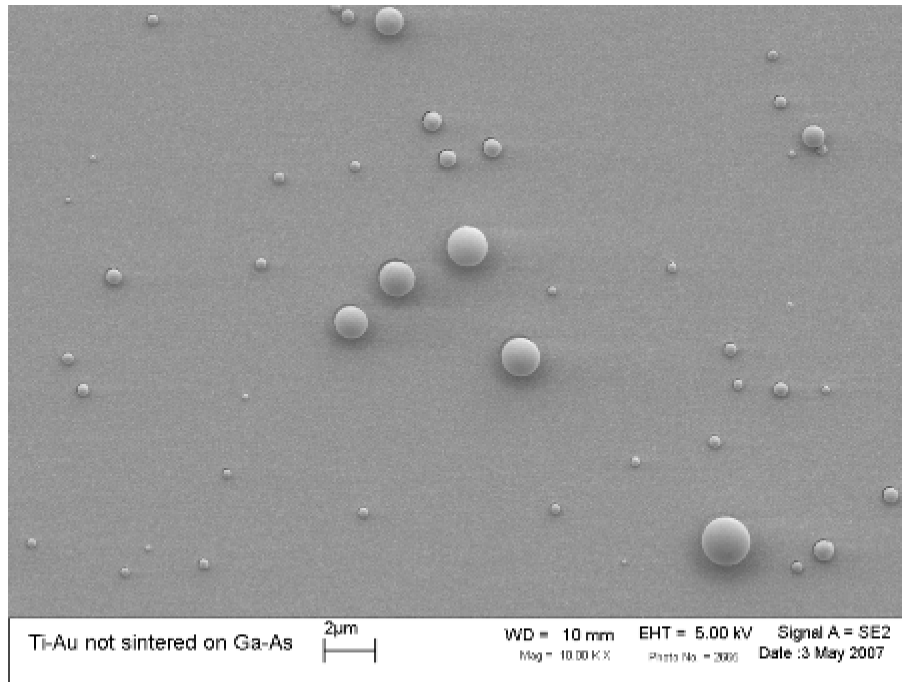

Figure C.3: An SEM image of the carbon pits on the surface of a GaAs sample after Ti/Au deposition using a carbon base crucible for the Au metal

These carbon pits will act as “shadow mask” during the cavity dry etching step, and therefore, causing the surface of the sample to look very rough and not uniform, see Fig.C.4 and Fig.C.5.

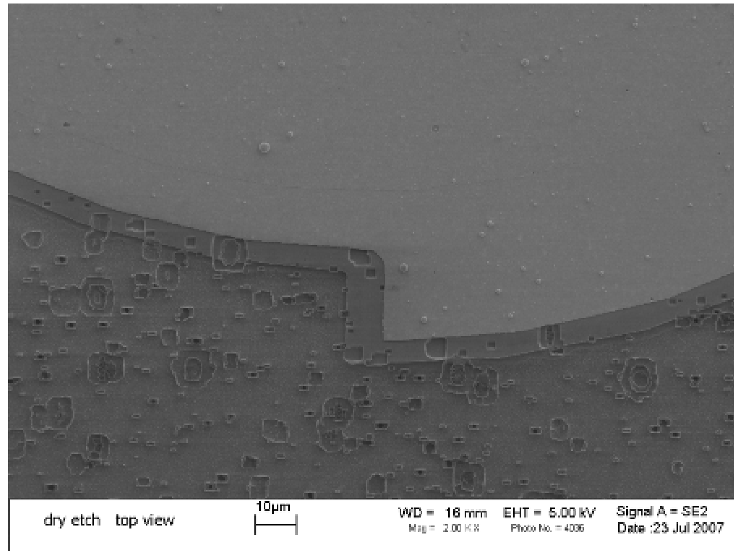

Figure C.4: SEM image (top view) of GaAs/AlGaAs spiral laser after dry etching the cavity with chlorine gas using RIE.

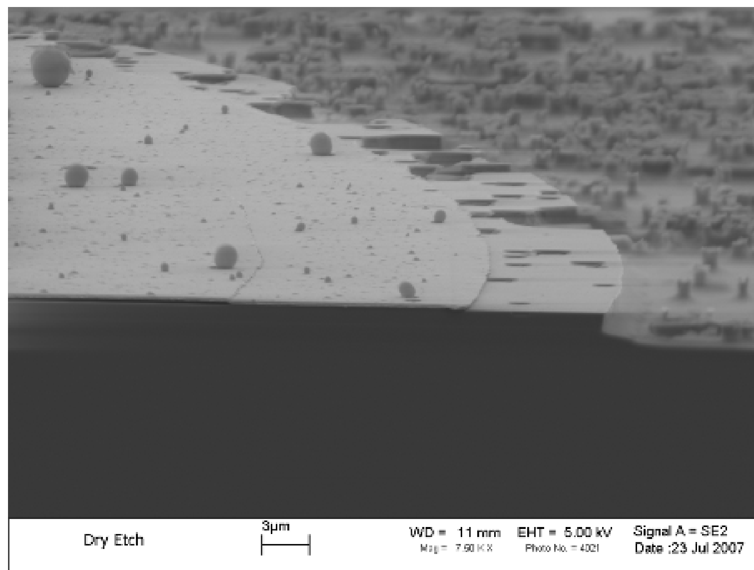

Figure C.5: SEM image (side view) of GaAs/AlGaAs spiral laser after dry etching the cavity with chlorine gas using RIE

8) Inspection

It is important to inspect your work after each step of your fabrication process. For inspection, you should use a high power microscope that is equipped with light polarization capabilities. This will help you have a better contrast between the surface of the sample and your lithography features. Also, keep in mind that if you see any of the errors indicated in Fig.C.1 and/or Fig.C.2 during your lithography process, you need to adjust the exposure and/or development times. Errors in photolithography will become permanent device errors if you don't fix them before moving on to the next step. Also, it is very helpful to carry a dummy Si sample along with your sample during processing. This way you can test, for example, your etching time using the dummy Si sample before you go ahead and etch your real sample.

II: Complete Description of Fabrication Procedures

A. The Hydrogenation Case

1) Pre-Clean Sample

a. Start with GaAs/AlGaAs laser sample.
b. Clean with Acetone (5 min) in Ultra-Sonic Bath.
c. Clean with IPA (5 min) with Ultra-Sonic Bath.
d. Rinse with DI water and blow dry with N_2.
e. Dip sample in BOE (10:1) for 90sec.
f. Rinse with DI water and blow dry with N_2.
g. **See Fig.C.6a.**

2) P-side Ohmic Contact Metal Ring

a. Use **AZ9260 Photolithography Recipe** in **Table C.1** to define the p-metal ring using **Mask F1**.
b. De-scum sample using RIE **(Photoresist Etch Recipe)** in **Table C.2** for 5-10sec.
c. Perform pre-metalization dip in HCl for 60sec.
d. Deposit Ti (30 nm)/ Au (200 nm) using E-beam Evaporation System.
e. Perform Lift-off using Acetone in Ultra-Sonic Bath.

f. Anneal contact metallurgy in RTA System or Alloying Station at 400 ºC for 4-5 min in forming gas (10% H2 in N2 balance).

g. **See Fig.C.6b.**

3) N-side Ohmic Contact Metal (deposited on n+ GaAs Substrate)

a. Rinse sample with DI water and Blow dry with N_2.

b. Spin AZ 9260 photoresist (at 4000rpm for 45sec) on top of the p+ GaAs/AlGaAs sample.

c. Perform pre-metallization dip in BOE (10:1) for 1 min

d. Rinse in DI water and Blow dry with N_2.

e. Deposit Sn (20 nm)/Au (110 nm) using E-beam Evaporation System.

f. Strip the photoresist from the p-side with Acetone, then rinse with IPA and DI water and then blow dry with N_2.

g. Anneal contact metallurgy in RTA System or Alloying Station at 390 ºC for 3 min in forming gas (10% H_2 in N_2 balance).

h. **See Fig.C.6b.**

Optional: You can anneal both metal sides at once at 400C for 4-5 min in forming gas (10% H_2 in N_2 balance)

4) P-side Electrical Isolation Layer Using Hydrogenation Process

a. Use **Mask F2** with **AZ 9260 Photolithography Recipe** in **Table C.1** to open a window for etching p+ GaAs cap layer.

b. In order to etch the p+ GaAs cap layer use either RIE (**GaAs/AlGaAs Dry Etch Recipe**) in **Table C.8** or the wet etch solution (1:H_2SO_4: 8:H_2O_2: 80:H_2O)-etch rate 0.5µm/min , **see Fig.C.6c.**

c. Strip-off the photoresist in Acetone, then rinse in IPA, DI water, and then blow dry with N_2.

d. Using PECVD (**Oxide Deposition Recipe**) in **Table C.6**, deposit 200 nm of SiOx over entire surface of epilayer**, see Fig.C.6d.**

i. For loading the sample in PECVD, place sample on 4" Si wafer

ii. Leave sample inside the chamber for 5min before deposition (for temp stabilization)

e. Use **Mask F2** with AZ 9260 photoresist again to open a window in the oxide for hydrogenation process. The rest of the device will be insulated from the hydrogenation process because oxide will act as a blocking mask, **see Fig.C.6e.**

f. See **Table C.3** for the **Hydrogenation Recipe**.

5) P-Side Metal Pad Formation

a. Use RIE or SAMCO **(Oxide Etch Recipe)** in **Table C.4 or Table C. 5**, respectively, to remove the oxide everywhere.

b. Use **Mask F3** with **AZ9260 Photolithogrphy Recipe** in **Table C.1** to open a window for the metal deposition.

c. Deposite (300nm-400nm) Au using E-beam Evaporation System.

d. Use Acetone with Ultra-Sonic Bath to do Lift-off of the metal

e. Strip-off the photoresist using Acetone and IPA then rinse with DI water and blow dry with N_2.

f. **See Fig.C.6f.**

6) Formation of Laser Cavity

a. Clean with Acetone and IPA (5min each) no Ultra Sonic Bath necessary.

b. Rinse with DI water and blow dry with N_2.

c. Use **AZ9260 Photolithography Recipe** in **Table C.1** to define laser cavity using **Mask F4**.

d. Execute "dry" etching step using Trion RIE System to etch laser cavity, see **"Notes on RIE Dry Etch Process"**.

e. Load sample in RIE and use **GaAs/AlGaAs Dry Etch Recipe** in **Table C.8**.

f. **See Fig.C.6g**.

7) Oxidation smoothing and surface passivation of the Cavity

a. Strip-off the AZ 9260 photoresist with Acetone and IPA.

b. Rinse with DI water and blow dry with N_2.

c. Load sample in PECVD and deposit (150nm-200nm) a nitride layer using PECVD (**Nitride Deposition Recipe**) in **Table C.7**.

d. Use either **Mask F2 or Mask F3** to open a window in the oxide layer by dry etching in either RIE or SAMCO.

e. **See Fig.C.6h**.

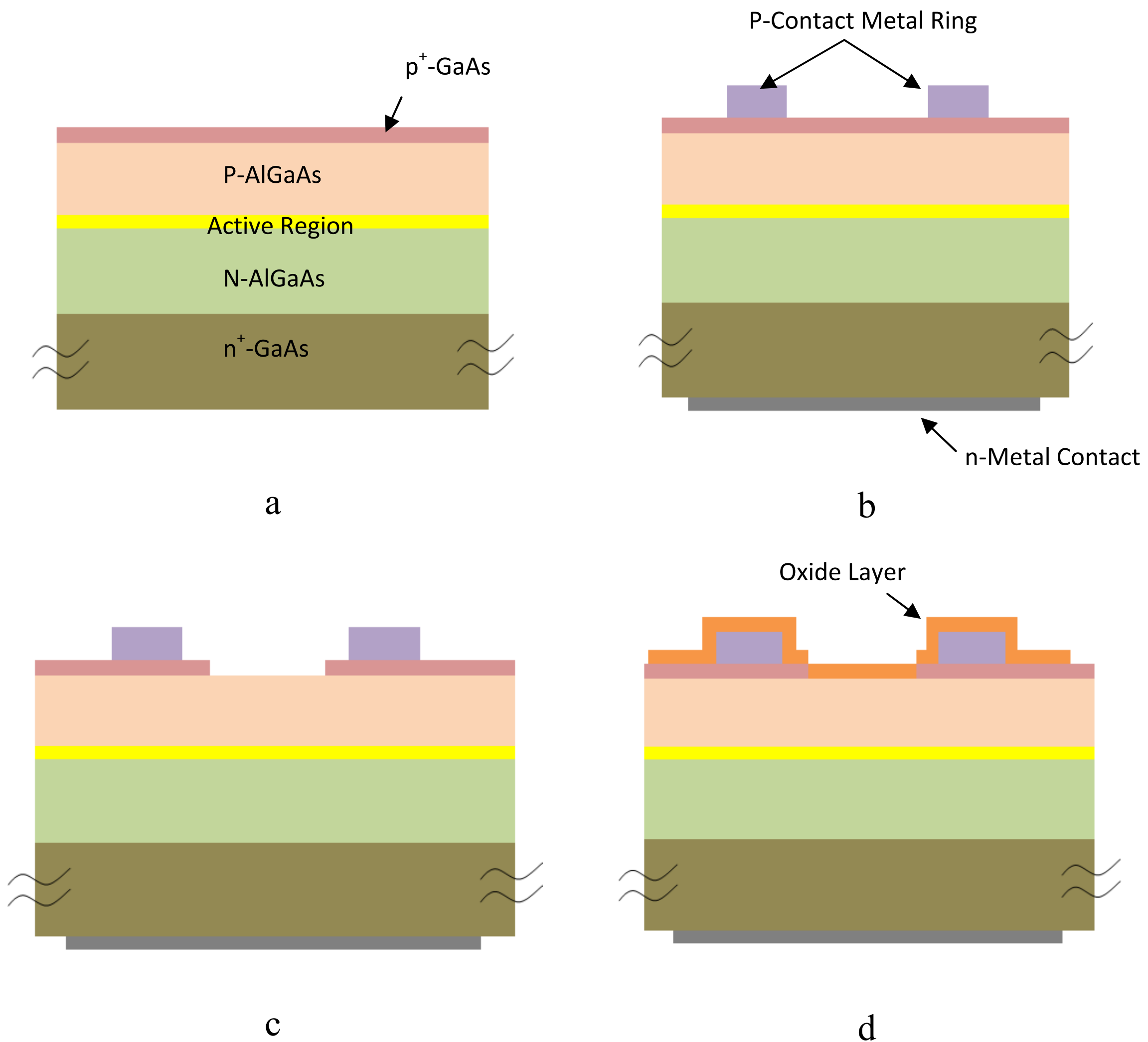

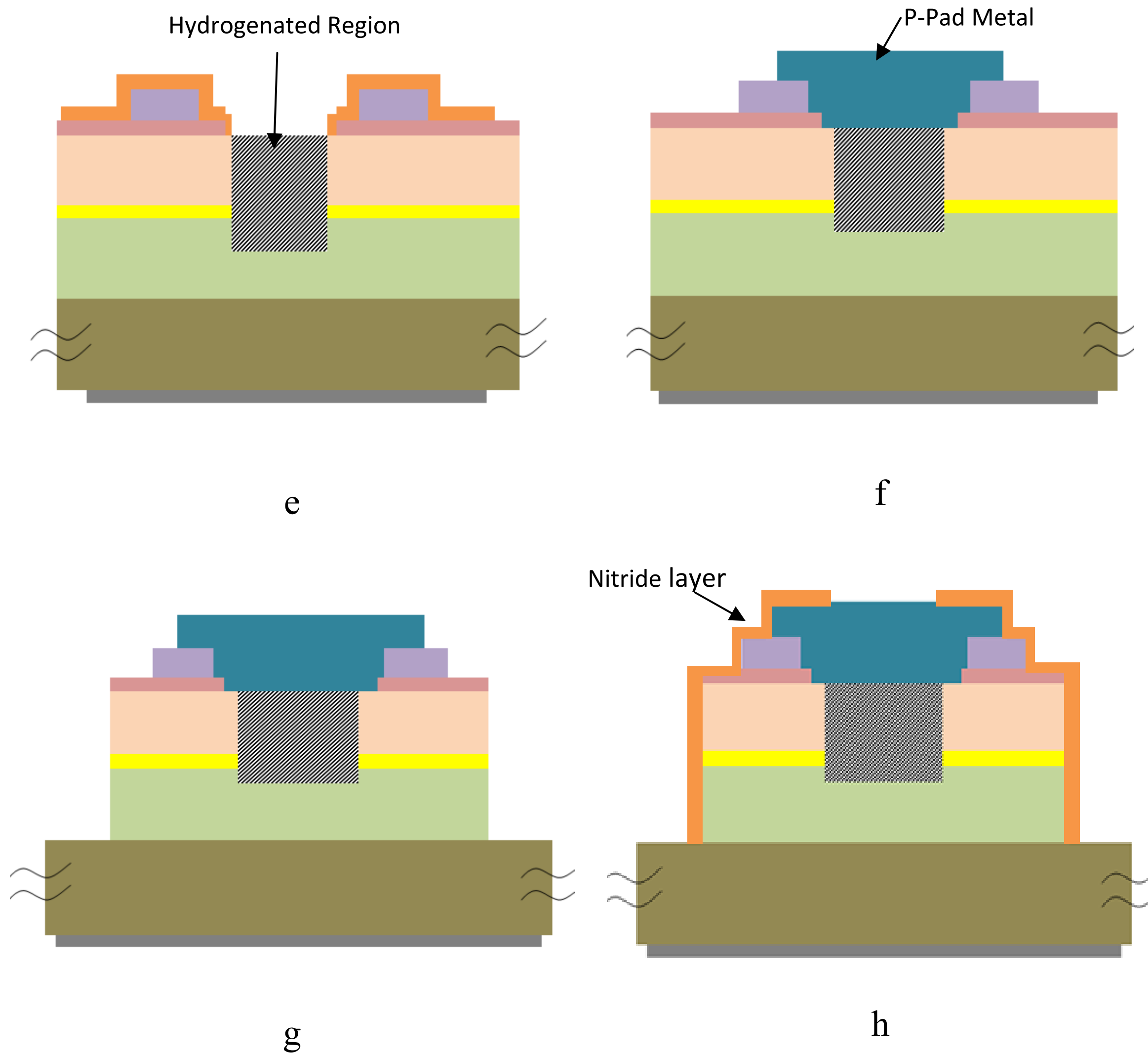

Figure C.6: shows the fabrication process flow of the WGM laser for the Hydrogenation case.

Figure C.7 shows the complete fabricated WGM laser device where hydrogenation is used as a method to block current and carriers.

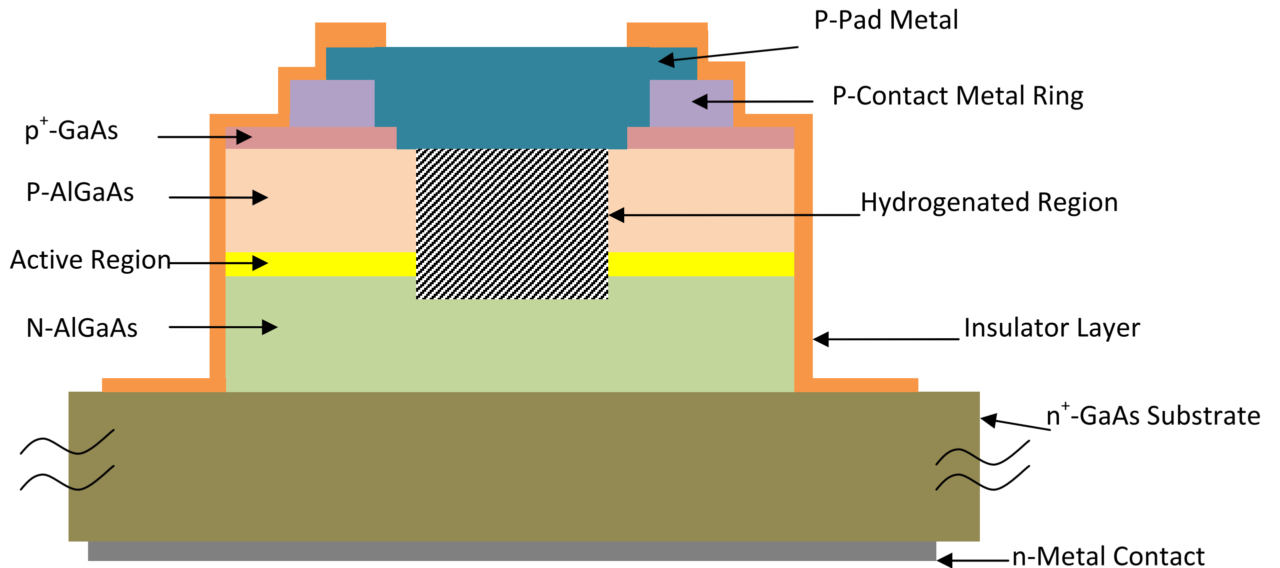

Figure C.7: Shows the Complete Fabricated device using hydrogenation to form the current blocking region

B. The Non Hydrogenated Case

1. Pre-Clean Sample

a. Start with GaAs/AlGaAs laser sample.
b. Clean with Acetone (5 min) in Ultra-Sonic Bath.
c. Clean with IPA (5 min) with Ultra-Sonic Bath.
d. Rinse with DI water and blow dry with N_2.
e. Dip sample in BOE (10:1) for 90sec.
f. Rinse with DI water and blow dry with N_2.
g. **See Fig.C.8a.**

2. P-side Ohmic Contact Metal Ring

a. Use **AZ9260 Photolithography Recipe** in **Table C.1** to define the p-metal ring using **Mask F1**.
b. De-scum sample using RIE (**Photoresist Etch Recipe**) in **Table C.2** for 5-10sec.
c. Perform pre-metalization dip in HCl for 60sec.
d. Deposit Ti (30 nm)/ Au (200 nm) using E-beam Evaporation System.

e. Perform Lift-off using Acetone in Ultra-Sonic Bath.
f. Anneal contact metallurgy in RTA System or Alloying Station at 400 ºC for 4-5 min in forming gas (10% H2 in N2 balance).
g. **See Fig.C.8b.**

3. **N-side Ohmic Contact Metal (deposited on n+ GaAs Substrate)**
   a. Rinse sample with DI water and Blow dry with N_2.
   b. Spin AZ 9260 photoresist (at 4000rpm for 45sec) on top of the p+ GaAs/AlGaAs sample.
   c. Perform pre-metallization dip in BOE (10:1) for 1 min
   d. Rinse in DI water and Blow dry with N_2.
   e. Deposit Sn (20 nm)/Au (110 nm) using E-beam Evaporation System.
   f. Strip the photoresist from the p-side with Acetone, then rinse with IPA and DI water and then blow dry with N_2.
   g. Anneal contact metallurgy in RTA System or Alloying Station at 390 ºC for 3 min in forming gas (10% H_2 in N_2 balance).
   h. **See Fig.C.8b.**

Optional: You can anneal both metal sides at once at 400C for 4-5 min in forming gas (10% H_2 in N_2 balance)

4. **P-side Electrical Isolation Layer Using Oxide**
   a. Use **Mask F2** with **AZ 9260 Photolithography Recipe** in Table C.1 to open a window to etch p+ GaAs cap layer.
   b. In order to etch the p+ GaAs cap layer use either RIE (**GaAs/AlGaAs Dry Etch Recipe**) in **Table C.8** or the wet etch solution (1:H_2SO_4: 8:H_2O_2: 80:H_2O)-etch rate 0.5µm/min , **see Fig.C.8c.**
   c. Strip-off the photoresist in Acetone, then rinse in IPA, DI water, and then blow dry with N_2.
   d. Using PECVD (**Oxide Deposition Recipe**) in **Table C.6**, deposit 200 nm of SiO_x over entire surface of epilayer**, see Fig.C.8d.**

i. For loading the sample in PECVD, place sample on 4” Si wafer

ii. Leave sample inside the chamber for 5min before deposition (for temp stabilization)

e. Use **Mask F5** with AZ 9260 photoresist to pattern oxide into a filled circle. This mask has features with larger diameter than the openings in mask F2.

f. Dry etch the oxide using RIE or SAMCO **(Oxide Etch Recipe)** in **Table C.4 or Table C.5**, respectively.

g. **See Fig.C.8e.**

5. P-Side Metal Pad Formation

a. Use RIE or SAMCO **(Oxide Etch Recipe)** in **Table C.4 or Table C.5**, respectively, to remove the oxide everywhere.

b. Use **Mask F3** with **AZ9260 Photolithogrphy Recipe** in **Table C.1** to open a window for the metal deposition.

c. Deposite (300nm-400nm) Au using E-beam Evaporation System.

d. Use Acetone with Ultra-Sonic Bath to do Lift-off of the metal

e. Strip-off the photoresist using Acetone and IPA then rinse with DI water and blow dry with N_2.

f. **See Fig.C.8f.**

6. Formation of Laser Cavity

a. Clean with Acetone and IPA (5min each) no Ultra Sonic Bath necessary.

b. Rinse with DI water and blow dry with N_2.

c. Use **AZ9260 Photolithography Recipe** in **Table C.1** to define laser cavity using **Mask F4**.

d. Execute “dry” etching step using Trion RIE System to etch laser cavity, see **“Notes on RIE Dry Etch Process”**.

e. Load sample in RIE and use **GaAs/AlGaAs Dry Etch Recipe** in **Table C.8**.

f. **See Fig.C.8g.**

7. Oxidation smoothing and surface passivation of the Cavity

a. Strip-off the AZ 9260 photoresist with Acetone and IPA.

b. Rinse with DI water and blow dry with N_2.

c. Load sample in PECVD and deposit (150nm-200nm) nitride layer using PECVD (**Nitride Deposition Recipe**) in **Table C.7.**

d. Use either **Mask F2 or Mask F3** to open a window in the oxide layer by dry etching in either RIE or SAMCO.

e. **See Fig.C.8h**.

a

b

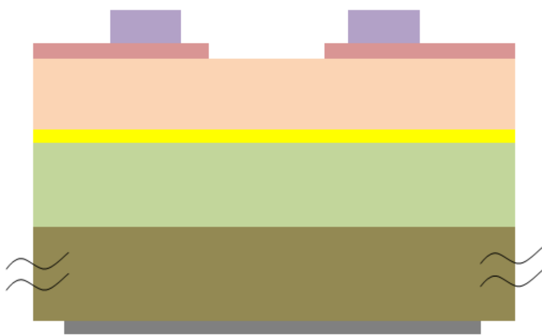

c

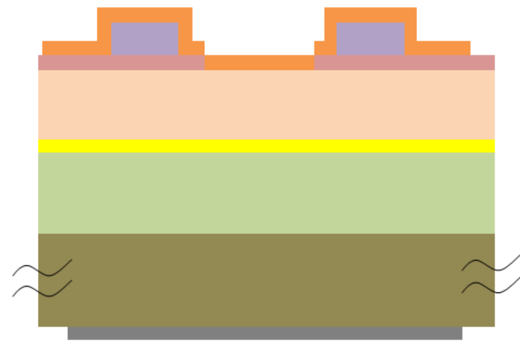

d

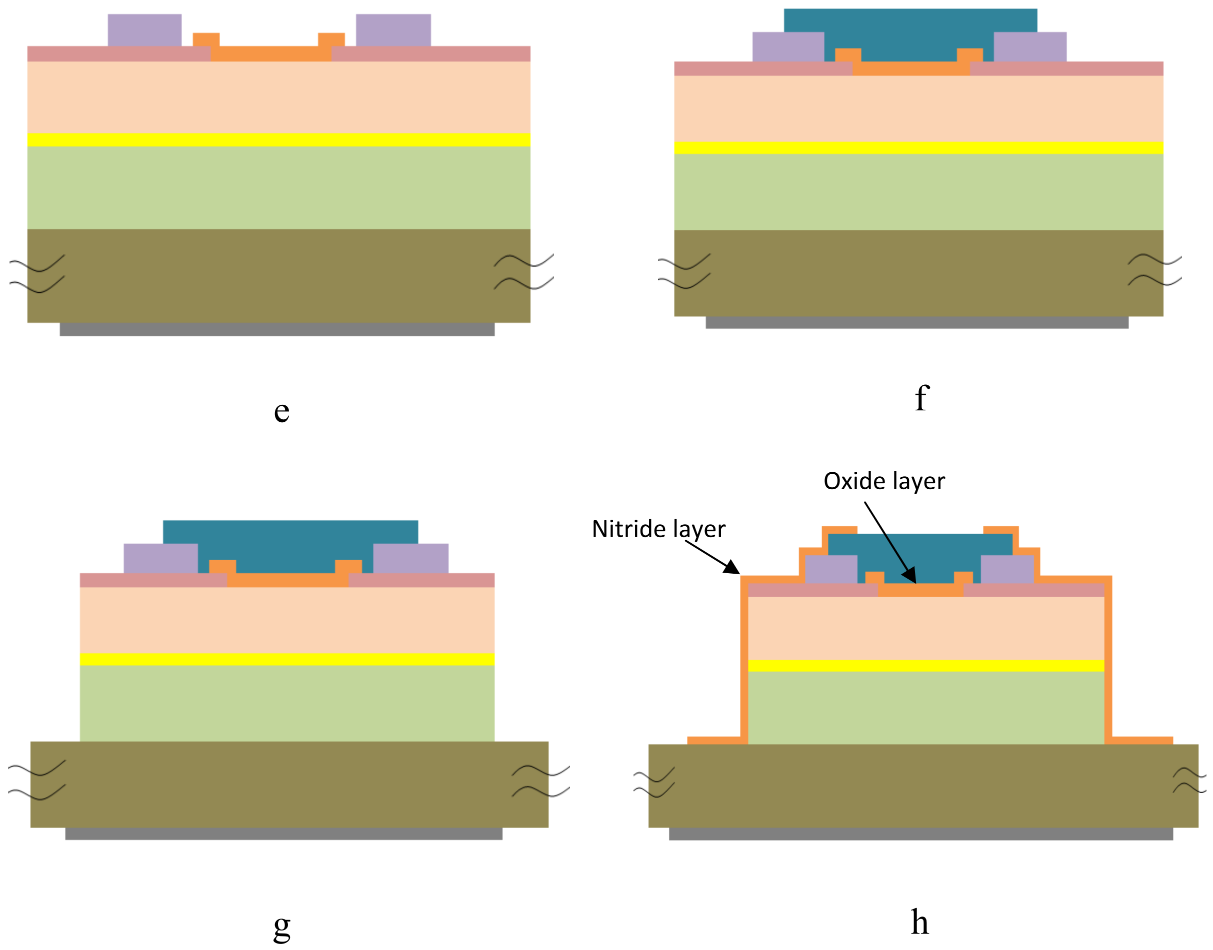

Figure C.8: shows the fabrication process flow of the WGM laser for the non-Hydrogenated case

Figure C.9 shows the complete fabricated WGM laser device where oxide is used as a method to block current and carriers.

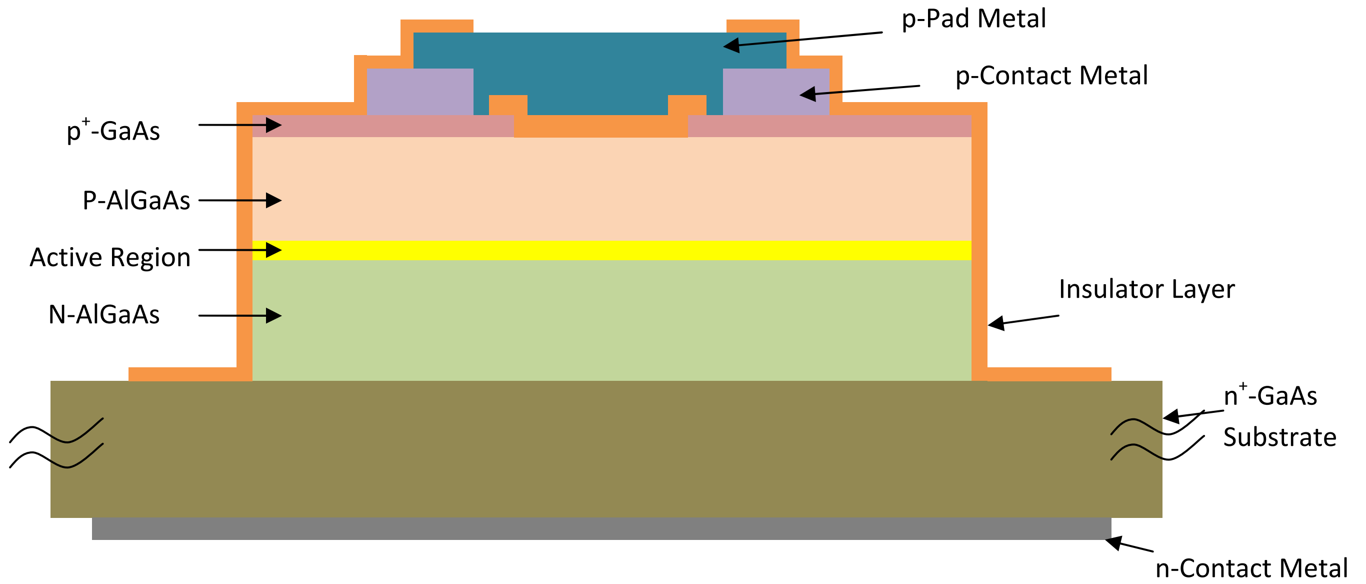

Figure C.9: Shows the Complete Fabricated device using Oxide to form the current blocking region

Table C.1: AZ9260 Photolithography Recipe

Parameter	Value
Spin Speed (rpm)	3000 for 45 sec (approx. 8µm thick)
Soft Bake (C)	115C for 3.5 min
Exposure(mW/cm2)	12.0 for 35sec
Developer (1AZ 400K :3 H2O DI)	Approx. 4min
Hard Bake (C)	120C for 5min

Table C.2: The Photoresist Etch Recipe

Parameter	Value
Chamber Pressure	30 mTorr
ICP	250 W
RIE	100 W
He back flow Pressure	8 Torr
O2	45 sccm
Temp of Chuck	20C
Electrostatic Chuck (ON)	Vdc=600V , $I_{Leakage}$= 4um
Etch Rate	Approx. 1 µm/min

Table C.3: The PECVD Hydrogenation Recipe

Parameter	Value
Chamber Pressure	750 mTorr
ICP	175 W
RIE	50 W
Temp of Chuck	250C
Ammonia (NH3) Flow Rate	220 sccm
Time (min)	15min @ 250C
Cool Down Process	Cool down to 100C while plasma is on before unloading the sample

Table C.4: The RIE Oxide Etch Recipe

Parameter	Value
Chamber Pressure	50 mTorr
ICP	350 W
RIE	50 W
He back flow Pressure	8 Torr
CF4	50 sccm
Temp of Chuck	20C
Electrostatic Chuck (ON)	Vdc=600V , $I_{Leakage}$= 4um
Etch Rate	Approx. 570A/min

Table C.5: The SAMCO Oxide Etch Recipe

Parameter	**Value**
Chamber Pressure	50-100 mTorr
Power	100 W
CF4 Flow Rate	10 sccm
Etch Rate	Approx. 1500Å/min

Table C.6: The PECVD Oxide Deposition Recipe

Parameter	**Value**
Chamber Pressure	900 mTorr
ICP Power	175 W
RIE Power	50 W
Temperture	355 C
Silane (SiH4) 2% flow rate	300 sccm
Nitrous Oxide (N2O) flow rate	71 sccm
Deposition Rate	450-500 A/min

Table C.7: The PECVD Nitride Deposition Recipe.

Parameter	**Value for Nitride**
Chamber Pressure	600 mTorr
ICP Power	175W
RIE Power	50W
Temperature	350C
Silane (SiH4) 2% flow rate	600sccm
NH3 flow rate (nitride)	15sccm
Deposition Rate	420A/min

Table C.8: The RIE GaAs/AlGaAs Dry Etch Recipe

Parameter	Value
Chamber Pressure	10 mTorr
ICP	320 W
RIE	50 W
He back flow Pressure	9 Torr
BCl3 Flow	20 sccm
Cl2 Flow	3 sccm
Temp of Chuck	20 C
Electrostatic Chuck (ON)	Vdc=600V , $I_{Leakage}$= 4um
Etch Rate	Approx. 0.85μm/min

Notes on RIE Dry Etch Process:

Use a **Thin** 4” **Si wafer** that has a very **Low Resistivety.** The specification of the Si wafer used in this process is as follows:

1) CZ/100/Boron/P+ type/Resis 0.0050- 0.0100 (ohm-cm) with EPI film Boron/p-type/ Thick 12.35 – 13.65 um/Resis 8.5000 – 11.5000 (ohm-cm)
2) Place the 4” Si wafer on a hot plate at 90C
3) Apply **CoolGrease Thermal Paste** on the surface of the 4” Si wafer to a surface area slightly larger than the sample (notice: the coolgrease will start to wet).
4) Mount laser sample on Si wafer (**make sure that the thermal paste cover the whole back side of the sample but not too much**).
5) Remove any thermal paste residue with a razor blade.

Appendix D: Definition of Optical Confinement Factor

In this appendix, analysis of the optical confinement in the transverse direction, Γ_y, is presented. This appendix follows the work done in appendix A. The transverse confinement factor for the three-layer slab waveguide consists of the fraction of the optical energy that is contained in the active region, *a*. Therefore, *a* cannot be ignored in this analysis. Note that we were able to ignore the active region, *a*, in our electromagnetic analysis for the symmetric three layer slab waveguide in appendix A without affecting the analysis.

The confinement factor is defined as the ratio of the power flow per unit area in the active region to the total power flow per unit area within and outside the active layer. The confinement factor derivation was done using [1].

$$\Gamma_y = \frac{P_{core}}{P_{total}} \qquad \text{(D.1)}$$

The time averaged power flow along the axial direction is determined from

$$P = \frac{1}{2}\int_S \mathrm{Re}\left(\vec{E} \times \vec{H}^*\right) \cdot d\vec{S} \qquad \text{(D.2)}$$

Where

$$\begin{cases} \vec{E} = E_x(y) \cdot \hat{a}_x \\ \vec{H} = H_y(y) \cdot \hat{a}_y + H_z(y) \cdot \hat{a}_z \\ d\vec{S} = dS \cdot \hat{a}_z \end{cases} \qquad \text{(D.3)}$$

To calculate P_{core} , we substitute Eq.(D.3) into Eq.(D.2), and therefore, P_{core} can be written as:

$$P_{core} = \frac{1}{2}\int_0^1 \int_{=\frac{a}{2}}^{\frac{a}{2}} E_x(y) \cdot H_y(y) dx dy = \frac{1}{2}\int_0^1 dx \int_{\frac{-a}{2}}^{\frac{a}{2}} E_x(y) \cdot H_y(y) dy = \int_0^{\frac{a}{2}} E_x(y) \cdot H_y(y) dy \quad \text{(D.4)}$$

Similarly, P_{total} can be written as

$$P_{total} = \frac{1}{2}\left[\int_{\frac{-b}{2}}^{\frac{b}{2}} E_x(y)\cdot H_y(y)dy + 2\int_{\frac{b}{2}}^{\infty} E_x(y)\cdot H_y(y)dy\right] = \left[\int_{0}^{\frac{b}{2}} E_x(y)\cdot H_y(y)dy + \int_{\frac{b}{2}}^{\infty} E_x(y)\cdot H_y(y)dy\right] \quad \text{(D.5)}$$

According to [1] we can write $H_y(y) = F\cdot E_x(y)$, where F is a constant. Substituting Eq(s).(D.4) and (D.5) into Eq.(D.1), we can express the optical confinement in the transverse direction as follows:

$$\Gamma_y = \frac{\int_0^{\frac{a}{2}} |E_x(y)|^2 dy}{\int_0^{\frac{b}{2}} |E_x(y)|^2 dy + \int_{\frac{b}{2}}^{\infty} |E_x(y)|^2 dy} = \frac{\int_0^{\frac{a}{2}} A^2\cos^2(\chi y)dy}{\int_0^{\frac{b}{2}} A^2\cos^2(\chi y)dy + \int_{\frac{b}{2}}^{\infty} C^2 e^{-2\gamma\cdot y}dy} \quad \text{(D.6)}$$

Following the analysis in appendix A, see Fig.A.5, we know that the boundary condition between region I and region II require that the tangential components of both electric and magnetic fields be continuous [2]. Therefore, the following can be stated:

$$E_{x_regionI}(y) = E_{x_regionII}(y) \quad \text{at} \quad y=b/2 \quad \text{(D.7)}$$

$$\frac{\partial E_{x_regionI}(y)}{\partial y} = \frac{\partial E_{x_regionII}(y)}{\partial y} \quad \text{at} \quad y=b/2 \quad \text{(D.8)}$$

Using equation (D.7) at y=b/2, we can write $A\cos(\chi\frac{b}{2}) = Ce^{-\gamma\cdot\frac{b}{2}}$ and, therefore, we can find C to be

$$C = A\cos(\chi\frac{b}{2})\cdot e^{\gamma\cdot\frac{b}{2}} \quad \text{(D.9)}$$

Substituting equation (D.9) into (D.6), we get the following

$$\Gamma_y = \frac{\int_0^{\frac{a}{2}} \cos^2(\chi y)dy}{\int_0^{\frac{b}{2}} \cos^2(\chi y)dy + \int_{\frac{b}{2}}^{\infty} \cos^2(\chi \frac{b}{2}) \cdot e^{\gamma \cdot b} \cdot e^{-2\gamma \cdot y} dy} \qquad \text{(D.10)}$$

Evaluating the integrals in Eq.(D.10), yields the following equation for the optical confinement in Eq.(D.11)

$$\Gamma_y = \frac{\int_0^{\frac{a}{2}} \frac{1+\cos(2\chi y)}{2} dy}{\int_0^{\frac{b}{2}} \frac{1+\cos(2\chi y)}{2} dy + \cos^2(\chi \frac{b}{2}) \cdot e^{\gamma b} \int_{\frac{b}{2}}^{\infty} e^{-2 \cdot \gamma \cdot y} dy} = \frac{\frac{1}{4}\left[a + \frac{1}{\chi}\sin(\chi a)\right]}{\frac{1}{4}\left[b + \frac{1}{\chi}\sin(\chi b)\right] + \cos^2(\chi \frac{b}{2}) \cdot e^{\gamma b}\left[\frac{1}{2\gamma} \cdot e^{-\gamma \cdot b}\right]}$$

$$\Gamma_y = \frac{\frac{1}{4} \cdot a \cdot \left[1 + \frac{\sin(\chi a)}{(\chi a)}\right]}{\frac{1}{4} \cdot b \cdot \left[1 + \frac{\sin(\chi b)}{(\chi b)}\right] + \frac{1}{4 \cdot \gamma}\left[1 + \cos(\chi b)\right]} \qquad \text{(D.11)}$$

The expression in Eq.(D.11) can be simplified as follows:

We know that

$$\sin(\chi b) = 2\cos\left(\frac{\chi b}{2}\right)\sin\left(\frac{\chi b}{2}\right) \qquad \text{(D.12)}$$

$$\cos(\chi b) = \cos^2\left(\frac{\chi b}{2}\right) - \sin\left(\frac{\chi b}{2}\right) \qquad \text{(D.13)}$$

From Appendix A, the characteristic equation is expressed as:

$$\tan\left(\frac{\chi b}{2}\right) = \frac{\gamma}{\chi} \qquad \text{(D.14)}$$

Using trigonometric identity and Eq.(D.14), we obtain the following:

$$\cos^2\left(\frac{\chi b}{2}\right) = \frac{1}{1+\tan^2\left(\frac{\chi b}{2}\right)} = \frac{\chi^2}{\chi^2+\gamma^2} \tag{D.15}$$

$$\sin^2\left(\frac{\chi b}{2}\right) = \frac{\tan^2\left(\frac{\chi b}{2}\right)}{1+\tan^2\left(\frac{\chi b}{2}\right)} = \frac{\gamma^2}{\chi^2+\gamma^2} \tag{D.16}$$

$$\sin(\chi b) = \frac{2\chi\gamma}{\chi^2+\gamma^2} \tag{D.17}$$

$$\cos(\chi b) = \frac{\chi^2-\gamma^2}{\chi^2+\gamma^2} \tag{D.18}$$

Substituting Eq.(s) (D.15) through (D.18) in the denominator of Eq.(D.11) and simplifying , we can obtain the following:

$$\left(\frac{1}{4}b+\frac{1}{4\gamma}\right)+\frac{1}{4}\left[\frac{\sin(\chi b)}{\chi}+\frac{\cos(\chi b)}{\gamma}\right] = \left(\frac{1}{4}b+\frac{1}{4\gamma}\right)+\frac{1}{4}\left[\frac{2\gamma}{\chi^2+\gamma^2}+\frac{1}{\gamma}\frac{\chi^2-\gamma^2}{\chi^2+\gamma^2}\right]$$

$$\left(\frac{1}{4}b+\frac{1}{4\gamma}\right)+\frac{1}{4\gamma}\left[\frac{2\gamma^2+\chi^2-\gamma^2}{\chi^2+\gamma^2}\right] = \frac{1}{4}b+\frac{1}{4\gamma}+\frac{1}{4\gamma} = \frac{b}{4}+\frac{1}{2\gamma} \tag{D.19}$$

Substituting Eq.(D.19) into the denominator of Eq.(D.11) yields the following:

$$\Gamma_y = \frac{\frac{a}{4}\left[1+\frac{\sin(\chi a)}{\chi a}\right]}{\frac{b}{4}+\frac{1}{2\gamma}} = \frac{\frac{a}{2}\left[1+\frac{\sin(\chi a)}{\chi a}\right]}{\frac{b}{2}+\frac{1}{\gamma}} \tag{D.20}$$

For a→0 then $\frac{\sin(\chi a)}{\chi a} = 1$, Eq.(D.11) can be simplified and written as:

$$\Gamma_y = \frac{\frac{a}{2}(1+1)}{\frac{b}{2}+\frac{1}{\gamma}} = \frac{a}{\frac{b}{2}+\frac{1}{\gamma}} \qquad \text{(D.21)}$$

The thickness of the optical confinement layer (OCL) is represented by *b* and the thickness of the quantum well (QW) layer is represented by *a*. In our material structure, see table 3.1, *b*=0.26 μm and *a*=10 nm. Also, the emission wavelength of our laser device is λ_o=795 *nm* and, therefore, $k_0 = \frac{2\pi}{\lambda_o} = 7.9\times10^4 cm^{-1}$. The dielectric constant (static) at 300K for $Al_{0.85}Ga_{0.15}As$ and GaAs are ε_1=10.5 and ε_2=12.9, respectively [4]. Using appendix A, we have calculated γ to be 1.12×10^5 cm^{-1} for m=0 mode. Using Eq.(D.21), we can calculate the optical confinement in the transverse direction to be Γ_y=0.047.

Next, we will look at how the optical confinement factor along the y-direction changes relative to the thickness of the optical confinement layer. Figure D.1 shows a plot of the normalized optical confinement factor along the y-direction in universal form as a function of the normalized optical confinement layer thickness *b* for Eq(s).(D.21). In order to normalize Eq.(D.21), we use the following equations [3]:

$$\Gamma_{y_norm}(b) = \frac{\Gamma_y(b)}{\left(\frac{2\pi}{\lambda_o}\sqrt{\varepsilon_2-\varepsilon_1}\right)\cdot a} \qquad \text{(D.22)}$$

$$b_{normalized} = \frac{b}{\left(\frac{\lambda_o}{2\pi\sqrt{\varepsilon_2-\varepsilon_1}}\right)} \qquad \text{(D.23)}$$

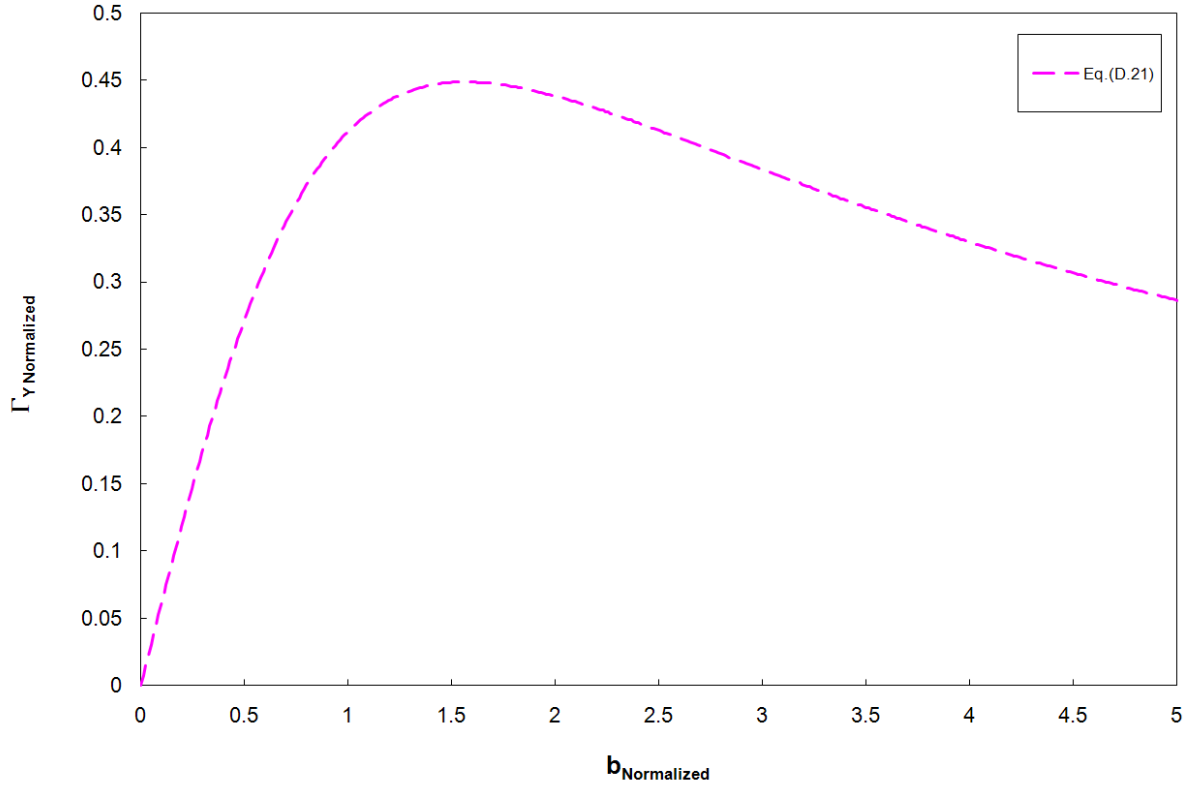

Figure D.1. Shows normalized optical confinement factor along the y-direction and its dependence on the normalized optical confinement layer thickness

The benefit of Fig.D.1 is that we can find the value of the optical confinement at any thickness *b*. Also, notice from the plot that the maximum value of the normalized optical confinement factor along the y-direction occurs approximately at $\Gamma_{y-norm} \approx 0.45$. If we plug this value in Eq.(D.22) and calculate for the optical confinement, we find out that $\Gamma_y \approx 0.05$ which is very close to the calculated value using Eq.(D.21).

References:

[1] Class notes from Dr. Safai-Jazi, Virginia Tech.

[2]Cassy H. C. and Panish M.B. 1978 *Hetrostructure Laser. Part A: Fundamental Principles.*

[3] L. V. Asryan and R. A. Suris, “Inhomogeneous line broadening and the threshold current density of a semiconductor quantum dot laser”, *Semicon. Sci. Technol.* vol. 11 (1996).

[4] http://www.ioffe.rssi.ru/SVA/NSM/Semicond/index.html

Appendix E: Design Parameters for WGM Lasers

In this appendix, the complete design of the mask is presented. We start by describing the design of the mask layout. Then, a table is presented showing the changes in the different parameters of the WGM lasers.

1. The Mask design

A side view of the different layers in the laser structure with the important parameters in the mask layout design is shown in Fig.E.1. These parameters are defined as follows:

d_{cavity}: The diameter of the etched cavity.

d_{pp}: The diameter of the p-pad metal.

d_{SW}^{out}: The outer diameter of the p-contact metal ring.

d_{SW}^{in}: The inner diameter of the p-contact metal ring.

d_{ox}: The diameter of the oxide mask window for Hydrogenation.

δ_{ME}: The separation between the p-contact metal and the edge of the cavity.

δ_{ox}: The separation between the p-contact metal ring and the oxide mask window.

δ_{SW}: The width of the p-contact metal ring.

δ_{pp}: The separation between the p-contact metal ring and the p-contact metal pad.

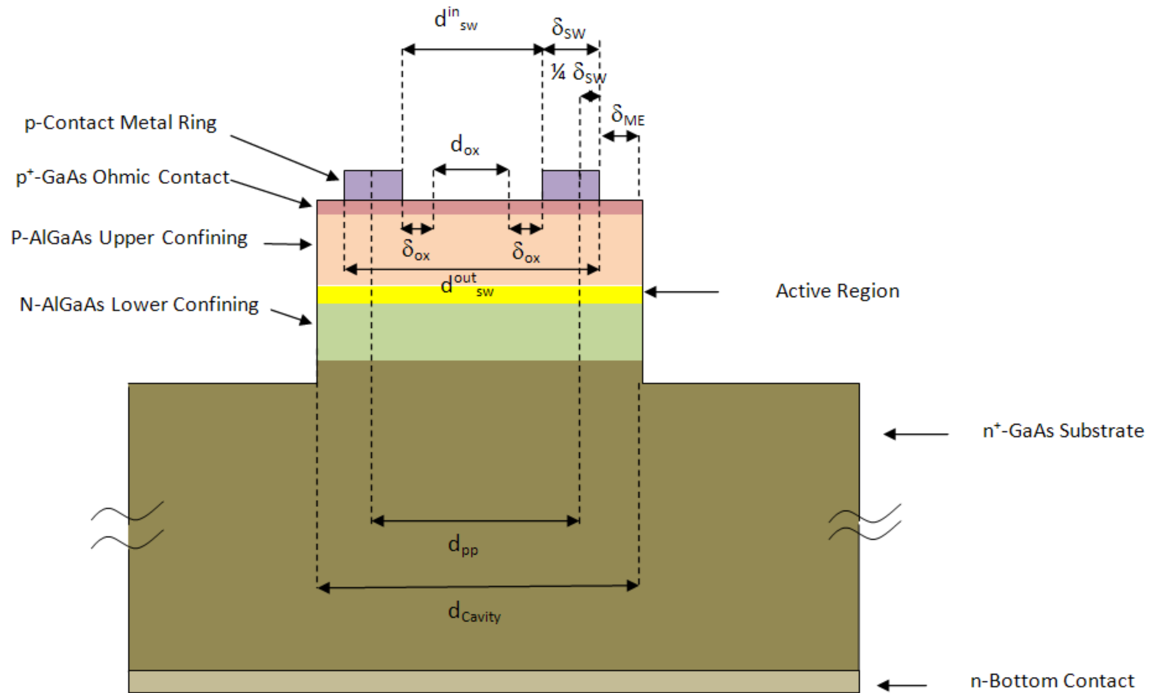

Figure E.1: A side-view of the laser structure showing the important parameters in the mask layout design.

In the mask design there are three types of device structures. The first type is conventional WGM laser structure i.e. a micropillar structure. This device structure is chosen to optimize the performance of the WGM laser without the influence of the light outcoupler. The second type is spiral laser structure. This device structure is chosen to investigate the effect of the outcopler on the optical performance of WGM lasers. And finally, the third type of device structure is partial circles which are used to modify the conventional cleaved cavity method to cover WGM lasers. All three types of devices are shown in Fig E.2, respectively.

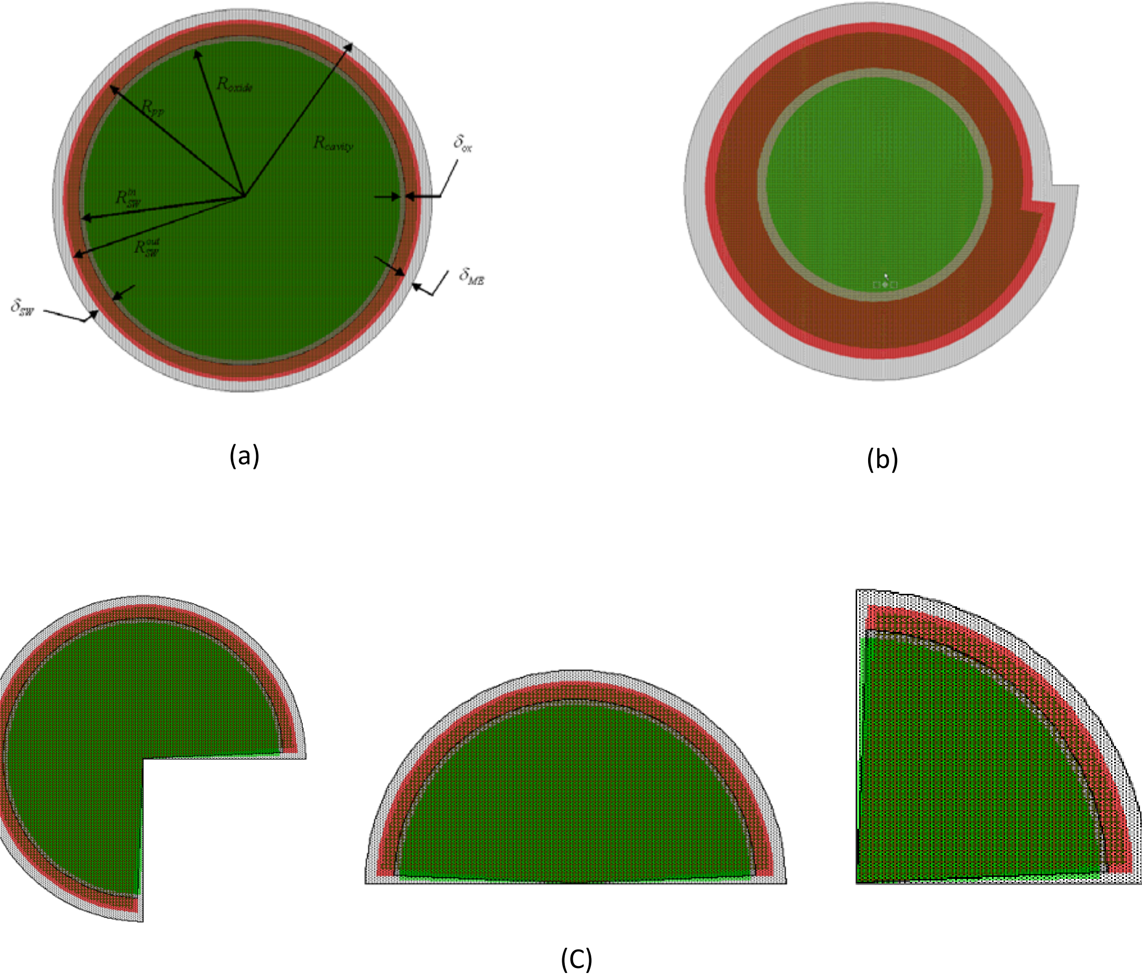

Figure E.2: (a) Shows the conventional WGM device structure, (b) shows the spiral device structure, and (c) shows the partial micropillar structures.

Figure E.3 shows the complete mask design. As you can see, there are six different fields on the mask. The three dark fields are used to create openings for the metal ring deposition, the metal pad deposition, and the oxide window for the hydrogenation process. The other three light fields are used to create the mesa etch for the optical cavity, the oxide field for blocking current and the option to have an n-metal top contact in case we decide to fabricate the laser devices using GaN on sapphire substrate. In this case, the sapphire substrate is an insulator, and therefore, it is necessary to deposit the n-metal after etching the GaN-epilayer all the way down to the n-GaN. All six fields are designed on a 4” glass plate.

Furthermore, each field on the mask is designated by an alphanumerical name as follows:

F1: is a dark field (DF) mask used to create the p-contact metal rings by lift-off

F2: is a dark field (DF) mask used to create an opening in the oxide window for the hydrogenation process.

F3: is a dark field (DF) mask used to create the p-pad metal contact by lift-off.

F4: is a light field (LF) mask used to create the mesa for the optical cavity by dry-etching process.

F5: is a light field (LF) mask used to create an oxide layer to form a current blocking region. This filed is used only as an alternative method for the non-hydrogenation process.

F6: is a light field (LF) mask used to give us the option to form a top n-metal contact.

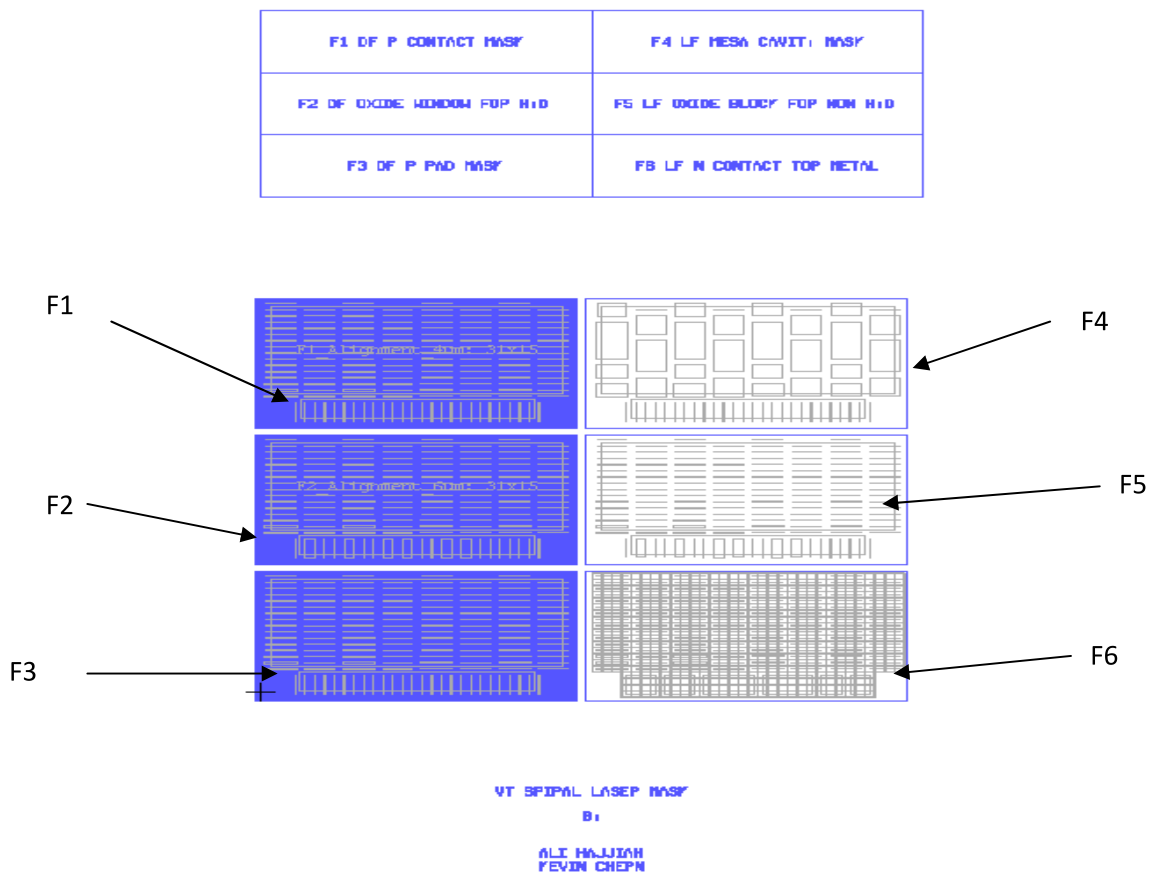

Figrue E.3: An image of the VT spiral laser mask

In each field there are 31 full and partial microdisk devices. Each full and partial microdisk device is repeated 4x for a total of 124 devices.

Also, in each field there are 4 spiral laser devices with radius =9µm, 6 spiral laser devices with radius =11µm, and 3 spiral laser devices with radius =18µm. Each of these 13 device types is repeated 4x with two different deformation parameters (ε=0.15, and ε=0.05) on the mask to give 104 devices with outcoupling angle of 90 degree.

In each of these devices, parameters such as the diameter of the etched cavity, the width of the p-contact metal ring, the separation between the p-contact metal and the edge of the cavity, the diameter of the oxide mask window for Hydrogenation , and the diameter of the p-pad metal window is varied. Table E.1 shows the variations in the different parameters for the full and partial microdisk devices, whereas; table E.2 shows the variations of these parameters for the spiral laser devices.

The following equations show how each parameter is contracted.

$$\frac{d_{pp}}{2} = \frac{d_{cacvity}}{2} - \left(\delta_{ME} + \frac{1}{4}\delta_{SW}\right) \qquad \text{(E.1)}$$

$$\frac{d_{ox}}{2} = \frac{d_{cavity}}{2} - \left(\delta_{ME} + \delta_{SW} + \delta_{ox}\right) \qquad \text{(E.2)}$$

$$\delta_{SW} = \frac{d_{SW}^{out}}{2} - \frac{d_{SW}^{in}}{2} \qquad \text{(E.3)}$$

We have decided to set the separation between the p-contact metal ring and the oxide mask window, δ_{ox}, to 1µm. Also, the width of the p-contact metal ring is formed by subtracting the inner radius of the p-contact metal ring from the outer radius of the p-contact metal ring. Eq(s).E. 4 and E.5 show how the inner and out radiuses are constructed.

$$\frac{d_{SW}^{out}}{2} = \frac{d_{cavity}}{2} - \delta_{ME} \qquad \text{(E.4)}$$

$$\frac{d_{SW}^{in}}{2} = \frac{d_{cavity}}{2} - \left(\delta_{ME} + \delta_{SW}\right) \qquad \text{(E.5)}$$

$\frac{d_{cacvity}}{2}$ (µm)	δ_{SW} (µm)	δ_{ME} (µm)	$\frac{d_{ox}}{2}$ (µm)	$\frac{d_{pp}}{2}$ (µm)
8	3	2	2	5.25
9	3	1	4	7.25
9	3	2	3	6.25
9	4	1	3	7
9	4	2	2	6
11	3	1	6	9.25
11	3	2	5	8.25
11	4	1	5	9
11	4	2	4	8
11	5	1	4	8.75
11	5	2	3	7.75
14	3	1	9	12.25
14	3	2	8	11.25
14	4	1	8	12
14	4	2	7	11
14	5	1	7	11.75
14	5	2	6	10.75
14	7	2	4	10.25
18	3	1	13	16.25
18	3	2	12	15.25
18	4	1	12	16
18	4	2	11	15
18	5	1	11	15.75
18	5	2	10	14.75
18	7	2	8	14.25
36	3	2	30	33.25
36	5	2	28	32.75
36	7	2	26	32.25
72	3	2	66	69.25
72	5	2	64	68.75
72	7	2	62	68.25

Table E.1: The important parameters in the mask design for the full circles and the partial circles.

$\frac{d_{cacvity}}{2}$ (μm)	δ_{SW} (μm)	δ_{ME} (μm)	$\frac{d_{ox}}{2}$ (μm)	$\frac{d_{pp}}{2}$ (μm)
9	3	1	4	7.25
9	3	2	3	6.25
9	4	1	3	7
9	4	2	2	6
11	3	1	6	9.25
11	3	2	5	8.25
11	4	1	5	9
11	4	2	4	8
11	5	1	4	8.75
11	5	2	3	7.75
18	3	1	13	16.25
18	3	2	12	15.25
18	4	2	11	15

Table E.2: The important parameters in the mask design for the spiral laser structure.